UPPSALA
UNIVERSITET

Digital Comprehensive Summaries of Uppsala Dissertations from the Faculty of Science and Technology 28

On Generation and Recombination in $Cu(In,Ga)Se_2$ Thin-Film Solar Cells

JONAS MALMSTRÖM

ACTA
UNIVERSITATIS
UPSALIENSIS
UPPSALA
2005

ISSN 1651-6214
ISBN 91-554-6191-3
urn:nbn:se:uu:diva-5721

Dissertation at Uppsala University to be publicly examined in Polhem hall, Ångström Laboratory, Friday, April 15, 2005 at 13:15 for the Degree of Doctor of Philosophy. The examination will be conducted in English

Abstract

Malmström, J. 2005. On Generation and Recombination in Cu(In,Ga)Se_2 Thin-Film Solar Cells. Acta Universitatis Upsaliensis. *Digital Comprehensive Summaries of Uppsala Dissertations from the Faculty of Science and Technology* 28. x, 112 pp. Uppsala. ISBN 91-554-6191-3

The solar cell technology based on Cu(In,Ga)Se_2 (CIGS) thin-films provides a promising route to cost competitive solar electricity. The standard device structure is ZnO:Al/ZnO/CdS/CIGS/Mo films on a glass substrate, where the first three layers are *n*-type semiconductors with wide bandgaps, forming a *pn*-junction with the *p*-type CIGS absorber layer; the Mo layer serves as a back contact. This thesis deals with analysis of the generation and recombination of electron-hole pairs throughout the device. These processes determine the maximum output power: generation limits the current; recombination limits the voltage.

The *generation* is calculated with an optical model based on complex refractive indices determined for the individual layers. The main features of the optical response of the solar cell can be reproduced with a specular model neglecting scattering. A model including ideally Lambertian scattering at the front and back surface of the CIGS absorber layer is introduced to investigate the possibility to maintain a high current generation with thin absorber layers. The result highlights the relatively poor optical performance of the Mo back contact. TiN and ZrN are explored as alternatives, and improved optical performance is experimentally demonstrated for both materials.

The *recombination* analysis emphasizes that, in general, more than one recombination path of comparable magnitude are operative in parallel. For cells with absorber bandgap increasing from 1.0 eV ($CuInSe_2$) to 1.7 eV ($CuGaSe_2$), a relative increase of interface recombination is found. When these cells are subject to accelerated ageing, degradation is smallest for intermediate bandgaps; an explanation involving different sensitivity to decreased absorber band bending and activation of grain boundaries is suggested. The optical gain with ZrN back contacts is counteracted by increased back contact recombination and contact resistance, but an intermediate layer of $MoSe_2$ is shown to alleviate these problems, allowing for an overall improved efficiency.

Keywords: solar energy conversion, solar cells, Cu(In,Ga)Se_2, device modelling, optical properties, electron-hole generation, light trapping, electron-hole recombination

Jonas Malmström, Department of Engineering Sciences, Solid State Electronics, Box 534, Uppsala University, SE-75121 Uppsala, Sweden.

© Jonas Malmström 2005

ISSN 1651-6214
ISBN 91-554-6191-3
urn:nbn:se:uu:diva-5721 (http://urn.kb.se/resolve?urn=urn:nbn:se:uu:diva-5721)

”När jag blir nyfiken står tiden still
då blir jag pigg och orkar lite till”

Bob Hund, *Düsseldorf*,
Omslag: Martin Kann (1996).

Till mina föräldrar

List of Papers

This thesis is based on the following appended papers, which are referred to in the text by their Roman numerals.

I	J. Malmström, J. Kessler, M. Edoff, and L. Stolt, "Relation between composition and optical properties of CdS films grown by chemical bath deposition", in: *Proceedings 19th European Photovoltaic Solar Energy Conference* (WIP-Munich, Munich, 2004), **II** p. 1909-12.
II	J. Sterner, J. Malmström, and L. Stolt, "Study on ALD In_2S_3/ $Cu(In,Ga)Se_2$ interface formation", *Progress in Photovoltaics: Research and Applications* (in press), DOI: 10.1002/pip.595 (2005).
III	O. Lundberg, M. Bodegård, J. Malmström, and L. Stolt, "Influence of the $Cu(In,Ga)Se_2$ thickness and Ga grading on solar cell performance", *Progress in Photovoltaics: Research and Applications* **11** (2003) p. 77-88.
IV	J. Malmström, O. Lundberg, and L. Stolt, "Potential for light trapping in $Cu(In,Ga)Se_2$ solar cells", in: *Proceedings 3rd World Conference on Photovoltaic Energy Conversion* (WCPEC-3 Organizing Committee, Osaka, 2003), **1** p. 344-7.
V	J. Malmström, S. Schleußner, and L. Stolt, "Enhanced back reflectance and quantum efficiency in $Cu(In,Ga)Se_2$ thin film solar cells with a ZrN back reflector", *Applied Physics Letters* **85** (2004) p. 2634-6.
VI	J. Malmström, J. Wennerberg, M. Bodegård, and L. Stolt, "Influence of Ga on the current transport in $Cu(In,Ga)Se_2$ thin film solar cells", in: *Proceedings 17th European Photovoltaic Solar Energy Conference* (WIP-Renewable Energies, Munich, 2001) **II** p. 1265-8.
VII	J. Malmström, J. Wennerberg, and L. Stolt, "A study of the influence of the Ga content on the long-term stability of $Cu(In,Ga)Se_2$ thin film solar cells", *Thin Solid Films* **431-432** (2003) p. 436-42.

VIII U. Malm, J. Malmström, C. Platzer-Björkman, and L. Stolt "Determination of dominant recombination paths in $Cu(In,Ga)Se_2$ thin-film solar cells with ALD-ZnO buffer layers", *Thin Solid Films* (in press), DOI: 10.1016/j.tsf.2004.11.008 (2005).

IX J. Westlinder, J. Malmström, G. Sjöblom, and J. Olsson, "Low-resistivity ZrN_x metal gate in MOS devices", submitted to Solid State Electronics (2005).

Reprints were made with permission from the publishers.

Comments on my contribution to the appended papers

I All experimental work (with help on RBS), the data analysis, and all of the writing with input from the co-authors.

II Optical characterisation and analysis, part of the device analysis and part of the writing.

III Contributions to the method used for optical analysis, and input to the device analysis and writing.

IV All of the optical analysis, part of the experimental work, and all of the writing with input from the co-authors.

V Definition of the project, part of the experimental work, and all of the writing with input from the co-authors.

VI Most of the electrical characterisation and the device analysis, and all of the writing with input from the co-authors.

VII Most of the electrical characterisation and the device analysis, and all of the writing with input from the co-authors.

VIII Contributions to the definition of the project and to the formulation of the new version of modified Arrhenius plot, and input to the data analysis and the writing.

IX Sputtering of the ZrN films, and input to the data analysis and the writing.

Work not included in this thesis

i. M. Bodegård, O. Lundberg, J. Malmström, L. Stolt, and A. Rockett, "High voltage Cu(In,Ga)Se_2 devices with Ga-profiling fabricated using co-evaporation", in: *Conference Record 28th IEEE Photovoltaic Specialists Conference* (IEEE, Piscataway (NJ), 2000), p. 450-3.

ii. J. Reiß, J. Malmström, A. Werner, I. Hengel, R. Klenk, and M. C. Lux-Steiner, "Current transport in $CuInS_2$ solar cells depending on absorber preparation", in: *Materials Research Society Symposium Proceedings* (Mater. Res. Soc, Warrendale (PA), 2001), **668** p. H9.4.1-6.

iii. T. Dullweber, O. Lundberg, J. Malmström, M. Bodegård, L. Stolt, U. Rau, H.-W. Schock, and J. H. Werner, "Back surface band gap gradings in Cu(In,Ga)Se_2 solar cells", *Thin Solid Films* **387** (2001) p. 11-13.

Contents

1 Introduction . . . 1
 1.1 Solar cells . . . 1
  1.1.1 $Cu(In,Ga)Se_2$ thin-film solar cells . . . 2
 1.2 What issues have been addressed and why? . . . 3
 1.3 About this thesis . . . 4
2 Generation . . . 5
 2.1 The goal: finding the generation profile . . . 5
  2.1.1 Some useful relations and definitions . . . 6
 2.2 Optical characterization and analysis . . . 10
  2.2.1 Calculating the optical response . . . 10
  2.2.2 Characterization: measuring the optical response . . . 11
  2.2.3 Analysis: deducing the optical properties . . . 11
 2.3 Optical properties of individual layers . . . 12
  2.3.1 DC-sputtered Mo back contact layer . . . 12
  2.3.2 Reactively sputtered ZrN back contact layer . . . 13
  2.3.3 Co-evaporated $Cu(In,Ga)Se_2$ absorber layer . . . 15
  2.3.4 CBD-CdS buffer layer . . . 20
  2.3.5 ALD-In_2S_3 buffer layer . . . 26
  2.3.6 RF-sputtered ZnO buffer layer . . . 34
  2.3.7 RF-sputtered ZnO:Al front contact layer . . . 36
 2.4 Modelling of generation in $Cu(In,Ga)Se_2$ devices – influence of CIGS thickness and back contact . . . 38
  2.4.1 Estimation of absorber absorptance as a function of absorber thickness using measured *R* and *T* spectra. . . . 39
  2.4.2 How much is there to gain with light trapping? . . . 43
  2.4.3 Experimental confirmation of optical gain with TiN and ZrN back reflectors . . . 47
3 Recombination . . . 49
 3.1 Basics of recombination in CIGS solar cells . . . 49
  3.1.1 Recombination mechanisms . . . 50
  3.1.2 Dominant recombination paths . . . 51
  3.1.3 Material aspects . . . 52
  3.1.4 Diode models for recombination in dark conditions . . . 54
 3.2 Modelling of the photocurrent loss . . . 59

3.2.1 The reciprocity theorem for carrier collection 59
3.2.2 A generalization of the reciprocity theorem to include both electrons and holes in the space charge region 60
3.2.3 Applications of the reciprocity theorem to collection in CIGS solar cells 62
3.2.4 Combining diode currents and the photocurrent under illumination 66
3.3 Recombination analysis of the diode currents 68
3.3.1 Fitting of one-diode model parameters 68
3.3.2 Discussion of the standard method for $J(V)_{\mathrm{T}}$ analysis . . . 69
3.4 Influence of the Ga content 72
3.5 Effect of damp-heat treatment depending on Ga content 73
3.6 Influence of the buffer layer 78
3.7 Influence of the absorber thickness and of Ga grading 79
3.8 Electronic losses with ZrN back contact and the beneficial effect of $MoSe_2$ 84
3.8.1 Suggested band diagrams at the back contact and effect on device performance 85
3.8.2 On the contact barrier of the CIGS/ZrN junction 87
3.8.3 $MoSe_2$ as a contact layer 89
4 Conclusions 91
5 Summary in Swedish 93
6 Acknowledgements 99

1. Introduction

During the course of the last century, there has been a quite spectacular development towards globally improved health, prolonged life time expectancy and increased material welfare, see Ref. [1] and references therein. One component in this development has been the increasing supply of energy to the society; the correlation between the energy supply and the standard of living as measured by the Human Development Index is very strong [2]. We can wish that progress continues, and accelerates in those regions where it has been slow. At the same time the environmental restrictions imposed on our energy usage have become more critical. In particular, it seems motivated by the risks associated with global warming to limit CO_2-emissions from the burning of fossil fuels [3].

Renewable energy sources have, more or less by definition, the advantages of (i) not being dependent on a resource that can be used up within relevant human time scales, and (ii) not resulting in accumulation of emissions or pollutants that risk disturbing the ecological system. The main disadvantage of renewable energy technologies of today, is that they cannot supply sufficient amount of energy at an acceptable cost. This is in particular true for solar cells, which is the technology dealt with in this thesis.

1.1 Solar cells

Solar cells can directly produce electricity from the energy in the the solar radiation.[1] The solar cell technology, or photovoltaics (PV), has some very attractive features:

+ The solar resource, the total amount of solar energy available, is huge.
+ Electricity is obtained, which is a practical, high-quality form of energy.
+ No pollutants are emitted during operation.
+ Solar cells are quiet. There are no moving mechanical parts in a solar cell.
+ Solar cells are durable; 20 years warranty is standard today.
+ The technology is modular and scalable.

But the solar electricity is also facing some important challenges:

- Relatively large areas are needed. This is because the solar energy is not

[1] A nice introduction to the operating principles and physics of solar cells is found in Ref. [4].

highly concentrated. However, only ~10 m^2 per capita would be needed to satisfy the total world supply of electricity.

- Electricity is produced only when the sun is shining. This implies a need for storage or combination with other electricity sources to meet electricity demand all around the clock.
- The cost of solar electricity is high, in the order of 0.5-1 €/kWh depending on installation site, interest rate etc.

Among these challenges, the cost issue is the most crucial one. The high cost explains why total installed capacity is relatively modest compared with, for example, wind energy and biomass. At the end of year 2003, the cumulative installations of PV modules were at about 1.800 MWp (where 1 Wp signifies output power of 1 W at standard solar intensity, 1000 W/m^2) in the OECD countries [5], representing an overwhelming majority of the global PV systems. The corresponding electricity generation is about 2–2.5 TWh per year, which is only somewhat more than a fraction 10^{-4} of the global electricity generation. On the other hand, the huge potential for solar electricity has motivated governmental initiatives to support the market development, in particular in Japan and Germany. This has resulted in a price decrease of about 30% for PV modules over the last four years. The price development has followed the economy of scale in such way that each time the cumulative production has doubled, the price has been reduced by 20%.

The latter observation is valid for the conventional solar module technology based on crystalline silicon wafers. Solar cell technologies based on thin-films, such as $Cu(In,Ga)Se_2$ solar cells, are considered to have a larger potential for cost reductions, because of reduced material and energy consumption in the production. However, this potential has not yet been realized in commercial production. The lack commercial success of thin-film technologies up to now can be explained by lower efficiency compared to crystalline silicon modules, and not yet proven durability; crystalline silicon module have proven to be extremely reliable. Therefore, the key requirements for a thin-film solar cell technology to become commercially viable is (i) low production cost, (ii) an efficiency comparable with today's crystalline silicon modules, (iii) high durability, and, in addition, (iv) low environmental impact of the production process.

1.1.1 $Cu(In,Ga)Se_2$ thin-film solar cells

The research in our group is concerned with thin-film solar cells based on $Cu(In,Ga)Se_2$ (CIGS) [6, 7]. As illustrated in Fig. 1.1, the standard device structure is ZnO:Al/ZnO/CdS/CIGS/Mo/glass substrate, where the total thickness of the five active layers is only about 3 μm = 0.003 mm. This is possible since the CIGS layer is so highly absorbing that almost all of the in-coming

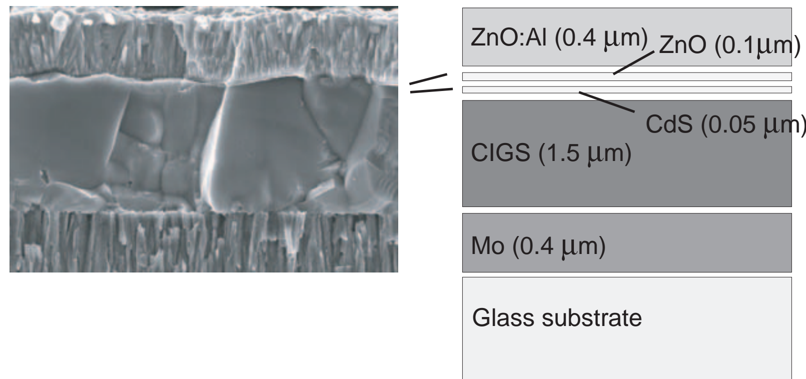

Figure 1.1: Scanning Electron Micrograph (left) and schematic illustration of the standard structure of $Cu(In,Ga)Se_2$ thin-film solar cells. Courtesy: M. Edoff.

photons with energy above its optical bandgap are absorbed within 1.5 μm.

The fabrication of a solar cell according to our baseline process [8] can be briefly described as follows:

1. The substrate glass is cleaned with detergent and rinsed in ultra-sonic bath.
2. The Mo back contact is deposited by DC sputtering.
3. The $Cu(In,Ga)Se_2$ absorber layer is deposited by co-evaporation from sources containing elemental Cu, In, Ga and Se.
4. The CdS buffer layer is deposited by chemical bath deposition (CBD).
5. The additional buffer layer of non-intentionally doped ZnO and the transparent front contact of Al-doped ZnO (ZnO:Al) are deposited by RF sputtering.
6. A Ni/Al/Ni metal grid is evaporated through a shadow mask onto the front side to decrease resistive losses.
7. Solar cells are isolated from each other by mechanical scribing.

1.2 What issues have been addressed and why?

Three topics closely related to the overall objectives of low cost, stability and low environmental impact are in focus for the CIGS research in our group:

- "Fast'n'Thin" CIGS deposition: By decreasing the deposition time and by making the CIGS layer even thinner than 1.5 μm with efficiency maintained high, cost reductions can be realized, c.f. thesis by O. Lundberg [9].
- Replacement of the CdS buffer: Buffers not containing toxic Cd are investigated, c.f. thesis by J. Sterner [10].
- Stability issues: Durability is tested using accelerated ageing such as damp-heat treatment, and degradation mechanisms are analysed, c.f. thesis by J. Wennerberg [11].

Rather than specifically addressing one of these topics, my project has been oriented towards characterisation and modelling of the properties of the solar cell device. In general, when successfully carried out, modelling of a physical system can help explain experimental observations, increase understanding of the system, and serve as a guide to new experiments and modified design of the system.

"A quantitative model with predictive power for $Cu(In,Ga)Se_2$ solar cells" was the rather brave goal defined when I started as PhD student in Uppsala in January 2000. The idea was to pin down the material properties of standard $Cu(In,Ga)Se_2$ solar cells that could be plugged into a device simulator computer software in order to reproduce measured device characteristics. Five years later, it is clear that I have not reached that goal – the world of $Cu(In,Ga)Se_2$ solar cell materials and physics was richer and more complex than I had realized.

Of course, failure to reach the original goal does not necessarily mean that the time has been spent without achievements. The results obtained from device analysis represent small steps on the way to the overall goal of a quantitatively reliable model of CIGS solar cells. The optical analysis undertaken also guided us to suggest a modified design of the CIGS cell with optically improved back contact. This development might allow for a reduced thickness of the CIGS layer at maintained efficiency, and thus more directly addresses the key questions of reducing cost and material consumption.

1.3 About this thesis

Analysis of solar cells naturally divides into optics – where are the photons absorbed and the electron-hole pairs generated? – and electronics – how do the electrons and holes move and where do they recombine? Chapter 2, Generation, and chapter 3, Recombination, correspond to these two categories. In these chapters, I have had the ambition to deepen the discussion on the results found in the appended papers, and, in some cases, to add new results. I have also allowed myself to be rather speculative, in particular in chapter 3. This all comes with the risk of loosing focus, which, however, hopefully will be found regained at the end, in chapter 4, where conclusions are listed. Finally, a summary in Swedish is given in chapter 5.

2. Generation

2.1 The goal: finding the generation profile

The first step in the conversion of energy in the solar radiation into electricity in a *pn*-junction solar cell is the generation of an electron-hole pair: the energy of a photon is absorbed by an electron that is excited from the valence band to the conduction band, and leaves behind a positively charged "hole". Each optically generated electron-hole pair can potentially contribute with one electron to the output current. It is therefore of interest to know *how many* electron-hole pairs that are generated by a certain radiation incident on the solar cell. Since the probability for an electron-hole pair to contribute to the output current depends on the position, x, where it was generated, it is also of interest to know *where* the optical generation takes place. The questions "how many" and "where" are answered by the *generation profile*, which I will denote $G(x)$. The objective of optical modelling for solar cells, at least from a device modelling point of view, is to be able to calculate such generation profiles. Fig. 2.1 shows an example of a generation profile, calculated with the optical model for CIGS solar cells presented in this chapter.

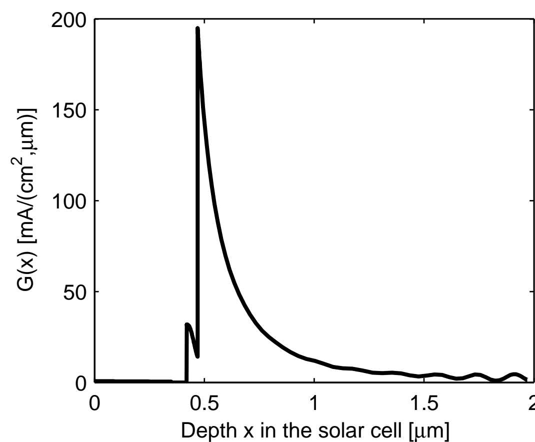

Figure 2.1: Generation profile calculated with the optical model presented in this chapter, with the incident flux of photons given by the standard AM 1.5 spectrum. The thickness of the layers in the ZnO:Al/ZnO/CdS/CIGS structure was 350 nm, 70 nm, 50 nm and 1.5 μm, respectively.

It can be seen that the generation profile has a strong peak at $x \approx 0.5$ μm. This is where the light enters the CIGS absorber, which has a very strong absorption coefficient. Once $G(x)$ is obtained, it can be used as input to a device simulator program, that solves the differential equations describing the transport of electrons and holes in the solar cell and calculates the output power. SCAPS-1D (or SCAPS), a device simulator developed for polycrystalline thin-film solar cells by the group of Prof. Burgelman [12, 13], offers from version 2.4 the possibility to import an externally calculated generation profile $G(x)$. This is one reason why I have used that software for the simulations referred to later in this thesis.

2.1.1 Some useful relations and definitions

Let $\Phi(x)$ be the total photon flux at some point x in the solar cell. The decrease in $\Phi(x)$ can be identified with absorption rate, which is the sum of the generation and other, in this context parasitic, absorption processes:

$$-\frac{d\Phi}{dx} = absorption = A_{tot}(x) = G(x) + A_{par}(x) \tag{2.1}$$

The easiest way to calculate the total photon flux and the total generation rate is to make the calculation for one photon wavelength λ at a time, and then use the superposition principle to add contributions from the different wavelengths present in the solar spectrum. At a specific wavelength λ, we have

$$\begin{aligned} -\frac{d\Phi(x,\lambda)}{dx} &= A_{tot}(x,\lambda) = G(x,\lambda) + A_{par}(x,\lambda) \\ -\Phi_0(\lambda)\frac{d\phi(x,\lambda)}{dx} &= a_{tot}(x,\lambda) = g(x,\lambda) + a_{par}(x,\lambda), \end{aligned} \tag{2.2}$$

where, in the second equation, the photon flux $\Phi_0(\lambda)$ incident on the solar cell has been used to define normalized versions of the of the photon flux ($\phi(x,\lambda)$), the total absorption ($a_{tot}(x,\lambda)$), generation rate ($g(x,\lambda)$) and the parasitic absorption ($a_{par}(x,\lambda)$). If the normalized generation rate $g(x,\lambda)$ is known and the superposition principle holds – which it does very well for optical absorption at normal solar intensity – then the generation profile $G(x)$ can be calculated for an arbitrary spectrum $\Phi_0(\lambda)$ incident on the solar cell:

$$G(x) = \int_0^\infty \Phi_0(\lambda) g(x,\lambda) d\lambda \tag{2.3}$$

In fact, to get $G(x)$, we need an optical model that provides $g(x,\lambda)$.

Reflectance, transmittance and absorptance

Fig. 2.2 illustrates the optical model that has been used in this work. A basic assumption is that the layers in the solar cell structure can be considered uniform and separated by abrupt, flat interfaces with regards to the propagation of light in the layers. The validity of this assumption requires that the length scale of non-uniformities at the interfaces, i.e. the surface roughness, is much smaller than the wavelength of the light. That condition is in most cases not fulfilled, but this *specular model*, i.e. an model not including light scattering, provides a reasonable starting point for the calculation of the generation profile.

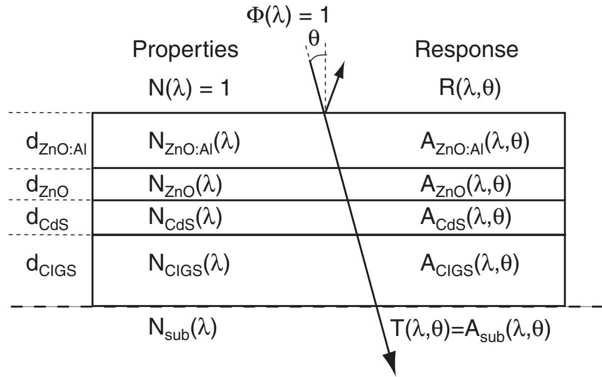

Figure 2.2: Specular (non-scattering) optical model of the CIGS solar cell and illustration of optical response. With this simplified model, the optical response (reflectance R, layer absorptance A_i and transmittance T) to incident light of given wavelength, angle of incidence and polarization can be readily calculated from the complex refractive index N_i and the thickness d_i of each layer.

As indicated in the figure, a photon with wavelength λ incident at an angle of incidence θ can either be reflected from the structure, or absorbed in one of the layers, or transmitted to the substrate. Note that in the standard structure, the (optical) substrate is the Mo back contact, since no light is transmitted through the Mo layer to the substrate glass. The fraction $R(\lambda,\theta)$ of the incident photons (with given wavelength, angle of incidence and polarization) that are reflected is called the reflectance, the fraction $A_i(\lambda,\theta)$ of the incident photons absorbed in layer i is called the absorptance, and the fraction $T(\lambda,\theta)$ transmitted to the optical substrate is called the transmittance. From conservation of energy

$$\begin{aligned} 1 &= R + A + T, \text{ where} \\ A &= \sum_i A_i \end{aligned} \tag{2.4}$$

Optical properties

The propagation of light, i.e. electro-magnetic waves, in the layered structure is controlled by the thickness d, and the complex refractive index $N = n - ik$ of each layer (and the substrate and medium of incidence); these are input parameters to the calculation.

The real part n of the refractive index determines the phase velocity of the light in the medium, and the imaginary part, the extinction coefficient k, determines the damping of the field amplitude. The optical properties can alternatively be expressed by the dielectric function, which equals the square of the complex refractive index

$$\varepsilon(E) = N^2(E) = \varepsilon_1(E) + i\varepsilon_2(E), \tag{2.5}$$

here expressed as a function of the photon energy $E = hc/\lambda = 1240\ \text{eVnm}/\lambda$. The dielectric function is more directly coupled to the electronic structure of the material than the refractive index, while the latter is more convenient for the description of the propagating light. A relation useful for the discussion is the normal incidence reflectance at an interface between two materials with refractive index N_2 and N_1:

$$R_{\perp} = \frac{|N_2 - N_1|^2}{|N_2 + N_1|^2} = \frac{(n_2 - n_1)^2 + (k_2 - k_1)^2}{(n_2 + n_1)^2 + (k_2 + k_1)^2}. \tag{2.6}$$

This relation shows that high reflectance is obtained if there is a big difference, a high contrast, in refractive index between the two materials.

Generation current, collection function and photocurrent

By integrating the generation in the solar cell, the total generation current is obtained

$$J_{gen} = q \int_{cell} G(x)dx = q \int_0^{\infty} \Phi_0(\lambda) \int_{cell} g(x,\lambda)d\lambda dx \tag{2.7}$$

The second integral is equal to total absorptance due to generation of electron-hole pair, $A_{gen}(\lambda)$, which means that the total generation current also can be written

$$J_{gen} = q \int_0^{\infty} \Phi_0(\lambda) A_{gen}(\lambda) d\lambda \tag{2.8}$$

The same equation can be used to calculate the current generated in one of the layers, from the absorptance of this particular layer, for example the CIGS absorber layer. Note that for both CIGS, CdS and ZnO, the parasitic absorption is low, so the total absorptance and the absorptance from generation of

electron-hole pairs are practically equal. For ZnO:Al, parasitic absorption it is important, because of free-carrier absorption not creating electron-hole pairs (c.f. section 2.3.6).

Unfortunately, not all of the generated electron-hole pairs contribute to the photocurrent J_L. The actual photocurrent can be obtained by integrating the generation profile multiplied by a collection function (or collection probability), $f_c(x)$, which may depend also on the applied voltage V and on the illumination Φ:

$$J_L(V,\Phi) = q\int_{cell} f_c(x,V,\Phi)G(x)dx \tag{2.9}$$

It is therefore desired that the collection probability is high in those regions of the solar cells where there generation rate is high. One advantage with CIGS solar cell structure is that the collection probability can be close unity, the maximum possible value, in the upper region of the CIGS layer, close to the CdS layer, where the generation is at maximum (see Fig. 2.1).

Quantum efficiency

If we measure the photocurrent J_L obtained when the solar cell is illuminated by monochromatic light of wavelength λ, and divide the number of electrons in the measured photocurrent by the number of photons in the incident light, then we have measured the *quantum efficiency*, QE. That is, the QE is defined as the probability that a photon incident on the solar cell contributes to the external photocurrent, as a function of the photon wavelength. It can be regarded as the product of $A_{gen}(\lambda)$, the wavelength-dependent probability for absorbing a photon and generating an electron-hole pair, and a probability $\tilde{f}_c(\lambda)$ that this generated electron-hole pair to contributes to the photocurrent:

$$QE(\lambda) = A_{gen}(\lambda)\tilde{f}_c(\lambda) \tag{2.10}$$

A QE measurement often provides valuable information on the properties of the solar cell. In Fig. 2.3, an estimate of $A_a(\lambda)$, the absorptance due to generation in the absorber layer, and a measurement of QE(λ) is shown for three CIGS cells with different thickness d_a of the absorber. It can be seen from the figure that as d_a is decreased, $A_a(\lambda)$ (the solid lines) decrease (because less light is absorbed in a thinner absorber). It can also be seen that the QE decreases more than A_a with decreasing d_a, due to degradation of $\tilde{f}_c(\lambda)$. (The method used to estimate $A_a(\lambda)$ from measurements of transmittance and reflectance will be discussed in section 2.4.1, and the reasons for the degradation of the collection probability will be discussed in section 3.7.)

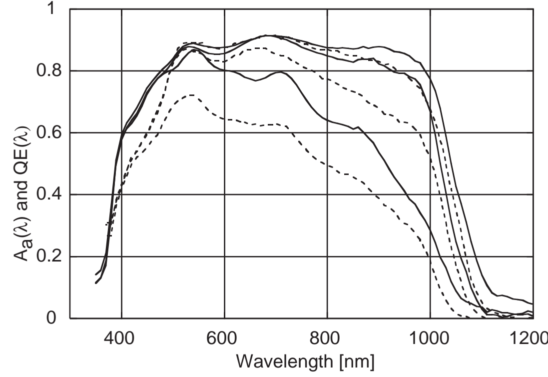

Figure 2.3: Example from Paper III of modelled absorber absorptance $A_a(\lambda)$ (solid lines) and measured QE(λ) (dashed lines) for three CIGS cells with different thickness d_a of the absorber; the highest curves are for $d_a = 1.8\ \mu$m, the intermediate curves are for $d_a = 0.8\ \mu$m and the lowest curves are for $d_a = 0.36\ \mu$m.

Finally, it can be noted that QE can be used to calculate the photocurrent,

$$J_L = q \int_0^\infty \Phi_0(\lambda)\mathrm{QE}(\lambda)d\lambda \tag{2.11}$$

and that it can be expressed in terms of the collection function f_c and the normalized generation $g(x,\lambda)$:

$$QE(\lambda) = \int_{cell} f_c(x)g(x,\lambda)dx \tag{2.12}$$

2.2 Optical characterization and analysis

Optical modelling involves three linked activities

1. Definition of a model that can be used to calculate the optical response of the structure given the input light and the material parameters.
2. Measurement of the optical response.
3. Analysis of the optical response to deduce the material parameters.

2.2.1 Calculating the optical response

The specular model chosen in this project was introduced in Fig. 2.2. For such a stack of uniform layers with abrupt interfaces the calculation of reflectance, transmittance and other measurable quantities is well established, see, e.g., Ref. [14], which I have used as a reference on thin-film optics.

In practice, the calculations have been performed with a package of Matlab scripts, called *moptics*, developed during the course of the project. The package can handle an arbitrary combination of coherent and non-coherent layers (such as glass substrates), and can be used to compute spectrophotometric quantities (R and T), ellipsometric quantities, generation profile $g(x,\lambda)$, e.t.c.

2.2.2 Characterization: measuring the optical response

The optical characterization has been done mainly by spectrophotometry, by which the reflectance and transmittance are measured in different ways. Two different systems were used: A commercial Perkin-Elmer λ900 double beam instrument, and a custom single-beam system.

Perkin-Elmer λ900

The Perkin-Elmer λ900 system is equipped with an integrating sphere, which allows for measurements of total as well as diffuse ("specular excluded") signals of response of scattering samples. When used for specular samples, a specular backside Al-mirror was used as reflectance reference, which was calibrated with the single-beam instrument.

Single-beam instrument

The custom-made single-beam instrument is described in Ref. [15]. With this instrument, both reflectance and transmittance can be measured with varying angle of incidence for different polarizations. It can be used with integrating spheres for scattering samples. In this work it was used mostly in specular mode. This mode is called "absolute", since no further corrections are needed once the measured spectra has been divided with the reference spectra (taken without any sample) that defines the 100% level.

2.2.3 Analysis: deducing the optical properties

Although the calculation of the optical response is straightforward for the specular optical, the inverse operation, to extract the optical properties given measurement data, is not trivial. I have employed two approaches – modified point-by-point fit and fitting of dispersion relations.

Numerical inversion, "point-by-point fit"

When a single layer is to be characterized, there are two unknown parameters (n and k) at each wavelength. It should be possible to determine these by two independent measurements, e.g. R and T at each wavelength point. An advantage with this method is that no assumptions have to be made about the wavelength-dependence of the optical properties.

However, a well-known problem is that there can exist multiple solutions of optical properties (n,k) for a given combination of measurement data (R, T). For critical combinations of R, T, film thickness and wavelength – at so-called branch points – the slightest measurement error will change the solution from a physically correct branch of solutions to an un-physical one. This problem often causes discontinuities in the n-values obtained. In order to reduce the influence of the branch-points, I have followed the procedure proposed by Djurisič *et al.*[16, 17].

Physical models – fitting of dispersion relations

The second approach is to reproduce measurement data by fitting the parameters of a physical model for the energy- (wavelength-) dependence of the optical properties of a material – a *dispersion relation* or an optical function; for a recent review of dispersion relations, see Ref. [18]. A disadvantage of this approach is that an appropriate model must be identified. In many cases dispersion relations are used only as parametrizations of the energy-dependence of the optical properties, without any coupling to the material properties. However, if a model is found that is actually linked to the electronic structure of the material, then the fit parameters can tell something of physical interest.

2.3 Optical properties of individual layers

In this section, the determination of the optical properties (n and k) of the individual layers in the solar cell structure is presented and discussed with reference to the literature.

2.3.1 DC-sputtered Mo back contact layer

In their short literature review of optical properties of Mo in the Handbook of optical constants (vol I) , Lynch and Hunter [19] state that “the optical properties of Mo have been measured many times and the results generally agree rather well” and cite 30 references. Tabulated in the IR-VIS-UV region (0.1 eV – 35 eV) is the data published by Weaver *et al.* [20], and this is the data used below as reference values for bulk material. Their high purity samples were carefully mechanically, chemically and electrically polished and cleaned before measured. For thin films prepared by evaporation, Nestell *et al.* [21] reported that the reflectance was lower than for bulk material when the substrates were at room temperature. With increased substrate temperature (1000°C) and annealing at 700°C, the reflectance approached bulk values, which was explained by improved crystallinity. As for thin film Mo deposited by sputtering, I have not found data in the literature.

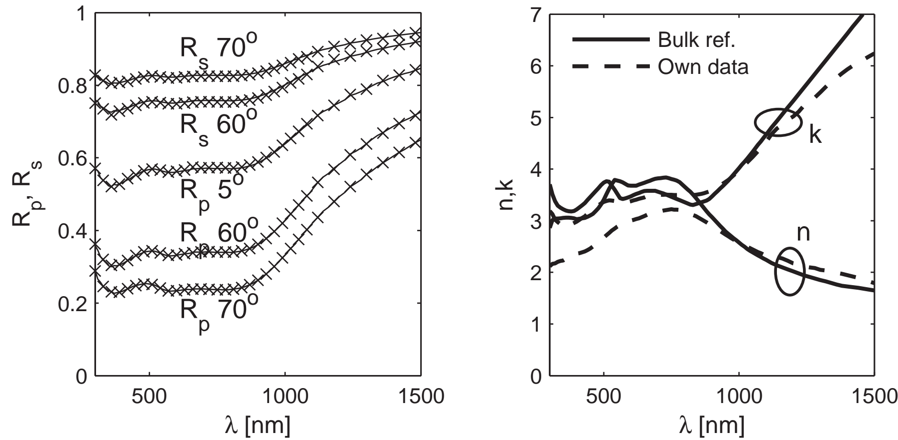

Figure 2.4: Left: Measured (x) and modelled (lines) reflectance R of sputtered Mo for different polarizations (s and p) and different angles of incidence $\theta_{in} = 5°, 60°$, and $70°$ as annotated in the graph. Right: $n(\lambda)$ and $k(\lambda)$ from point-by-point-fit, compared with bulk reference data from Ref. [20].

Fig. 2.4 illustrates a determination of n and k for a sputtered Mo film from a measurement of reflectance at varying angle of incidence and polarization. The measurements were made with the single-beam instrument, and the fit was made point-by-point with suppression of discontinuities as proposed in Refs. [16, 17]. It can be seen that n and k of the sputtered sample have less pronounced structures with respect to the bulk reference. The level of n and k is generally lower, which translates into a lower reflectance compared to bulk material.

It can be remarked that:

- When Mo samples were characterized by both reflectance at varying angle of incidence and ellipsometry, good agreement was found.
- The optical properties of sputtered Mo vary quite a lot depending on the process parameters. Films sputtered at higher process pressure and lower sputter power have lower reflectance. The data of Fig. 2.4, which I have used in the optical simulations, are for a film sputtered at relatively low pressure and high power.
- The reflectance decreases with storage time, most probably due to oxidation.

2.3.2 Reactively sputtered ZrN back contact layer

Optimization of the deposition process

In Paper V, ZrN was investigated as an optically improved alternative to the standard Mo back contact. The ZrN layers were deposited by reactive sput-

tering from a Zr target. The key parameter in reactive sputtering is the partial pressure of the reactive gas, which in general depends non-linearly on the controlled process parameters such as the flow of the reactive gas fed into the chamber [22]. In the current case, not only the flow of nitrogen gas, but also the base pressure and sputtering rate were found to be important parameters for the deposition of ZrN films of high optical quality. Good results were obtained with a base pressure below 10^{-7} mbar and at a deposition rate of about 3 nm/s.

When the base pressure was high and the sputter rate low, films with low conductivity and low reflectivity were obtained. Since Zr is very reactive with oxygen, this can probably be explained by inclusion of oxygen in the film, either as segregations of ZrO_2 or in the crystal structure. High nitrogen gas flow decreases the deposition rate and, therefore, increases the relative impact of oxygen residuals in the chamber. When the nitrogen gas flow was too low, under-stoichiometric Zr-like films were obtained. Examples of ZrN films from this optimization, showing different optical quality, can be found in the master thesis of Sebastian Schleussner, Ref. [23].

Optical properties obtained

The reflectance of a high-quality film, having a resistivity below 50 $\mu\Omega$cm, is shown in the left graph of Fig. 2.5. It has been shown by Veszelei *et al.* [24] that the structure-less reflectance for low photon energies (long wavelengths) of high-quality ZrN is determined by its free-electron character. The optical properties are therefore well described by a screened Drude model:

$$\varepsilon(E) = \varepsilon_\infty + \chi_{Drude}(E) = \varepsilon_\infty - \frac{E_N^2}{E^2 + i\Gamma E}. \tag{2.13}$$

where $E = \hbar\omega = hc/\lambda$ is the photon energy. E_N is called the un-screened plasma energy, which is proportional to the density n_e of free electrons. $\Gamma = \hbar/\tau$ is a damping coefficient for the free electrons with relaxation time τ, and ε_∞ is a real constant that accounts for the influence of interband transitions at higher photon energies.

This is of practical use, since the optical properties of a ZrN film can be obtained from a straightforward fit of the parameters in the screened Drude model to measured reflectance data. For the reflectance data shown in Fig. 2.5, $\varepsilon_\infty = 10.28$, $E_N = 9.88$ eV and $\Gamma = 0.76$ eV were obtained. The resulting model reflectance is given by the solid line in the left graph, and the real part n and imaginary part k of the refractive index are given in the right graph.

The (screened) plasma energy, E_P, is defined by $\varepsilon_1(E_P) = 0$, which allows for longitudinal oscillations of the electrons [25]. It follows from Eq. 2.13 that

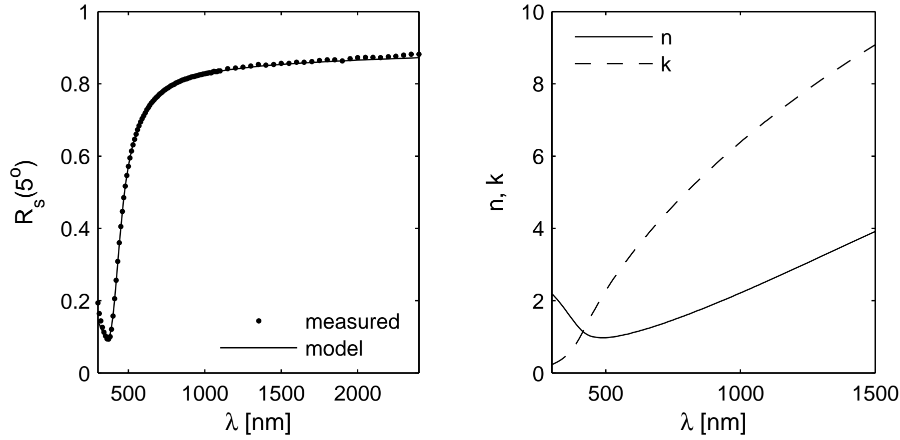

Figure 2.5: Left: Measured and modelled reflectance R_s for s-polarized light measured at $\theta_{in} = 5°$C. The model data were obtained from a fit of Eq. 2.13, yielding $\varepsilon_\infty = 10.28$, plasma energy $E_N = 9.88$ eV and relaxation energy $\Gamma = 0.76$ eV. Right: $n(\lambda)$ and $k(\lambda)$ resulting from the fit.

$$E_P^2 = \frac{E_N^2}{\varepsilon_\infty} + \Gamma^2 \approx \frac{E_N^2}{\varepsilon_\infty} \qquad (2.14)$$

With the parameters obtained in the fit of Fig. 2.5, $E_P = 3.2$ eV is obtained. The screened plasma energy (here at $\lambda_P = 390$ nm) controls the position of the reflectance minimum seen in Fig. 2.5. It can be noted from Eq. 2.14 that the parameter ε_∞ accounts for the screening, i.e. the difference between the unscreened plasma energy E_N and the screened plasma energy E_P.

2.3.3 Co-evaporated Cu(In,Ga)Se_2 absorber layer

At the beginning of my PhD project, there was only little data available on the optical properties of $CuInSe_2$ and $CuGaSe_2$, and hardly any on polycrystalline $CuIn_{1-x}Ga_xSe_2$ thin-films with varying Ga content x. (For a comprehensive and yet concise review of the literature available on determination of optical data n and k for CIGS, see the thesis by Kay Orgassa [26].) Since the Cu(In,Ga)Se_2 layer is the most important layer in CIGS solar cells in general and for the generation of electron-hole pairs in particular, the experimental determination of n and k for $CuIn_{1-x}Ga_xSe_2$ for different Ga content x therefore appeared to be an important task. However, the determination of optical properties is more difficult than for the other layers in the structure because of the following complications:

High surface roughness. Device-quality CIGS films have a relatively high surface roughness. The roughness depends on the specifics of the de-

position process. For our baseline process, the root-mean-square (rms) value of the surface roughness (σ_{rms}) is typically ~5% of the film thickness. The surface roughness distorts the spectrophotometric as well as the ellipsometric response of the film relative to the case of smooth surfaces, in a way that is not trivial to take into account. For example, effective medium theories for the roughness layer are not applicable when σ_{rms} is comparable with (> 10% of) the wavelength of the light.

Surface overlayers. An unprotected CIGS surface is known to react with the atmosphere. The surface overlayers formed, essentially indium oxides, have lower refractive index than the CIGS material, which affects the optical response. In particular, the reflectance is lowered since the surface overlayers act as index-matching anti-reflective coatings.

High absorption coefficient. The high absorption coefficient of $Cu(In,Ga)Se_2$ implies that a non-vanishing transmittance throughout the spectral region of interest is obtained only for very thin films. Thus, methods for determination the optical properties relying on the transmittance cannot be applied for films of standard thickness. This is a potential problem, since thinner films may have different optical properties (due to different crystal quality) than standard-thick films. Note that high absorption coefficient is not a problem for ellipsometry.

Before I had mastered these experimental challenges in a satisfactory way, new data were added in the literature:

- Alonso *et al.* determined by spectroscopic ellipsometry the optical properties of single crystalline $CuInSe_2$ ($x = 0$) and $CuGaSe_2$ ($x = 1$) [27] and bulk samples of polycrystalline $CuIn_{1-x}Ga_xSe_2$ with $x = 0.2$, 0.4, 0.6, and 0.75 [28]. The surface roughness and surface overlayers were addressed by careful mechanical and chemical polishing.
- Paulson *et al.* [29] solved the surface roughness issue of thick co-evaporated $CuIn_{1-x}Ga_xSe_2$ films in an elegant way: the films were peeled off from the Mo substrate, and the optical properties could then be measured by spectroscopic ellipsometry on the smooth back surface side. The influence of oxidation was reduced by characterizing the films immediately after peeling. Results were reported for $x = 0.00$, 0.31 0.45, 0.66 and 1.00.
- Orgassa *et al.* determined n and k from R- and T-measurements at normal incidence of co-evaporated $CuIn_{1-x}Ga_xSe_2$ thin films with Ga content $x =$ 0.00, 0.23 0.51, 0.73 and 1.00 [26, 30]. The inversion from RT to nk was done with a method where the bifurcation point discontinuities in the n-values obtained from a point-by-point are by-passed with a linear functions that join regions of well-determined n. By using thin samples (210 nm – 270 nm), smooth surfaces (σ_{rms} measured to a few nm by atomic force microscopy, AFM) and high enough transmittance was obtained.

The connection between the optical properties and the band structure of $Cu(In,Ga)Se_2$ is discussed by both Alonso and Paulson. Below, I will discuss how the optical data of Alonso, Paulson and Orgassa compare with each other and with own CIGS data that I have used for the simulations of Paper IV and in this thesis. The latter were determined from fitting to a spectrophotometric characterization of a $CuIn_{1-x}Ga_xSe_2$/glass sample, with absorber thickness $d_a \approx 160$ nm. The absorber had a Ga content x of (0.42 ± 0.05) and a [Cu]/([In]+[Ga]) ratio of (0.94 ± 0.05), according to X-ray fluorescence (XRF) data. Reflectance R and transmittance T for p-polarized light at three different angles of incidence, $\theta_{in} = 5° 60°$, and 70°, were measured with the single-beam instrument; results for 5° and 60° are shown with symbols in Fig. 2.6. The solid lines show simulation results for a fit of a Forouhi-Bloomer dispersion relation [31] with two oscillator terms. As can be seen from the graph, the quality of the fit is not excellent. This is most probably due to the effect of surface roughness and surface overlayers, which was not included in the optical model. The surface issues affect above all the n-values, while the k-values are well determined from the transmittance data. Good agreement was obtained between k-values from point-by-point fits and the dispersion fit. Since the dispersion fit yielded a more continuous variation of n, which agreed well in shape with the at the time recently published data by Alonso for $CuInSe_2$, the result of the dispersion was used in the simulations.

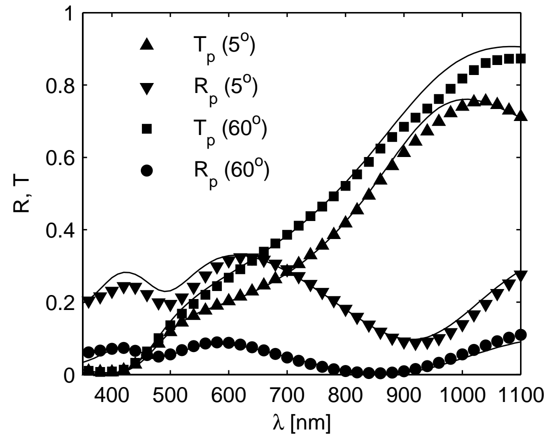

Figure 2.6: Measurement (symbols) and simulation (lines) of reflectance and transmittance of p-polarized light of a $CuIn_{0.6}Ga_{0.4}Se_2$/glass sample with (fitted) absorber thickness $d_a = 158$ nm. The simulated data were obtained from a fit of a Forohui-Bloomer dispersion [31] with two oscillators. No correction was made for the influence of surface overlayers and surface roughness.

In the comparison I will also include data from the master thesis of Johan Börjesson [32], who characterized $CuIn_{1-x}Ga_xSe_2$/Mo samples prepared in

our laboratory by spectroscopic ellipsometry in the range 0.8 eV – 6.5 eV. The samples had a thickness in the range 400 nm – 440 nm, and a Ga content of $x = 0.0$, 0.3 and 1.0, respectively. The surface roughness was measured by AFM to $\sigma_{rms} \approx 25$ nm.

Data comparison

Data for $CuInSe_2$ (x = 0) are shown in Fig. 2.7. Looking first at the n-values, the agreement between Alonso, Orgassa, and Paulson is very good. The n-values of Börjesson are similar in shape but significantly lower, which he explained by the influence of the relatively high surface roughness [32]. The increase in Orgassa's n-values for shorter wavelengths could possibly be explained by the fact that his reflectance data were not corrected for the reflectance R_{ref} of the reference material used in the integrating sphere. $R_{ref} < 1$ then leads to an overestimation of R and n, and R_{ref} (e.g. for $BaSO_4$) typically decreases for decreasing λ. The slight hump around $\lambda = 750$ nm is the effect of a bifurcation point, c.f error bars given in Ref. [30].

Turning to the k-values in the right graph, the first observation is that Alonso's data are higher then the others throughout the spectrum. This might reflect that her data are for bulk single crystals, while the other data are for polycrystalline thin-films. It can be noted that Alonso did not include results for $k < 0.1$, since they were judged inaccurate. The ellipsometry data of Paulson and Börjesson have in common that $k > 0$ is obtained also for subbandgap (long) wavelengths, in disagreement with k-values by Orgassa, obtained from RT-measurements, which decrease sharply to $k \approx 0$ at the bandedge.

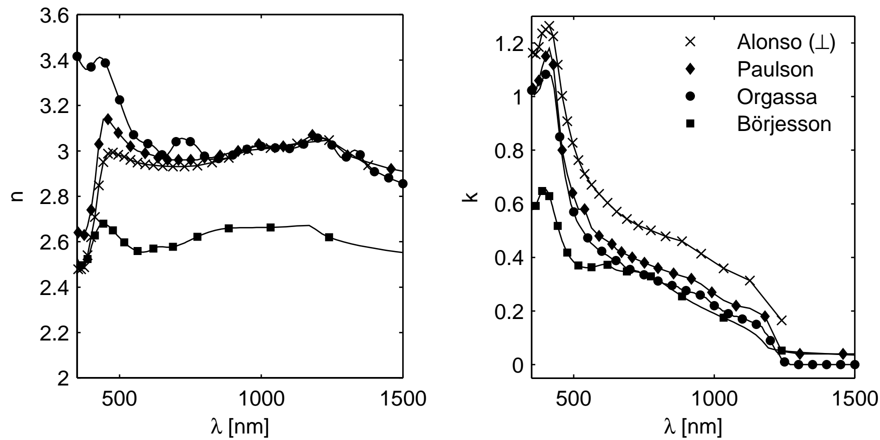

Figure 2.7: Real part n (left) and imaginary part k (right) of the refractive index of $CuInSe_2$ determined by Alonso [27] (ordinary component $\perp$), Paulson [29], Orgassa [26, 30], and Börjesson [32].

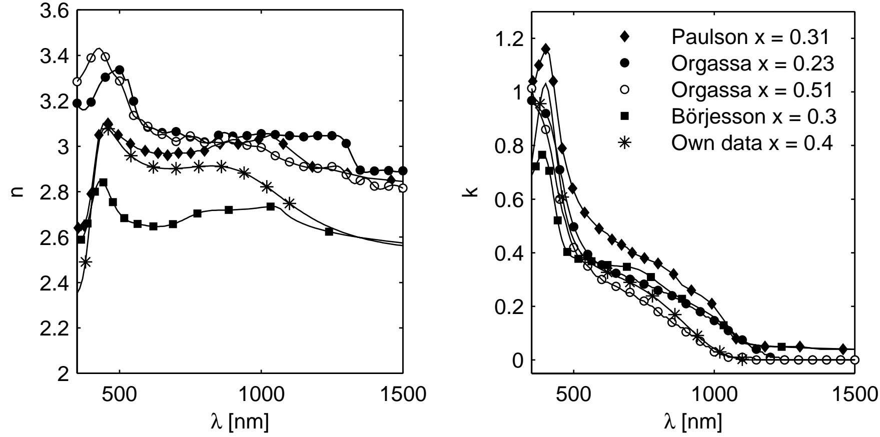

Figure 2.8: Real part n (left) and imaginary part k (right) of the refractive index of $CuIn_{1-x}Ga_xSe_2$ according to Paulson [29] ($x = 0.31$), Orgassa [26, 30] ($x = 0.23$ and $x = 0.51$) , Börjesson [32] ($x = 0.3$), and own data from the fit of Fig. 2.6 ($x = 0.4$).

$CuIn_{1-x}Ga_xSe_2$ data of Paulson ($x = 0.31$) Orgassa($x = 0.21$ and 0.51) and Börjesson ($x \approx 0.3$) are shown in Fig. 2.8; the result of the fit of Fig. 2.6 ($x \approx 0.4$) is also included. Similar differences between data as for $x = 0$ are observed for both n and k: Börjesson's n-values are lower, Orgassa's and Paulson's n-values agree well, although Orgassa's values increase for short λ and show a branch-point-induced hump (this time around 1300 nm for $x = 0.21$). As can be seen from the two Orgassa data sets, the Ga content only has a minor influence on n between 500 nm and 1000 nm. My n-values are in between Orgassa/Paulson and Börjesson. Higher n with respect to Börjesson can be explained smaller influence of surface roughness with a thinner film. Lower n with respect to Orgassa can partly be explained by the reflectance correction (no reference sample needed with the single-beam instrument), but higher surface roughness (not measured) or surface oxidation could also contribute. As for the k-values, it can again be observed that from ellipsometry (Paulson, Börjesson) $k > 0$ also for subbandgap wavelengths, while RT-results show a decrease to that $k \approx 0$ at the bandedge. When the difference in Ga content is accounted for, my k-values are in good agreement with Orgassa's results, which can be seen from comparison with his data for $x = 0.5$ (open circles). Close inspection reveals some difference in the shape of $k(\lambda)$ close to the bandgap, which, as discussed in Orgassa's thesis, can be related to the form of the Forouhi-Bloomer dispersion used; a more appropriate dispersion relation for $Cu(In,Ga)Se_2$ has been proposed by Djurisič and Li [33]. Nevertheless, It seems that my data from the fit in Fig. 2.6 are accurate enough for the purpose they have been used in Paper IV, namely to simulate the trends in total generation as a function of absorber thickness for different back contacts.

In addition to the influence of the surface properties already discussed, differences in bulk properties might contribute to discrepancies between data. In particular, the *density* of the films can differ between samples. Lower density is expected for thin films relative to bulk material, which could contribute to the decrease in k-values for thin films relative to the k-values of Alonso in Fig. 2.7. When we compare thin (sub-micron) CIGS layers simultaneously deposited on glass and on Mo substrates, the XRF counts for the elements (proportional to the number of atoms per area unit) are similar (as expected), but the layers on glass are consistently thicker and have higher surface roughness. This implies that the density is lower for the films on glass than for the films on Mo, an effect that is probably related to a difference in substrate temperature. For this reason, the data by Paulson *et al.*, obtained for films grown on Mo substrates to standard thickness, are probably the most accurate for device-quality CIGS for photon energies well above the bandgap.

However, close to the bandgap the error in k-values obtained from RT-measurements is small, while it appears significant for ellipsometry. From a device modelling point of view, the k-values close to the bandgap are most important for the total generation current. For light with higher photon energy (short wavelength), absorption is so high that, for standard absorber thickness, this light will be absorbed independent of the exact k-value.

In conclusion, I suggest the following regarding the optical properties of thin-film $CuIn_{1-x}Ga_xSe_2$

- Differences in method (ellipsometry vs. RT) as well as difference in bulk and surface properties of the films analysed should be considered when comparing different data sets.
- For photon energies well above the bandgap, the data from Paulson *et al.* [29] are the most accurate available, since the smooth back surfaces of standard-thick films were characterized.
- For device simulation, the data from Orgassa *et al.* [30] are preferable, because (i) the RT-method yields higher accuracy in the absorption coefficient for photon energies in the critical bandgap region and (ii) a practical parametrization of the data as a function of Ga content x has been given in Orgassa's thesis [26].
- The optical data used for simulations in Paper IV and in this thesis are accurate enough for the purpose they have served. k-values compare well with Orgassa's data for similar Ga content.

2.3.4 CBD-CdS buffer layer

Material properties of CdS grown by chemical bath deposition (CBD) strongly depend on the CBD recipe and the substrate used. The strong process dependence arises from the complexity of the chemical system, in which several

growth mechanisms can be effective in parallel [34].

In particular, the process dependence is important for the optical properties of the resulting film. While the determination of optical properties of films on glass substrates is fairly straightforward, its relevance for modelling of Cu(In,Ga)Se_2 devices can therefore be questioned. It would be more interesting to determine the optical properties of CdS grown on device quality Cu(In,Ga)Se_2 films. This is experimental task is not straightforward, and, to my knowledge, not yet accomplished. First, it requires that the optical properties of the underlying CIGS (and Mo) layer(s) be known or determined. Second, the surface roughness of the CIGS layer is typically of the same order of magnitude as the thickness of the CdS layer. This makes it harder to independently measure the CdS thickness, and significantly complicates the analysis of any ellipsometric or spectrophotometric data.

Having this task yet to accomplish in mind, I will in the following introduce literature data on bulk and thin film CdS, describe some result from my optical characterisation of CBD-CdS on glass substrates, and, finally, discuss how properties of CBD-CdS on CIGS can be expected to relate to existing data and how these properties could be determined.

General properties and literature data

Cadmium sulphide is a semiconductor with an optical bandgap around 2.4 eV (515 nm). It crystallizes both in hexagonal closed-packed (wurtzite) structure and cubic *fcc* (zinc-blende) structure; the hexagonal structure is slightly ($\sim$1 meV/atom) more stable [35]. In thin films of CdS prepared by CBD, both structures are normally present, see, e.g., Refs. [36, 37]. The fundamental gap is attributed to transitions at the Γ point in the centre of the Brillouin zone (3D M_0 critical point) [38].

The optical properties of bulk CdS have been measured many times. A good reference source is the CdS chapter in Handbook of optical constants of solids (II) [39], but there are also many newer publications available, for instance by Ninomiya and Adachi [38]. As reference values for (hexagonal) single crystals I have chosen from Ref. [39] the data from Cardona and Harbeke [40] for $\lambda < 650$ nm, and the data from Bieniewski and Czyzek [41] for $\lambda \geq 650$ nm.[1] Thin film values are tabulated in [39] from the work of Khawaja and Tomlin [42] (note the corrections in HOC vol. III [43]). They determined the optical properties of evaporated thin films of CdS (and ZnS) in the range 250-2500 nm from reflectance and transmittance measurements, including the effect of surface roughness into their model. The values obtained were slightly lower than for bulk materials, but increased with increasing substrate temperature. Another thin film reference is the ellipsometric determination by Mathew, Mukerjee, and Vijayakumar [44] of n and k of spray-pyrolysed films in the range

[1] In both cases the ordinary component.

530–600 nm. They also found refractive index lower than bulk values and increasing with substrate temperature, along with increased crystal quality and decreased surface roughness.

Although optical properties are mentioned in numerous articles about CBD-CdS, the complex refractive index is rarely discussed. Basol, Kapur, and Halani [45] compared CdS buffers prepared by evaporation and CBD. For films on glass substrates, they measured the refractive index using ellipsometry and found lower values for CBD-CdS ($n = 1.8 - 2.0$) compared to for evaporated layers ($n = 2.3$), which could explained the lower (average) reflectance measured. In the short paper by Mahanty *et al.* [46], n-values between 1.6 and 2.2 (at an unspecified wavelength) are reported for CBD-CdS films prepared with varying concentrations of $CdSO_4$ and thiourea. The best data so far available for CBD-CdS on glass is probably found in the thesis of Kay Orgassa [26]. He determined the refractive index of samples prepared using the a recipe for high performance CIGS cells, but with the deposition time reduced from five to four minutes, and the deposition procedure repeated three times; the purpose was to avoid the cluster growth mechanism and still get a film thickness comparable what he obtained on CIGS (about 80 nm).

Own results for CBD-CdS on glass

Paper I– process dependence

The process dependence of the optical properties of CBD-CdS is highlighted in Paper I, where we show that the optical properties of CBD-CdS grown on glass using our baseline recipe vary as a function of process time. We relate the variation in optical properties to variations in both *composition* and *density* of the film, as obtained from measurements of (geometrical) thickness using profilometry and interferometry, and of atomic thickness (in atoms/cm^{-3}) of Cd and S using Rutherford Backscattering Spectrometry (RBS) and X-ray fluorescence (XRF). In addition we observe a difference between films grown on glass and on Al_2O_3.

The variation in optical properties was successfully modelled with an effective medium approximation (EMA), considering the layer a uniform mixture of compact CdS and void. According to the Brüggeman EMA [47] used, the resulting dielectric function ε_{eff} is given by the relation

$$(1 - f_v)\frac{\varepsilon_M - \varepsilon_{eff}}{\varepsilon_M + 2\varepsilon_{eff}} + f_v\frac{\varepsilon_p - \varepsilon_{eff}}{\varepsilon_p + 2\varepsilon_{eff}} = 0, \qquad (2.15)$$

where $\varepsilon_M = 1$ is the dielectric function of the matrix material (void) and $\varepsilon_p = \varepsilon_{CdS}$ is the dielectric function of the particle material (CdS without voids), and f_v is the volume fraction of the particle material. This is a crude model: only two free parameters, the volume fraction of CdS and the thickness of the model layer, are used for fitting the measured reflectance and transmit-

tance spectra at all wavelengths; the properties of the particle material are considered independent of volume fraction and grain size, which is not to be expected part of the matrix material is most probably different from void, for instance a compound containing Cd but not S. Considering these limitations, the consistence with the independent measurements of film thickness and volume fraction is surprisingly good. The volume fraction found for the thicker films is also in good agreement with packing density[2] reported by Mathew [44] and Mahanty [46].

Refractive index and dispersion relation

A more precise determination of the optical properties of our CBD-CdS on glass was made for samples prepared with a slightly modified procedure compared to our baseline recipe (cf. Paper I); the solution of cadmium acetate is added to the ammonia, and this solution is then filtered into the reaction beaker before the thiourea is added. Compared to the standard procedure this tends to result in films that are harder (more resistant to scratches) and less scattering. A possible explanation would be that filtering removes colloids of $Cd(OH)_2$, and thus suppresses the growth mechanism induced by these colloids, see [34] ch. 2-3. Note that filtering with coarser filters did not have the same effect.

Before optical characterisation, the CdS deposited on the back side of the sample was etched away with diluted HCl. A Perkin-Elmer λ900 system was used to measure transmittance, T, and front and back side reflectance, R and R_b, from 300 nm to 1500 nm with 10 nm step. Both total and diffuse signals were measured. The diffuse component was small ($R_{diff} < 0.3$ %), so the specular Al reflectance reference (restricted to $\lambda \geq 350$ nm) could be used. Measured total T, R, and R_b are shown in the left graph of figure 2.9.

Assuming flat surfaces and a homogeneous film, complex refractive index was determined by a point-by-point fit and by fitting of a dispersion relation; the result was practically identical with both methods. Based on fitting of bulk reference data, the dispersion relation was chosen on the following form:

$$\varepsilon_{CdS}(E) = \varepsilon_\infty + \chi_{DE}(E, R, E_0, A_0, \Gamma_0, \alpha_0) + \chi_{TL}(E, E_g^{TL}, E_1, A_1, \Gamma_1). \quad (2.16)$$

In this expression, χ_{DE} denotes a Djurišić-Elliott oscillator [48] that accounts for the fundamental gap transitions, including excitons. χ_{TL} represents a Tauc-Lorentz oscillator [49] that accounts for the dispersion in the visible region caused by the transitions around 5-6 eV (c.f. Ref. [38]), and ε_∞ is a real constant that accounts for the contribution to ε_1 of all higher-lying transitions. The numerical values obtained for the parameters are given in Table 2.1.

With this dispersion it is possible to nicely model measurement data. This is illustrated by the agreement between measured and modelled RT-spectra in

[2] p, defined by $n_{film} = pn_{bulk} + (1-p)n_{void}$.

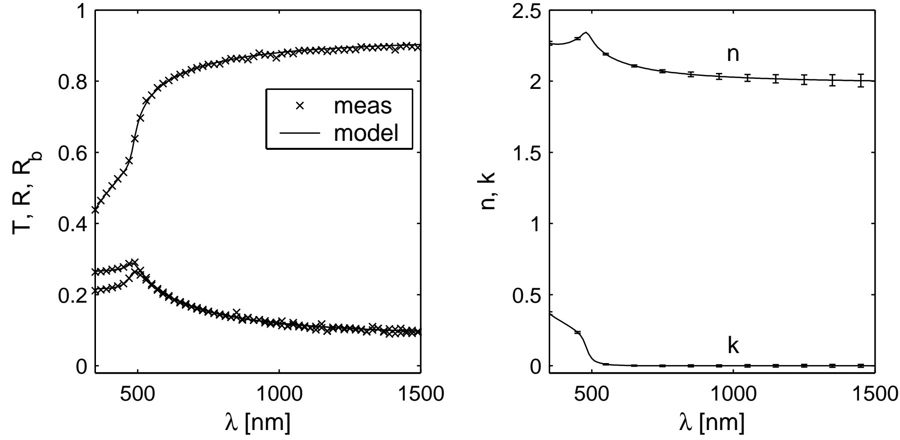

Figure 2.9: Left: Measured and modelled transmittance (T), and front (R) and back side (R_b) reflectance. Right: $n(\lambda)$ and $k(\lambda)$ from dispersion analysis with error estimates indicated.

Table 2.1: *Results from fitting of the CdS dispersion in Eq. 2.16 and film thickness d to measurement data of Fig. 2.9.*

	Unit	Value		Unit	Value
ε_∞	[-]	0.83	E_g^{TL}	[eV]	2.31
R	[eV]	0.017	E_1	[eV]	5.77
E_0	[eV]	2.61	A_1	[eV]	40.7
A_0	$[(eV)^{1.5}]$	18.9	Γ_1	[eV]	3.43
Γ_0	[eV]	0.08			
α_0	[eV]	0.0			
d	[nm]	38			

the left graph of Fig. 2.9. The right graph shows the optical data obtained. The error bars have been calculated according to Ref. [17]. In the visible region ($\lambda < 850$ nm), the absolute and relative measurement error were modelled with a wavelength distribution determined from repeated noise measurements and scaled to an average of 0.25% each. In the NIR region ($\lambda \geq 850$ nm) a constant error of 0.5% was used, since instrument problem has resulted in un-usually high noise level. With these error estimates, a value $\chi^2 = 0.9$ was obtained as measure of the quality of the fit, c.f. [50].

It might be argued that the number of free parameters (10 in the dispersion + film thickness, making a total of 11) is too high for the relatively simple spectral dependence (dispersion) observed. In particular, it is almost impossible to ensure that the optimization algorithm converges to the globally best set of parameter values. Therefore, any assignment of parameter values to real

physical parameter properties should be made with utmost care. On the other hand, it is useful to use a dispersion relation which is flexible enough to accommodate most details in the spectra of the bulk materials. Starting from, and comparing with, established parameter values for the bulk materials helps finding thin film values that are physically sane. For example, the increase of the E_0 value of the fundamental gap from 2.5 eV [38] to 2.6 eV (this sample) probably reflects a real bandgap widening. Likewise, an increase in Γ values obtained is to be expected for thin-films. Furthermore, the dispersion has a practical value also when the parameters found do not represent the globally best fit nor have a physical meaning, and for improved convergence it is quite possible to fit only a subset of all parameters.

Data comparison

The refractive index data shown in Fig. 2.9 ($n = 2.02$ at 1000 nm) are low compared to bulk values, slightly lower than Orgassa's data ($n = 2.17$ at 1000 nm), and in the high end of the range given in Ref. [45]. As for the films in Paper I(deposited without filtering of the solution), n is lower for all single dip films, and similar for the double dip film. The main reason for Orgassa's higher n is most probably the modified deposition procedure, enhancing ion-by-ion growth. In addition, the reflectance values used for the determination were taken under the assumption of 100% reference reflactance [26]. Reference correction will yield slightly lower $R(\lambda)$ and result in slightly lower n.

In figure Fig. 2.10 the dielectric function taken from literature data for single crystal, evaporated thin films and the CBD-CdS of Orgassa are compared with the dispersion fit. The general trend between the four datasets is de-

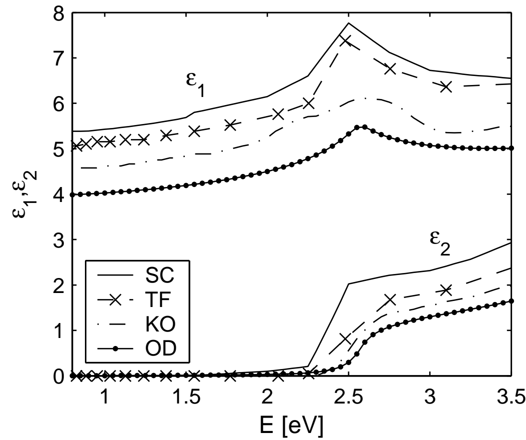

Figure 2.10: Real part ε_1 and imaginary part ε_2 of the dielectric function of CdS. Literature data for single crystals (SC, [40, 41]), evaporated thin films (TF, [42]), and CBD-CdS by Kay Orgassa (KO, [26]) are compared with own data (OD).

creasing $\varepsilon(E)$ and increased optical bandgap.

Now the question comes to what can be expected for the optical properties of CBD-CdS on CIGS. First, we know that the film grows thicker on CIGS than on glass; with our 7.5 min baseline process the Cd signal measured by XRF is about double for CdS on CIGS. This can be understood in terms of a decreased incubation time. Fig. 1 in Paper Iindicates an incubation time on glass of about 4 minutes; on the CIGS surface there are nucleation sites available from the beginning, which can reduce the incubation time to almost zero. Second, the difference in nucleation and available number of reaction sites can be expected to favour ion-by-ion growth over hydroxide cluster growth mechanism, which affects the composition, density and structure of the film. In particular, the colloidal growth increases with time, and a short incubation time therefore favours ion-by-ion growth. Epitaxial growth of CBD-CdS, indicative of ion-by-ion growth, has been confirmed on single crystal $CuInSe_2$ [36], and transmission and scanning electron microscopy of CBD-CdS on CIGS typically reveals a compact-looking films that conformally cover the surface of the $Cu(In,Ga)Se_2$ grains.

The above suggest that the optical properties of CBD-CdS on CIGS, compared to on glass, should be closer to the reference values for bulk and thin films evaporated at high substrate temperature. One might speculate that Orgassa in his first dip of the characterized samples created a nucleation layer that has a similar impact on the growth as a CIGS surface. My guess would therefore be that optical properties of CBD-CdS on CIGS are similar to Orgassa's data in magnitude, and retains the shape given by the proposed dispersion relation. To settle this question experimentally, one approach would be to include the effect of surface roughness in the optical model. Another option would be to produce CIGS surface smooth enough to make scattering negligible. This can be accomplished by mechanical polishing, chemical etching [51], epitaxial growth on crystalline substrates [36], or simply by making the CIGS layer thin enough. The first approach has the advantage that the sample preparation is not changed from the solar cell baseline, and the disadvantage of being more sensitive to model errors; the opposite holds for the second approach. In any of these, an appropriate dispersion relation for CdS should be helpful.

2.3.5 ALD-In_2S_3 buffer layer

In Paper IIwe made an optical characterisation of ALD-In_2S_3 deposited on glass substrates. n and k were extracted from a point-by-point fit of R, T and R_b spectra, using an optical model where the effect of surface roughness was modelled with a Brüggeman effective medium approximation. >From the wavelength dependent absorption coefficient so obtained, we concluded

an indirect bandgap of about 2.1 eV independent of film thickness, substrate temperature and Na content of the substrate. Here, I will show that a dispersion relation based on an indirect bandgap is sufficient for reproducing the measured optical properties n and k in the range 1.5–3.5 eV. However, band structure considerations and some literature data rather suggest that the nature of fundamental optical bandgap is direct, but forbidden by selection rules.

Refractive index and dispersion relation for ALD-In_2S_3 on glass

It is first worth pointing out that without taking surface roughness into account in the optical model, it was not possible to reproduce measurement data obtained Paper II. This is illustrated in figure Fig. 2.11, where simulated R, T, and R_b are plotted for different thickness of the model roughness layer. Note that in a simpler model not including a roughness layer, $R \geq R_b$ for all

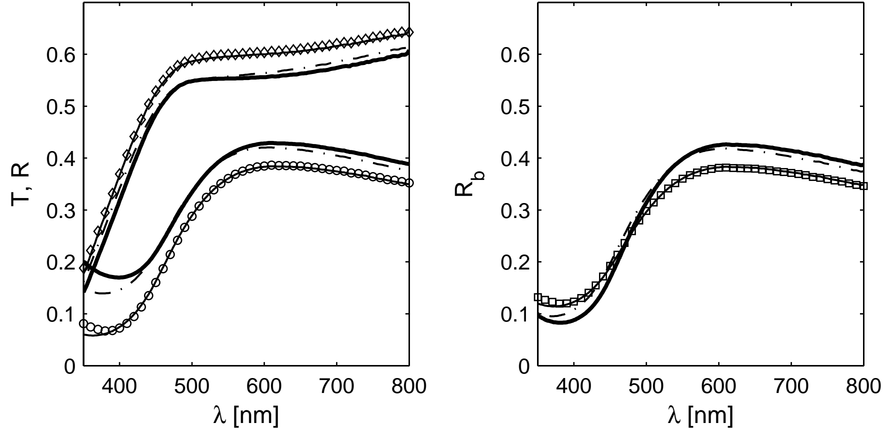

Figure 2.11: Illustration of the effect of surface roughness. Symbols show experimental data (same as in Fig. 5b in Paper II); transmittance (T, diamonds) and front side reflectance (R, circles) in the left graph, and back side reflectance (R_b, squares) in the right graph. The simulations shown are made for three different values of the thickness s of the roughness layer, while keeping the optical properties and the average film thickness, $d_{av} = d_{fit} + s_{fit}/2$, constant: $s = 0$ (thick solid lines), $s = 0.5s_{fit}$ (dash-dotted lines), and $s = s_{fit}$ (thin solid lines).

wavelengths, which is conflict with measurement data.

For our films, the assumption of one indirect bandgap is enough to reproduce not only the absorption coefficient throughout the measurement range 1.5–3.5 eV (see Fig. 6 in Paper II), but also the refractive index. The optical properties can be modelled with a standard dispersion relation for indirect bandgap [52], having only 5 parameters including ε_∞:

$$\varepsilon_{In_2S_3}(E) = \varepsilon_\infty + \chi_{id}(E_{id}, A_{id}, \Gamma_{id}, E_c). \tag{2.17}$$

Here, E_{id} is the indirect bandgap energy, A_{id} is the strength of the transition, Γ_{id} a broadening parameter, and E_c models a cut-off energy related to the finite width of the (parabolic) bands assumed to take part in the transition, see Ref. [52].

Fig. 2.12 shows the optical properties obtained when this model was simultaneously fitted to experimental R, R_b and T of three samples with ALD-In_2S_3 on SL glass, deposited with 1000 ALD cycles. The dispersion result is in good agreement with a point-by-point fit for the same samples.

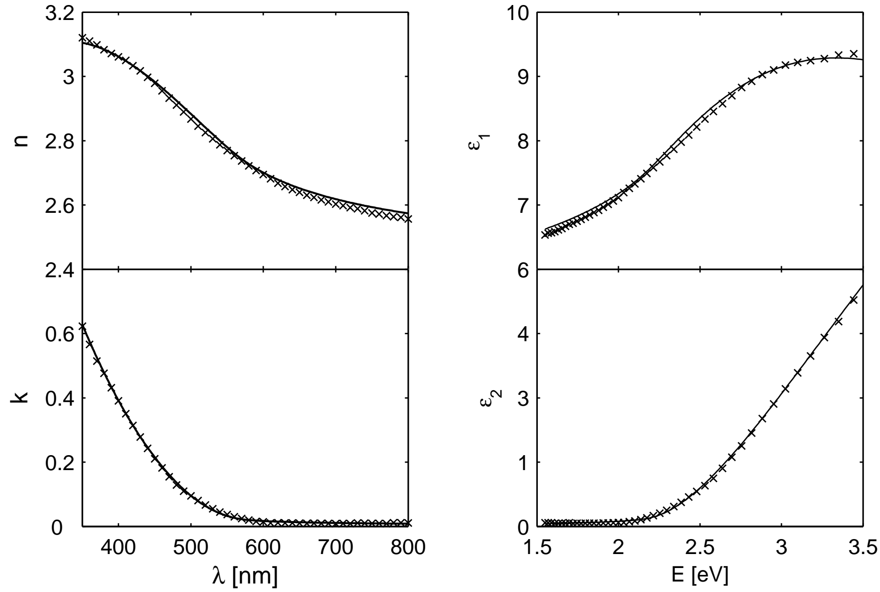

Figure 2.12: Optical properties ALD-In_2S_3 determined by point-by-point fit (symbols) and dispersion fit (lines) for 3 samples on SL glass (1000 ALD cycles, $T_{sub} = 160°C/200°C$): $n(\lambda)$ and $k(\lambda)$ (left); $\varepsilon_1(E)$ and $\varepsilon_2(E)$ (right).

Fitted parameters with estimated 90% confidence limits are shown in Table 2.2. The two thickness parameters d_c, thickness of compact film, and s, thickness of model roughness layer were also fitted, making the total number of fit parameters $M = 11$.[3] The measurement error was modelled with wavelength dependent distributions for absolute and relative errors, normalized to an average of 0.25% each. The model errors were below 0.5% absolute througout the spectrum and the minimum reduced χ^2 was 0.34, which implies (i) that the fit was good and (ii) that the assumed errors were too large; to get $\chi^2_{red} = 1$ the measurement errors should be decreased by a factor 1.7.

[3]With 226 data points in each spectrum, the total number of data points in the fit equalled $N = 3 \times 3 \times 226 = 2034$, and the degrees of freedom for the χ^2 distribution was then $r = N - M = 2032$.

Table 2.2: *Results from fitting of the ALD-In_2S_3 dispersion in Eq. 2.17,thickness d_c of compact film and thickness s of model roughness layer to measurement data of three differentALD-In_2S_3/glass samples.*

	Unit	Value	$\pm c_{90\%}$		Unit	Value	$\pm c_{90\%}$
ε_∞	[-]	0.68	0.40	d_{c1}	[nm]	28.3	0.6
E_{id}	[eV]	2.16	0.01	s_1	[nm]	10.3	0.9
A_{id}	[-]	25.61	0.56	d_{c2}	[nm]	32.0	0.7
Γ_{id}	[eV]	0.047	0.003	s_2	[nm]	17.4	0.7
E_c	[eV]	8.22	0.39	d_{c3}	[nm]	23.7	0.6
				s_3	[nm]	6.8	1.1

The relatively large uncertainty in ε_∞ and E_c is related to their strong correlation, which is shown in Table 2.3.

Table 2.3: *Normalized covariance matrix elements for dispersion fit parameters of ALD-In_2S_3.*

Param.	E_{id}	A_{id}	Γ_{id}	E_c
ε_∞	0.22	0.50	0.00	-0.98
E_{id}		0.70	0.62	-0.34
A_{id}			0.38	-0.63
Γ_{id}				-0.07

Measurement data were well reproduced with this dispersion also for the thicker films. The maximum model error was 2%, which is low but significantly larger than the measurement error. It was found that (not-so-dramitic) failure of the model in this case was correlated to low levels of light scattering at shorter wavelengths ($\lambda < 550$ nm). In addition, when the thickness of the roughness layer is $\sim$30 nm it makes a significant fraction of the shorter wavelengths, which violates the validity of the EMA model for the roughness layer. Thus, overall, this dispersion based on indirect bandgap seems compatible with our measurement data. But is it physically sound?

Discussion on the magnitude and nature of the optical bandgap of β-In_2S_3

A discussion on the nature of fundamental optical gap naturally starts at the crystal structure and the resulting electron band structure. Thin films of indium sulphide deposited by ALD are reported to have the crystal structure of β-In_2S_3 [53–56]. This *spinel* structure is interestingly complex: The chemical formula can be written $\{In(t)_{\frac{2}{3}}\square\}In_2(o)S_4$, where In(t) and In(o) represent tetrahedrally and octahedrally bounded In atoms, respectively, and $\square$ repre-

sents a vacant site.[4] All chemical bounds are satisfied, and still 4 out of the 84 lattice sites in the unit cells are empty.[5] The large number of atoms in the unit cell can explain why there, to my knowledge, is no publication available giving a theoretically calculated band structure diagram of β-In_2S_3. There are a few publications that show calculated valence and conduction band density of states (DOS) [57, 58], and these data have been compared with X-ray absorption spectra [57, 59]. Lavrent'ev *et al.* [57] found in their comparison good agreement both for β-In_2S_3 and the analogue material $CdIn_2S_4$. This latter spinel compound has actually been more thoroughly studied with regards to band structure and optical properties than β-In_2S_3; band structure calculations [60, 61] suggest that the lowest optical interband transition of $CdIn_2S_4$ is of indirect nature, followed by direct transitions at the Γ point of the Brillouin zone, and this picture agrees well with an experimentally found indirect bandgap at 2.3 eV [62], followed by a direct allowed transition around 2.65 eV [62, 63], and then structures at 3.0 eV, 4.5 eV and 6 further energies in the deep UV [see 63, Table 2]. The analogy with $CdIn_2S_4$ should be helpful when optical properties of β-In_2S_3 are to be analysed.

Bandgap determinations for β-In_2S_3, done with varying methods and varying quality, are abundant in the literature; very little is published on the optical functions n and k. Selected references on the bandgap are summarized in Table 2.4. In a first group of references [53, 64–73] and Paper 1 (Pcds), all bandgap values fall in the range 2.0–2.3 eV, but there is disagreement on the nature of the transition. This group covers both bulk materials and thin films, and different methods for bandgap determination. In a second group of references [54–56, 74, 75] , significantly higher bandgaps $\geq$ 2.7 eV of direct and allowed nature are claimed for thin films, based on approximate expressions for the absorption coefficient $\alpha(E)$ and plots of $(\alpha E)^2$ vs. E.

The differences between the references can at least partly can be explained by errors induced by the approximations for α. Two variants are commonly used,

$$\alpha(E) = -\frac{1}{d}\ln\left[\frac{T}{(1-R)^2}\right] \quad (2.18)$$

$$\alpha(E) = -\frac{1}{d}\ln[T] \quad (2.19)$$

[4] In β-In_2S_3 the vacant sites are ordered, while in α-In_2S_3 they are randomly distributed.

[5] This could be expected to facilitate diffusion of other elements; diffusion of Cu and Na has been into ALD-In_2S_3 buffers in CIGS solar cells has been reported [55] and is probably important for the device performance.

Table 2.4: *Selected references on the optical bandgap of β-In_2S_3. Types: da = direct allowed, df = direct forbidden, ida = indirect allowed. For explanation and implications of α-methods, see text. (?) marks that the method was not clearly stated.*

Sample type	α- method	E_g-method	E_g [eV]	Type	Authors	Comment	Year	Ref.
Single crystal	$\ln[\frac{T}{(1-R)^2}]$ (?)	$(\alpha E)^{2/3}$ vs E	2.03	df	Rehwald and Harbeke	Evap. films for E>2.8 eV	1965	[64]
Single crystal	$\ln[T]$ (?)	α^2 vs E	2.0	da	Kambas *et al.*		1985	[65]
Single crystal	-	$(I_{ph})^2$ vs E	2.0	-	Becker *et al.*	Photoelec. cell	1986	[66]
Powder	-	$I_{ph}(E)$	1.97	-	Bube and McCarrol	Max in A/W	1959	[67]
Powder	-	max in $\frac{dR}{d\lambda}$	2.1	-	Gorai *et al.*		2003	[68]
Evap. thin films	$\ln[\frac{T}{(1-R)^2}]$	$(\alpha E)^2$ vs E	2.1	da	Barreau *et al.*	R taken constant in [69]	2001	[69, 70]
OM-CVD thin film	$\ln[T+R]$ (?)	$(\alpha E)^2$ vs E	2.0	da	Nomura *et al.*	”absorption meas.”; Fig. 6 values very low.	1991	[71]
Spray pyr. thin film	$\ln[T+R]$ (?)	$(\alpha E)^{0.5}$ vs E	2.2	ida	Kim and Kim	”absorption meas.”	1986	[72]
SILAR thin film	$\ln[T+R]$ (?)	$(\alpha E)^2$ vs E	2.3	da	Mane and Lohande	Linear region not clear	2002	[73]
Spin coat. coll. thin film	$\ln[T+R]$ (?)	$(\alpha E)^2$	2.0-3.5	da	Yasaki *et al.*	”quantum size effects”	1999	[76]
CBD thin film	$\ln[T]$ (?)	$(\alpha E)^{0.5}$ vs E	2.0	ida	Sandoval-Paz *et al.*	Linear region not clear	2005	[77]
		$(\alpha E)^2$ vs E	2.5	da		Linear region not clear		
CBD thin film	$\ln[T+R]$ (?)	$(\alpha E)^2$ vs E	2.75	da	Lokhande *et al.*		1999	[74]
ALD thin film	$\ln[T]$ (?)	$(\alpha E)^2$ vs E	2.3	da	Asikainen *et al.*	d, and n in transp. reg. obtained using [78]	1994	[53]
ALD thin film	-	$T(\lambda)$	3.25	-	Yousfi *et al.*	”absorption onset”;	2000	[75, 79]
			2	-		after annealing	2001	[79]
ALD thin film	-	drop in QE	2.7-2.8	-	Naghavi *et al.*	”apparent bandgap”	2003	[55]
ALD thin film	-	$T(\lambda)$	2.7	-	Spiering *et al.*	”by analysis of transm.”	2003	[54]
ALD thin film	$\ln[T]$	$(\alpha E)^2$ vs E	2.7	da	Naghavi *et al.*		2004	[56]
quasi-ALD thin film	$\ln[\frac{T}{(1-R)^2}]$ (?)	$(\alpha E)^2$ vs E	2.6–3.0	da	Guillén *et al.*	”quantum size effects”	2004	[80]
ALD thin film	RT-inv.	$(\alpha E)^{0.5}$ vs E	2.1	ida	Sterner *et al.*	Alt. type df, see text	2005	Paper II

These are both based on the expression for the transmittance of a slab of material 1 with thickness d between media 0 and 2:

$$T = T_{02} = \frac{T_{01}T_{12}e^{-\alpha d}}{1+R_{01}R_{12}e^{-2\alpha d}}, \tag{2.20}$$

where T_{ij} (R_{ij}) is the transmittance (reflectance) of the interface between media i and j for light coming from medium j. For a thin film on a substrate, this is already an approximation since interference and substrate/air reflections are not considered. If medium 2 is the same as the incident medium 0, $T_{12} = T_{01} = (1-R_{01})$. Further, if the product αd is large (which also ensures that interference is not important), the denominator is approximately equal to 1 and we get

$$T \approx (1-R)^2 e^{-\alpha d}, \tag{2.21}$$

which can be transformed to Eq. 2.19 since in this case $R \approx R_{01}$; the approximation in Eq. 2.19 is obtained by also neglecting the factor $(1-R)^2$, which for a constant R only changes the magnitude but not the shape of $\alpha(E)$.

For thin films, the condition $\alpha d >> 1$ for strong absorption is often not met. This is illustrated in Fig. 2.13, using T and R data for two of our samples, deposited with 1000 cycles and 2000 ALD cycles, respectively. Clearly, the

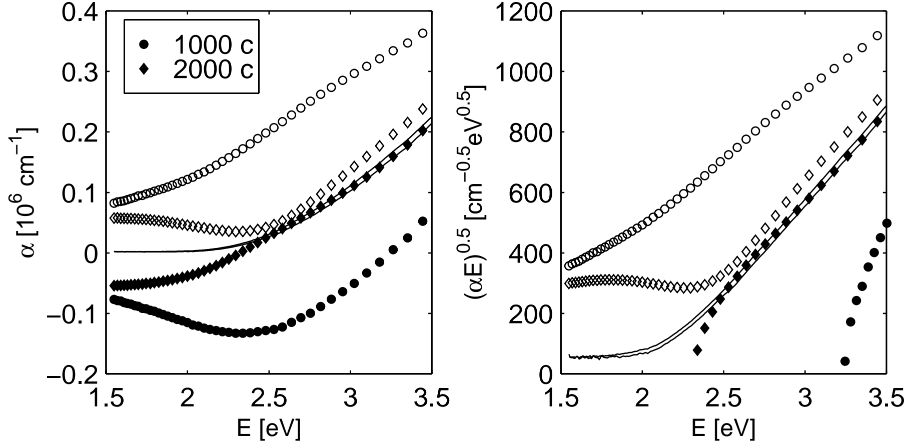

Figure 2.13: Left: Absorption coefficient $\alpha(E)$ (lines) determined for two samples of ALD-In_2S_3 on SL glass (1000/2000 ALD cycles, $T_{sub} = 160°C$), compared with results using approximation $\ln[T]$ (open symbols) and approximation $\ln[T/(1-R)^2]$ (closed symbols). Right: Errors in α induced by the approximations prevent the extraction of a 2.1 eV indirect bandgap of from a plot of $\sqrt{\alpha E}$ vs E.

approximations in Eq. 2.19 and 2.19 result in large errors in α, in particular for the thinner film. As shown in the right graph, this makes proper extraction of a 2.1 eV indirect bandgap impossible. Another problem in some of the ref-

erences is that a direct allowed transition is claimed from linearity of $(\alpha E)^2$ vs E, also when no clearly linear region is demonstrated – see for example Fig. 3 in Ref. [73]. For these two reasons, the high bandgaps claimed in the second group appear not adequate for the fundamental gap, although they might possibly reflect higher direct transitions.

The most thorough determination for single crystal β-In_2S_3 seems to be the one in the paper by Rehwald and Harbeke [64], which primarily concerns the conduction mechanism. With samples of up to 4 mm in thickness (interference lost) they have probably used Eq. 2.20,[6] alternatively the approximation of Eq. 2.19 which in this case is applicable for α down to ~ 10 cm^{-1}. They found for all crystals (with varying composition and resistivity) a fundamental absorption edge at 2.0 eV. Since energy dependence of $\alpha(E)$ in the range 10^3 cm^{-1}–10^4 cm^{-1} could be described by

$$\alpha(E) = A\frac{(E-Eg)^{3/2}}{E} \tag{2.22}$$

they concluded a direct forbidden transition. In addition they found an absorption structure at 2.45 eV, the nature of which they could not determine, and, for the most highly resistive samples, a very weak ($\alpha < 10$ cm^{-1}) transition at about 1 eV,[7] which was covered by free-electron absorption in the more conductive samples.

With α for our samples, it is possible to identify at least one clearly linear region (2.55 eV–3.25 eV) in a plot of $(\alpha E)^{2/3}$ vs E. As we mentioned in Paper II, this linear region extrapolates to a bandgap of about 2.3 eV for all samples. (As we also mentioned in Paper II, a plot of $(\alpha E)^2$ vs E for direct allowed transitions yields no clearly linear regions at all.) However, if it is assumed that there is another direct forbidden transition giving rise to the fairly linear behaviour in the range 2.25 eV–2.45 eV, the two resulting bandgaps are 2.06 eV and 2.57 eV, respectively. This is in fair agreement with the results of Rehwald and Harbeke [64], and in line with what could be expected from the band structure published for $CdIn_2S_4$. It should definitely be possible to reproduce the optical properties with a dispersion relation based on two direct forbidden transitions. However, this would add more fit parameters, and with our thin films with rough surfaces, the lack of sharp structures results in a large correlation uncertainty in these parameters; clearly, characterisation of the transition energies is better done on well defined samples with sharp surfaces and large grains, and should be compared with theoretical results from band structure calculations.

To conclude, a dispersion based on a single indirect bandgap at 2.1 eV is

[6]"The absorption constant was calculated with the correction for reflectivity determined from long-wavelength refractive index of 2.56."

[7]In agreement with the activation energy of intrinsic conduction.

sufficient to explain the observed optical properties in the range 1.5–3.5 eV. However, comparison with results for single crystal β-In_2S_3 hint that direct forbidden transitions at about 2.1 eV and 2.6 eV provides a better physical description.

2.3.6 RF-sputtered ZnO buffer layer

ZnO has a wurtzite (hexagonal) crystal structure. The optical properties for photon energies up to 5 eV are dominated by the transitions at the direct bandgap at about 3.3 eV [81, 82]. As will be illustrated here, the optical properties of thin-film ZnO prepared by RF-sputtering are fairly similar to bulk values, except in the vicinity of the band edge.

The Perkin-Elmer λ900 system was used to measure transmittance, T, and front and back side reflectance, R and R_b, in the same way as described above for the CdS samples. The diffuse components of the spectra were confirmed to be negligible. Measured and modelled total T, R, and R_b are shown in the left graph of Fig. 2.14. The model spectra are calculated from a fit of a dispersion of the form

$$\varepsilon_{ZnO}(E) = \varepsilon_\infty + \chi_{DE}(E, R, E_0, A_0, \Gamma_0, \alpha_0), \quad (2.23)$$

where χ_{DE} just like for CdS is a Djurišić-Elliott oscillator [48] that accounts for the bandgap transitions; ZnO was the application for which χ_{DE} was developed in Ref. [48]. The parameter values obtained from the fit are shown in Table 2.5.

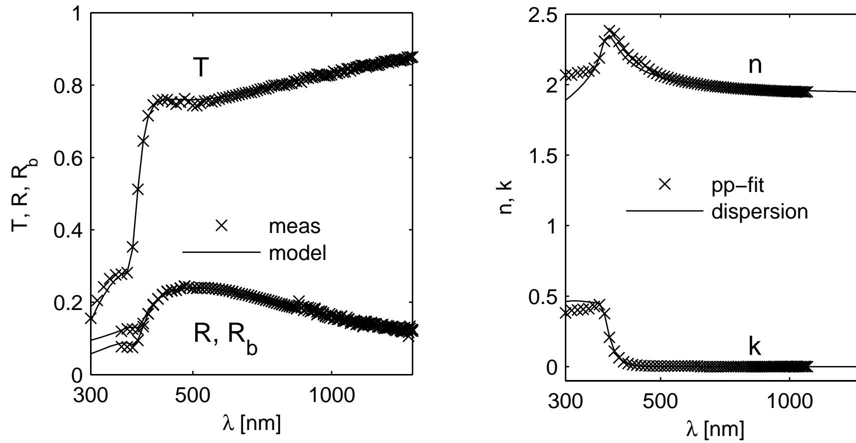

Figure 2.14: Left: Measured ('x') and modelled (lines) transmittance T and front side (R) and back side ($R_b, \leq R$) reflectance of RF-sputtered ZnO. Right: $n(\lambda)$ and $k(\lambda)$ from point-by-point-fit ('x') and dispersion fit (lines). Note that the wavelength scale is logarithmic to magnify the region around the bandgap.

Table 2.5: *Results from fitting of the ZnO dispersion in Eq. 2.23 and film thickness d to measurement data of Fig. 2.14.*

	Unit	Value
ε_∞	[-]	2.65
R	[eV]	0.11
E_0	[eV]	3.50
A_0	[(eV)$^{1.5}$]	27.0
Γ_0	[eV]	0.15
α_0	[eV]	0.08
d	[nm]	69.5

In the right graph of Fig. 2.14 the n-values and k-values obtained from the dispersion fit are compared with n-values and k-values obtained from a point-by-point fit for another ZnO sample prepared in the same way. The agreement is good for except for $\lambda < 350$ nm. In Fig. 2.15 the dielectric function obtained from the fit is compared with the single crystal data measured from Jellison and Boatner [81], measured by ellipsometry. The agreement is good except in the vicinity of the bandgap, where the single crystal data show much sharper structures with two distinct absorption peaks. Physically, the broadening in the thin film data is expected from the potential fluctuations caused by grain boundaries and other crystal defects. In terms of the fit parameters, the broadening is reflected in an increase of the parameter Γ_0 and a decrease of the parameter α_0 with respect to the fit of the data of Ref. [81] given in Ref. [48].

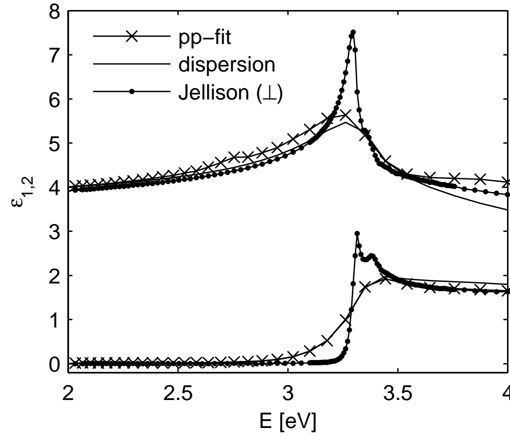

Figure 2.15: Real part ε_1 and imaginary part ε_2 of the dielectric function obtained for RF-sputtered ZnO obtained from point-by-point fit and dispersion fit, compared with reference data for single crystals (Jellison and Boatner [81], ordinary component $\perp$).

2.3.7 RF-sputtered ZnO:Al front contact layer

ZnO:Al contains ~ 1 atomic % Al. This adds a large number of free electrons in the conduction band. It can therefore be expected that the optical properties can be described by a dispersion

$$\varepsilon_{ZnO:Al}(E) = \varepsilon_\infty + \chi_{DE}(E,R,E_0,A_0,\Gamma_0,\alpha_0) + \chi_{Drude}(E,E_N,\Gamma_D), \qquad (2.24)$$

where χ_{DE} models the bandgap, as for ZnO in Eq. 2.23, and χ_{Drude} models the influence of the free electrons, as for ZrN in Eq. 2.13. According to the comprehensive investigation of the optical properties of sputter-deposited ZnO:Al by Jin, Hamberg, and Granqvist [83], which is advantageously read together with a corresponding paper about In_2O_3:Sn [84], this is almost the case. Two things are modified: (i) the bandgap absorption edge is smeared out and shifted to higher energies by the Al-doping, and (ii) the damping of the free electrons is dominated by ionized impurity scattering, which is not well described by the Drude model. However, the contribution from the free electrons can be approximately described by the Drude model if the damping coefficient, Γ_D, is allowed to vary with the photon energy.

Based on inspection of the energy-dependent damping deduced from point-by-point fits, I have assumed that the damping can be described by

$$\begin{aligned}\Gamma(E) &= \Gamma_{max},\ \text{for } E \leq E_1 \\ &= \Gamma_{min} + (\Gamma_{max} - \Gamma_{min})\frac{E_2 - E}{E_2 - E_1},\ \text{for } E_1 < E < E_2 \\ &= \Gamma_{min},\ \text{for } E \geq E_2,\end{aligned} \qquad (2.25)$$

i.e., by a linear variation in a transition region between two constant values. Measurements and dispersion fits of T, R and R_b for ZnO:Al/glass are shown in Fig. 2.16, corresponding to Fig. 2.14 for ZnO. It can be seen that the χ_{DE} dispersion is flexible enough to describe the bandgap region well, also when it is distorted by the doping. With the modified Drude term, the decrease in transmittance for long wavelengths caused by free electron absorption is also well described. The discrepancy between the model and the measurement data for the front and back side reflectance at long wavelengths, does not seem to be a failure of the dispersion relation. This is rather related to a depth gradient in the doping of the film; the resistivity of the ZnO:Al layers is observed to decrease with deposition time, an effect probably related to the availability of oxygen in the sputter process.

As seen in the right graph of Fig. 2.16, the free electrons cause the refractive index n to decrease and the extinction coefficient k to increase with increasing wavelength. The difference in optical properties with respect to ZnO is illustrated in Fig. 2.17 by the dielectric function determined for the two layers. The absorption edge is clearly shifted to higher energies and smeared out.

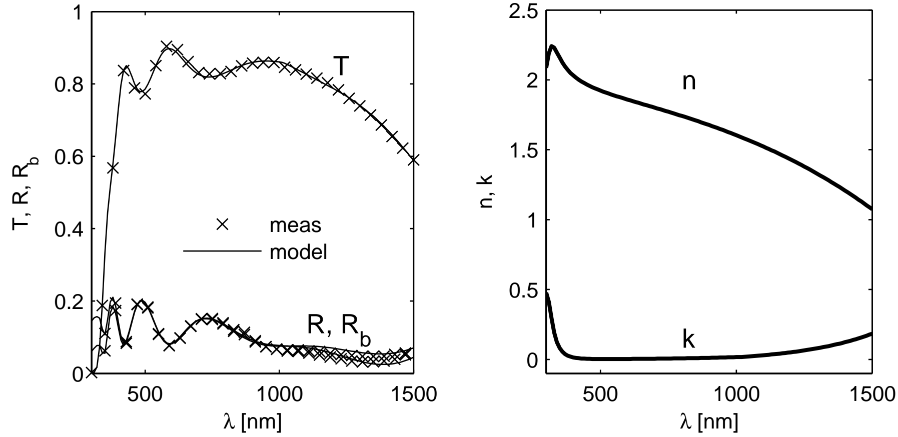

Figure 2.16: Left: Measured ('x') and modelled (lines) transmittance T and front side (R) and back side ($R_b, \leq R$) reflectance of RF-sputtered ZnO:Al. Right: $n(\lambda)$ and $k(\lambda)$ from dispersion fit. In contrast to the case of Fig. 2.14, the wavelength scales are here linear.

The parameters obtained in the fit for this sample are given in Table 2.6. The value of the unscreened plasma energy, E_N, can be used to estimate the carrier concentration n_e. According to the Drude theory, E_N is given by

$$E_N^2 = n_e \frac{q^2 \hbar^2}{\varepsilon_0 m_c^*}, \tag{2.26}$$

where m_c^* is the conduction-band effective mass. Using a reference value of $m_c^* = 0.28 m_0$ (as in Ref. [83]), yields $n_e = 3.7 \cdot 10^{20}$ cm^{-3}, which compares well with the values reported in Ref. [83].

Table 2.6: *Results from fitting of the ZnO:Al dispersion in Eq. 2.24 and film thickness d to measurement data of Fig. 2.16.*

	Unit	Value		Unit	Value
ε_∞	[-]	2.56	E_N	[eV]	1.35
R	[eV]	0.24	Γ_{max}	[eV]	0.18
E_0	[eV]	4.31	Γ_{max}	[eV]	0.054
A_0	[(eV)$^{1.5}$]	28.1	E_1	[eV]	0.51
Γ_0	[eV]	0.33	E_2	[eV]	1.22
α_0	[eV]	0.11			
d	[nm]	318			

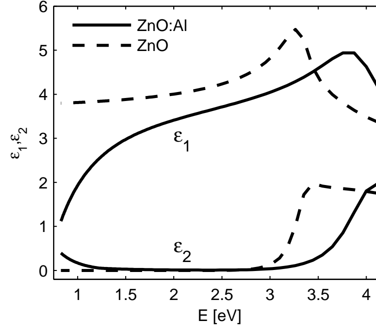

Figure 2.17: Real part ε_1 and imaginary part ε_2 of the dielectric function of RF-sputtered ZnO:Al obtained by fitting of the dispersion in Eq. 2.24 to measurement data of Fig. 2.16. The dielectric function determined for ZnO is included for reference.

2.4 Modelling of generation in Cu(In,Ga)Se_2 devices – influence of CIGS thickness and back contact

With the optical properties of all layers in the solar cell structure at hand, the optical model can be used to deliver answers to questions like: How much is the generation current J_{gen} decreased when the absorber thickness is decreased? How much is there to gain with an optically improved back contact?

The accuracy of the answers will depend not only on the accuracy of the optical properties used for the layers, but also on the applicability of the specular model. We have found that the specular model can reproduce the main features in the optical response of complete devices, for example the characteristic interference fringes caused by the window layers in QE spectra. It fails, however, in that:

- The amplitude of the interference fringes in the total reflectance have higher amplitude than in measurement spectra.
- The predicted interference in QE spectra for wavelengths where the absorber is partly transparent is more pronounced than in measurement spectra.

Both effects can be explained by light scattering caused by the surface roughness of the CIGS layer; lower-than-modelled reflectance at the Mo back contact could contributed to the second observation. For ZnO:Al/ZnO/CdS/glass samples, the agreement, including amplitude of interference is very good. For the integrated generation current, too high amplitude of interference fringes will only have a marginal effect, since positive and negative errors approximately cancel.

2.4.1 Estimation of absorber absorptance as a function of absorber thickness using measured R and T spectra.

In Paper III, the influence of varying absorber thickness d_a in the solar cell performance was investigated. As d_a is decreased from the standard thickness of 1.8 μm down to below 0.2 μm, the short circuit current of the solar cell decreases, as shown by Fig. 2.18.

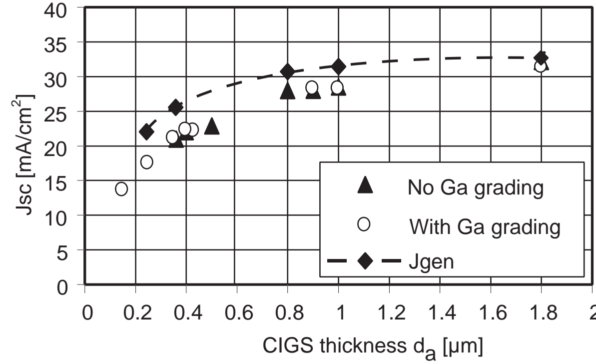

Figure 2.18: Short circuit current J_{sc} determined from QE measurements as a function of CIGS absorber thickness d_a, for absorbers with and without Ga grading. The dashed line gives the current generated in the CIGS layer, calculated from the absorber absorptance determined with the method discussed in this section.

It is of interest to quantify to which extent the decrease in short circuit current is due to optical losses, i.e. due to decreased generation of electron-hole pair in the device. This was done in Paper III by calculating the decrease in generation current J_{gen} from Eq. 2.8, using an approximation for absorber absorptance $A_a(\lambda)$ that will be discussed in this section. The result is indicated by the dashed line in Fig. 2.18. As can be seen, the experimentally obtained short circuit current decreases more rapidly than the generation current with decreasing thickness. The reason for the additional decrease is increased recombination leading to a degradation of the collection function $f_c(x)$, which will discussed in section 3.7.

Since the optical properties of all layers were not available when the study of Paper III was carried out, an alternative method was used to determine $A_a(\lambda)$. With the alternative method, $A_a^d(\lambda)$, where the superscript d here is added to signify absorber absorptance in the *device* structure, is estimated from measured reflectance for the complete device, and from measured reflectance and transmittance of CIGS/glass and window/glass structures, see Fig. 2.19. The desired quantity $A_a^d(\lambda)$ is not directly measurable, but can be related to the absorber absorptance $A_a^g(\lambda)$, which is readily calculated from

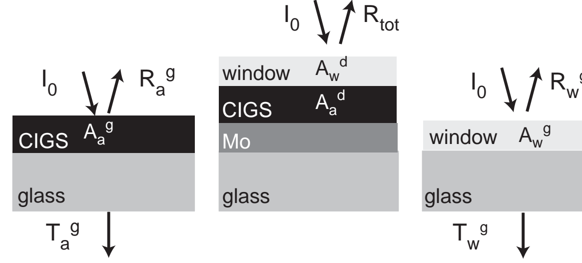

Figure 2.19: Samples and measurements used for estimating the absorptance in the absorber layer with the method used in Paper III. $A_a^d(\lambda)$ is the desired CIGS absorber absorptance of the complete device structure in the middle, A_w^d is the absorptance of the ZnO:Al/ZnO/CdS window layers in the device, and R_{tot} is the measured total reflectance of the device. R_a^g, T_a^g, and A_a^g denote the reflectance, transmittance and absorber absorptance for the absorber/glass substrate structure to the left, and R_w^g, T_w^g, and A_w^g are the corresponding quantities for the window/glass substrate structure to the right.

measurements of reflectance and transmittance for CIGS/glass according to

$$A_a^g(\lambda) = 1 - T_a^g(\lambda) - R_a^g(\lambda), \tag{2.27}$$

where it has been used that absorption in the glass substrate can be neglected.

It is then assumed that the *internal absorptance* for the CIGS layer on glass and and in the device are equal in the two cases. The internal absorptance is here defined for the CIGS/glass structure as

$$A'^g_a(\lambda) = \frac{A_a^g(\lambda)}{1 - R_a^g(\lambda)} \tag{2.28}$$

, and for the complete device as

$$A'^d_a(\lambda) = \frac{A_a^d(\lambda)}{1 - R_{tot}(\lambda) - A_w^d(\lambda)}. \tag{2.29}$$

Here, $R_{tot}(\lambda)$ is the total device reflectance and A_w^d is the absorptance of the window layers in the device. The approximation of equal internal absorptance is accurate if

(i) The optical properties of the CIGS absorber are the same when deposited on glass as when deposited on Mo.

(ii) The effect of different reflection of light at CIGS/glass and CIGS/Mo interfaces can be neglected.

By making the additional approximation that

(iii) The window absorptance in the device, $A_w^d(\lambda)$, is equal to the window absorptance obtained on a glass substrate, $A_w^g(\lambda)$,

the absorber absorptance in the device can be calculated from quantities directly obtained from measurements:

$$A_a^d(\lambda) = A_a^g(\lambda)\frac{1 - R_{tot}(\lambda) - A_w^g(\lambda)}{1 - R_a^g(\lambda)}, \tag{2.30}$$

with $A_a^g(\lambda)$ given by Eq. 2.27. The validity of condition (i) was checked by comparing the reflectance of two CIGS absorbers simultaneously deposited on glass and on Mo, respectively. After mechanical polishing of the samples, to suppress the influence of different surface roughness and surface overlayers, their reflectance was practically equal, as shown by Fig. 7 in Paper III. This indicates that their optical properties were similar. It cannot be excluded that a difference in optical properties exists for thinner absorbers, since the difference in substrate temperature caused by different emittance of glass substrates with and without Mo layer has a relatively larger impact in this case.

The validity of condition (ii) is more critical for thin than for thick absorbers, since for thin absorbers more light reaches the back surface of the absorber. The accuracy of the approximation can be checked by comparing the internal absorptance of Eq. 2.28 with that Eq. 2.29, when calculated with the specular optical model. This is done in the left graph of Fig. 2.20, for $d_a = 1.5$ μm (upper pair of curves) and $d_a = 0.3$ μm (lower pair of curves). It can be seen that internal absorptance calculated for the absorber in the device (solid lines, Eq. 2.29) is higher than the internal absorptance calculated for the absorber on a glass substrate (dashed lines, Eq. 2.28). This is because the reflectance is higher at the CIGS/Mo interface than at the CIGS/glass interface.

The validity of assumption (iii) can also be checked with the optical model. This is illustrated in the right graph of Fig. 2.20, where the solid line shows the calculated window absorptance in the device, $A_w^d(\lambda)$, for $d_a = 1.5$ μm, and the dashed line shows the window absorptance on glass substrate, $A_w^g(\lambda)$. It can be seen that the both curves agree well. Interference is more pronounced for the latter for short wavelengths, and more pronounced for the former for long wavelengths. This is because the contrast in refractive index is larger between CdS and glass than between CdS and CIGS for short wavelengths, and vice versa for long wavelengths. The interference pattern of the solid line depends on the absorber thickness, but the approximation $A_w^d(\lambda) = A_w^g(\lambda)$ is accurate independent of the absorber thickness. (Note that this conclusion might change when scattering is considered.)

The total error in the integrated generation current obtained with the simplified method, as evaluated from comparison with the specular optical model,

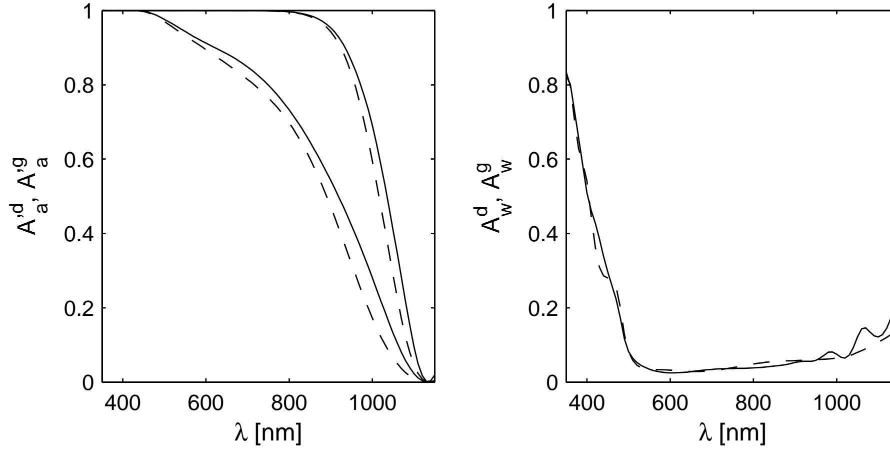

Figure 2.20: Left: Internal absorber absorptance $A'^{d}_{a}(\lambda)$ (Eq. 2.29) calculated for the complete device structure (solid lines) compared with internal absorber absorptance $A'^{g}_{a}(\lambda)$ (Eq. 2.28) calculated for a CIGS/glass sample (dashed lines). The higher and lower pair of absorptance curves are for absorber thickness $d_a = 1.5$ μm and $d_a = 0.3$ μm, respectively. Right: Window absorptance $A^{d}_{w}(\lambda)$ calculated for the ZnO:Al/ZnO/CdS layers in the device, i.e., on CIGS/Mo substrate (solid line) for $d_a = 1.5$ μm, compared with window absorptance $A^{g}_{w}(\lambda)$ calculated for ZnO:Al/ZnO/CdS on glass substrate (dashed line).

is only about 1 % at $d_a = 1.5$ μm, and about 5 % at $d_a = 0.4$ μm. In terms of current density, this corresponds to about 1 mA/cm^2 at $d_a = 0.4$ μm, which is considerably less than the decrease in J_{gen} with respect to cells with thicker absorbers, and also less than the difference between modelled J_{gen} and measured short circuit current. The latter implies that the method can be used to discriminate between optical losses and additional collection losses.

At last, it can be noted that a big advantage of this method is that no optical model is needed for the estimation of $A_a(\lambda)$. A disadvantage is that control samples with CIGS on glass must be fabricated and characterized for all thicknesses, but, on the other hand, that means that differences in optical properties between absorbers caused by different deposition conditions are automatically accounted for. The method has also the additional advantage that the effect of light scattering is to some extent included through the measured reflectances $R_{tot}(\lambda)$ and $R^{g}_{a}(\lambda)$. This feature can make the estimations of $A_a(\lambda)$ obtained with this method more accurate than the estimations obtained with a specular optical model.

2.4.2 How much is there to gain with light trapping?

It was concluded from Paper III that optical losses contribute significantly to decreased efficiency for CIGS solar cells with absorber thickness below 1 μm. In Paper IV, the possibility to maintain a high current generation in the absorber layer by the application of *light trapping* was investigated. The idea behind the concept of light trapping is to increase the average path that the light travels in the absorber layer beyond the absorber thickness, in order to increase the chances for light absorption. This effect can be obtained by, c.f. Fig. 2.21

1. Scattering of light such that it travels across the absorber at an oblique angle, and
2. High reflection of light at the absorber/back contact interface and at the absorber/window interface.

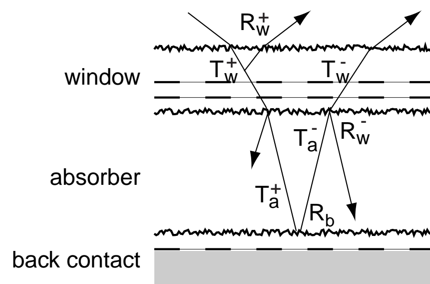

Figure 2.21: Device structure and notation for analysis of the potential for light trapping in $Cu(In,Ga)Se_2$ solar cells.

Scattering at the front and/or back surface of the absorber is preferable. Since the absorber has higher refractive index than the window layers, light scattered in these layers will be refracted towards the surface normal when it enters the absorber, which decreases the enhancement of the optical path induced by the scattering. Scattering in the bulk of the absorber is also possible, but scattering centres in the bulk are likely to degrade the electronic properties of the absorber.

High reflectance at the back contact, R_b, can be obtained by a large contrast in refractive index between the absorber and the back contact materials. If the back contact (or the upper layer in back contact comprising more than one layer) has a refractive index lower than the absorber, then for a high enough angle of incidence *total reflection* will be obtained. This effect must be relied upon to achieve high average reflectance R_w^- for light (with some angular distribution) incident on the absorber/window interface from the absorber side; a high contrast in the refractive index at this interface would decrease the transmittance T_w^+ for light from the medium of incidence (air) into the absorber.

T_w^+ should clearly be maximized in order to couple as much as possible of the incoming light into the absorber.

Optical modelling of layered structures in the case when the propagating light fluxes are partially coherent is a formidable task. However, not only the fully coherent (specular) case, but also the fully incoherent case are fairly straightforward to analyse, and those were the two limiting cases investigated in Paper IV. The fully incoherent case is of special interest, since it comprises the upper limit for light trapping by scattering. The actual limit depends on the assumptions made for the angular distribution of the scattered light; in Paper IV, the case of ideally Lambertian light scattering at both the front and back surface of the absorber was investigated, which means that the brightness (radiance) of the reflected light was assumed equal for all possible directions in the scattering hemisphere. The basis for the analysis in the incoherent case is the following expression for the absorber absorptance $A_a(\lambda)$

$$A_a = T_w^+ \frac{[(1 - T_a^+) + R_b T_a^+ (1 - T_a^-)]}{1 - R_w^- R_b T_a^+ T_a^-}, \tag{2.31}$$

which can be derived, e.g., by using matrix formalism for the optical response of layered structures. In Eq. 2.31, the quantities marked with $^+$ and $^-$ superscripts refer to inward and outward light fluxes, respectively, c.f. Fig. 2.21. The new quantities introduce are the T_a^+ and T_a^-, which denote the average absorber single pass transmittance for the total hemispherical inward and outward fluxes, respectively. Inspection of Eq. 2.31 reveals that

- The upper limit of A_a is reached when $T_a^+ = 0$ (all light absorbed on one passage). Then $A_a = T_w^+$, i.e. all light that is transmitted through the window is absorbed.
- The second term in the nominator represents absorption of the outward flux, which is increased by a high value of the reflectance R_b at the back contact.
- The denominator represents the enhancement by multiple reflections, and increases with both R_b and the window outward reflectance R_w^-.

The expression given for A_a in Eq. 2.31 is exact, provided that the quantities on the right hand side are calculated for the actual angular distribution of the total flux, possibly made up of multiple internal reflections. This holds independently of the structure, degree of coherency and absorption of the window layer and the back contact. In some simple cases, such as combinations of specular and ideally Lambertian scattering at the window and back interfaces, the angular distribution in the absorber is known, and it is then possible to express $T_a^{+/-}$, R_w^- and R_b analytically [85].

Eq. 2.31 highlights the importance of a high reflectance R_b at the back contact. Unfortunately, the standard Mo back contact performs bad in this respect. This is illustrated by Fig. 2.22, where R_b calculated for $CuIn_{0.6}Ga_{0.4}Se_2$ and

Ag, ZrN, TiN and Mo back contacts are shown. As mentioned in Paper IV, the flux of energy caused by interference between the incident and reflected waves present at the back contact interface [14] has to be taken into account in this calculation. It can be seen that for Mo, R_b varies in the range 20%-40% in the critical region $\lambda = 900$–1100 nm where CIGS absorption is relatively weak. This can be compared $R_b > 95\%$ obtained for Ag, which has a very low value of the real part n (~ 0.2) and a high value of the imaginary part k (~ 7) of the refractive index in this region, and therefore a high contrast in refractive index relative to CIGS. High R_b is also obtained with Al, another metal with strong free-electron character and therefore low n-values and high k-values. The problem with both Ag and Al is lack of chemical stability during absorber deposition. As alternatives, we have investigated TiN and ZrN. Both nitrides are known to be chemically stable, and have free-electron character which yields suitable optical properties. Although the levels of R_b obtained, 50%-60% for TiN and about 60% for ZrN in the region 900–1100 nm, are not at all as high as for Ag, there is significant improvement with respect to Mo.

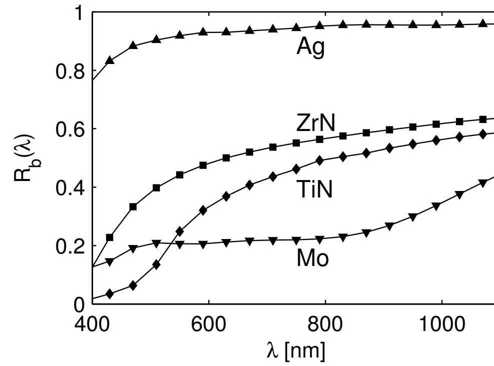

Figure 2.22: Reflectance $R_b(\lambda)$ at a $CuIn_{0.6}Ga_{0.4}Se_2$/back contact interface for Ag (Ref. [86]), ZrN, TiN (Ref. [87]) and Mo back contacts. $R_b(\lambda)$ is calculated from complex refractive indices of the materials using the Fresnel formulae and taking into account the interference flux of energy present at the CIGS side of the interface [14]. Optical properties of CIGS, Mo and ZrN are from this work.

To estimate the potential for light trapping and the influence of the back contact, the absorber absorptance given by Eq. 2.31 was calculated as a function of wavelength and of absorber thickness for the different back contacts. For each thickness, the total generation of electron-hole pairs in the absorber, $J_{gen} = A_a^{\mathrm{AM1.5}}$ was calculated using Eq. 2.8 and the standard AM 1.5 spectrum. The assumptions made in the calculation of the parameters $T_a^{+/-}$, R_w^- and R_b to be used in Eq. 2.31 are described in Paper IV. The generation current obtained with scattering model was also compared to the result of the specular model at normal incidence of the incoming light, see Fig. 4 of Paper IV.

Here, results from a similar calculation is shown in Fig. 2.23 for Ag, ZrN, Mo and "0%" (R_b = 0) back contacts. A difference with respect to Paper IV is that the wavelength range used for calculation of J_{gen} is extended to 1100 nm, in order to include the weak absorption tail of the optical data used; the absorption depth $1/\alpha$ increases from 2 μm at λ = 1000 nm, to 40 μm at λ = 1100 nm. (For an example of QE simulated with the same data, see Fig. 3.3 in the next chapter). The extention of the wavelength range increases the total available current in the standard spectrum (350–1100 nm) to 42.8 mA/cm^2. The upper limit for J_{gen} in this simulation, 35.1 mA/cm^2, is obtain by substracting the integrated inward reflectance losses (3.9 mA/cm^2) and inward window absorbtance losses (3.8 mA/cm^2), as indicated in the left graph of Fig. 2.23. These values depend on the thickness of the window layers, wich here were set to 350 nm, 70 nm, and 50 nm for ZnO:Al, ZnO and CdS, respectively.

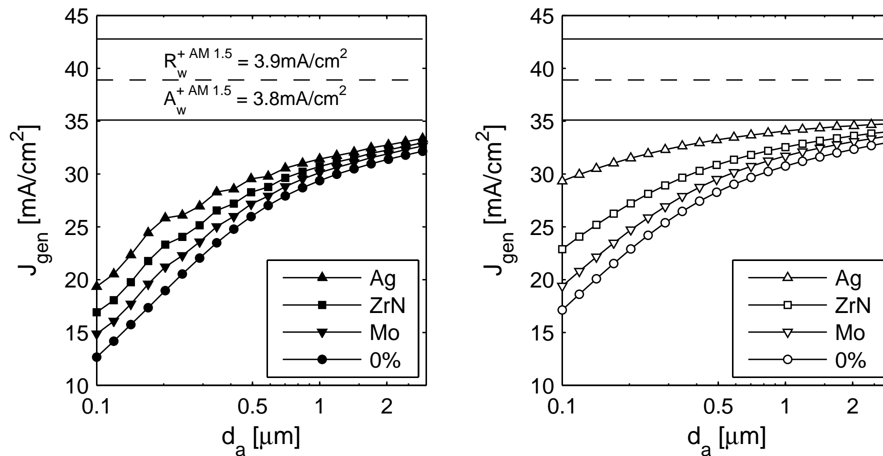

Figure 2.23: Simulated integrated AM 1.5 current J_{gen} generated in the CIGS layer for Ag, ZrN and Mo back reflectors as a function of absorber thickness at normal incidence. The left graph show results for the specular model, and right graph show results for the case of ideally Lambertian scattering at absorber back and front interfaces.

Due to the weak CIGS absorption for long wavelengths, the increased wavelength region has only a marginal effect on J_{gen} for thin absorbers and for low back reflectance. However, the light trapping effect becomes more pronounced. This is shown by the increased gain by light trapping for thicker absorbers shown in Fig. 2.24, relative to the results shown in Fig. 4b) of Paper IV. It can be noted that the calculated optical gain with a ZrN contact relative to a Mo contact at $d_a = 0.5$ μm is 1.1 mA/cm^2 in the specular model and 1.4 mA/cm^2 in the scattering model.

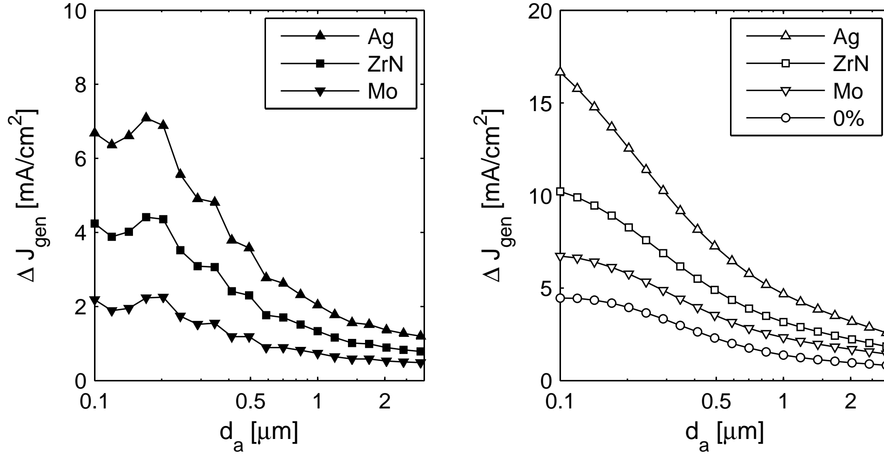

Figure 2.24: Current generation gain relative to the specular case with $R_b = 0$ for the simulations of Fig. 2.23.

2.4.3 Experimental confirmation of optical gain with TiN and ZrN back reflectors

The optical gain with the alternative back contacts TiN and ZrN was confirmed by improved QE for TiN in Paper IV and for ZrN in Paper V. QE spectra for the two cases are shown in Fig. 2.25. The integrated gain QE with respect to the reference cell with Mo back contact is 0.8 mA/cm^2 for the TiN cell with absorber thickness $d_a = 0.45$ μm, and 1.1 mA/cm^2 for the ZrN cell; in both cases this happens to be exactly the gain predicted by the simulations discussed above.

The exact agreement is encouraging but should not be taken too seriously. There are a number of expected model errors that seem to have cancelled. Light scattering is present in the samples, which should increase the gain by some 0.1 mA/cm^2. On the other hand, the QE is determined not only by the absorber absorptance but also by the collection efficiency. As shown in Paper V and further discussed in section 3.8, the collection efficiency can degrade with alternative back contacts. For the samples shown Fig. 2.25, CIGS absorbers with increasing Ga content towards the back contact (Ga grading) was used, which has been found to help maintaining high collection efficiency in cells with alternative back contact, see Paper V and Ref. [88]. But the Ga gradient also introduces a depth gradient in the optical properties of the absorber that was not taken into account in the simulations of the optical gain.

Nevertheless, even when considering the error sources in the simulations, the optical gain due to increased back reflectance with TiN and ZrN is evident from

1. Increased total device reflectance for $\lambda \geq 800$ nm, and

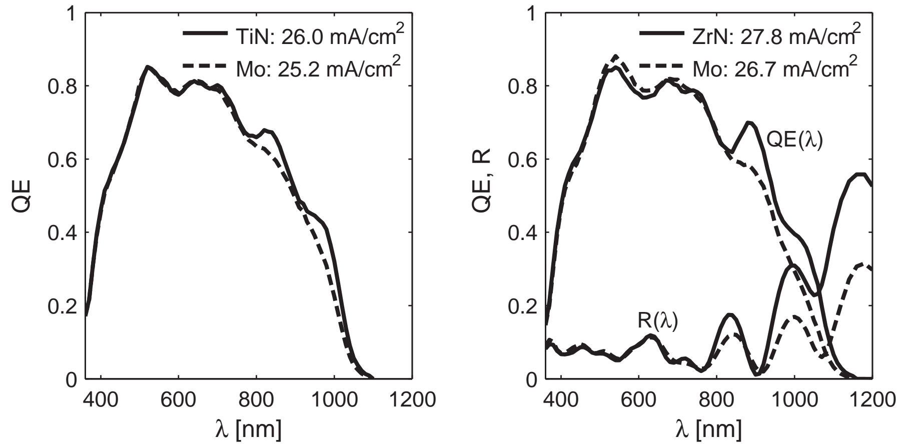

Figure 2.25: Optical gain with TiN (left, Paper IV) and ZrN (right, structure B of Paper V) back contacts. The observed increase in integrated QE is in good agreement with the predictions of the optical model. Note for the ZrN sample the increase in device reflectance $R(\lambda)$, which gives evidence of increased back contact reflectance R_b for CIGS/ZrN relative to CIGS/Mo.

2. Increased interference in the quantum efficiency for $\lambda \geq 800$ nm

An increase in device reflectance $R(\lambda)$ can be observed in Fig. 2.25 for ZrN. The largest contribution to $R(\lambda)$ is from the window/absorber subsystem, which is equal for reflector and reference samples. Since light reflected at the back contact is damped by at least two passages through the absorber before contributing to $R(\lambda)$, the increase in R_b is much larger than that observed in $R(\lambda)$.

The optical gain is larger for ZrN than for TiN. However, the optical gain with a plain ZrN contact is more than counter-balanced by degradation of the electrical properties. As discussed in Paper V and section 3.8, the degradation of the the electrical properties can be suppressed by a thin interfacial layer of $MoSe_2$. Since the device reflectance with a $MoSe_2$/ZrN back contact is still higher than with a Mo back contact (see Fig. 3 of Paper V), the electrically benign interfacial layer of $MoSe_2$ does not remove the optical gain.

3. Recombination

3.1 Basics of recombination in CIGS solar cells

It follows from the continuity equations for electrons and holes, that the total current output from a solar cell under illumination can be considered as a difference between a recombination current and a generation current:

$$J(V,\Phi) = J_{rec}(V,\Phi) - J_{gen}(\Phi). \tag{3.1}$$

The generation current J_{gen} was the topic of the last chapter, and the recombination current J_{rec} is the topic of this chapter. Whereas the generation current J_{gen} to an excellent approximation can be considered to depend only on the illumination (Φ), the recombination current J_{rec} is a function of both illumination and of the applied voltage (V). Under dark conditions ($\Phi = 0$), the recombination current reduces to what I will call the *diode current*, J_{diode}.[1] The total current output under illumination can then also be regarded as the difference between the diode current and a *photocurrent* J_L:

$$J(V,\Phi) = J_{diode}(V,\Phi) - J_L(V,\Phi), \tag{3.2}$$

where, in general, both the diode current and the photocurrent are functions of the applied voltage and of the illumination. This split of the total current is not arbitrary; the photocurrent will tend to zero as the illumination is decreased to zero, and the diode current will tend to zero as the voltage is decreased to zero, or, put differently, an incremental change $\delta\Phi$ of the illumination results in a change δJ_L of the total current, while an incremental change δV of the applied voltage will change the total current by δJ_{diode}.

The relation between the generation and recombination currents, on one hand, and the diode and light currents on the other hand, can be established by means of the collection function introduced in chapter 2. Repeating that

$$J_L(V,\Phi) = q \int_{cell} f_c(x,V,\Phi) G(x) dx \tag{3.3}$$

[1] Other names for this current are *bucking current* and *forward current*.

and introducing the photocurrent loss due to incomplete collection

$$J_L^{loss}(V,\Phi) = q \int\limits_{cell} (1 - f_c(x,V))G(x)dx \tag{3.4}$$

we get

$$\begin{aligned} J_{gen}(\Phi) &= J_L(V,\Phi) + J_L^{loss}(V,\Phi) & (3.5) \\ J_{rec}(V,\Phi) &= J_{diode}(V,\Phi) + J_L^{loss}(V,\Phi). & (3.6) \end{aligned}$$

The above equation makes clear that the total recombination current has two components: one component due to the diode current, and one due to the photocurrent loss.

Although the diode current and the photocurrent loss are caused by the same recombination mechanisms, they behave quite differently as a function of voltage and illumination, and are therefore modelled and analysed differently. The basic models for the diode current are discussed in section 3.1.4, and its characterisation by analysis of current-voltage characteristics measured as a function of temperature, $J(V)_{\mathrm{T}}$, is discussed in section 3.3. Modelling and characterisation of the photocurrent loss is discussed in section 3.2. Before getting there, I will briefly mention different *recombination mechanisms*, then discuss the dominant *recombination paths* in CIGS solar cells, which refers specific regions in the solar cell where recombination is high. I will also comment on the material defects that are decisive for recombination losses.

3.1.1 Recombination mechanisms

Recombination is the process which acts to bring the solar cell back to equilibrium by annihilation of excess electrons and holes. There are three main mechanisms by which an electron excited to the conduction band can return to the valence band [89]. In *radiative recombination*, the de-excitation involves the emission of a photon which carries away most of the excess energy. In *Auger recombination*, the excess energy is transferred to another electron or hole. The third mechanism is known as *Shockley-Read-Hall (SRH) recombination* [90, 91]. In this mechanism, the electron gives up its energy by emitting one or several phonons, which normally involves defects states, either in the volume of the material or at surfaces. This mechanism is dominant for CIGS solar cells – basically because of the large number of defects that exist in the CIGS material.

The SRH-recombination mediated by a discrete defect state (trap level) at an energy E_t within the bandgap can be described by

$$R = \frac{f_n f_p (np - n_0 p_0)}{f_n(n + n_t) + f_p(p + p_t)}. \tag{3.7}$$

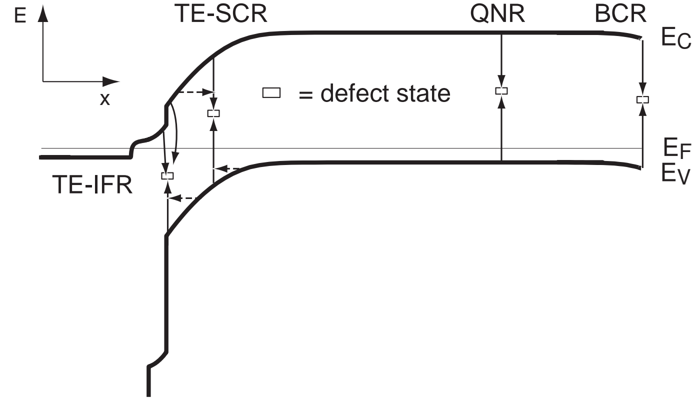

Figure 3.1: Schematic illustration of the dominant recombination paths in CIGS solar cells. The vertical arrows indicate how electrons from the bottom of the conduction band (E_C) can recombine with holes from the top of the valance band (E_V) via defects states within the bandgap. The horizontal arrows indicate how recombination can be enhanced by tunnelling in regions with high electric field. In the direction of the incoming light, the recombination paths are: tunnelling-enhanced recombination at the CdS/CIGS interface (TE-IFR), tunnelling-enhanced recombination in the space charge region (TE-SCR), recombination in the quasi-neutral region (QNR), and recombination at the back contact (BCR).

Here, $f_n = 1/\tau_n$ is a characteristic frequency for recombination of electrons, given by $v_{th}\sigma_n N_t$, where v_{th} is the thermal velocity of the electrons, σ_n is the cross section for trapping of electrons and N_t is the density of defects states; f_p is the corresponding recombination frequency for holes. n_t specifies the number of defects states occupied by electrons, and p_t specifies the number of defect states occupied by holes. The product $n_t p_t$ equals n_i^2. In general, more than one discrete level or a continuous distribution of levels add to the total recombination. It is straightforward to derive from Eq. 3.7 that for values of f_n and f_p of comparable magnitude, defect states close to midgap will give the largest contribution to the total recombination at a certain position. For a fix value of E_t and at an injection level such that $n, p >> n_t, p_t$, recombination will reach its maximum when $n \approx f_p/f_n \cdot p$, which is fulfilled at some point in the space charge region.

3.1.2 Dominant recombination paths

Recombination occurs at different rate in different regions of the solar cell. The dominant recombination paths in CIGS solar cells are indicated in Fig. 3.1. These are, in the direction of the incoming light:

TE-IFR Tunnelling-enhanced recombination at the CdS/CIGS interface.

TE-SCR Tunnelling-enhanced recombination in the space charge region.

QNR Recombination in the quasi-neutral region.

BCR Recombination at the back contact.

Normally, tunnelling enhancement is important only for interface recombination and for recombination in the space charge region, as indicated by the horizontal arrows in Fig. 3.1. However, tunnelling can be important also for recombination at the back contact, if there is a strong band bending close to this interface. In addition, tunnelling can contribute to recombination at grain boundaries, even in the formally quasi-neutral region.

Recombination in the buffer and window layers is not included in the list. Under dark conditions, these recombination paths can clearly be neglected because of the wider bandgap E_g of these layers; SRH-recombination increases, proportionally in quasi-neutral regions and with an exponent between 0.5 and 1 in the space charge region, with the excess excess np product given by

$$n_i^2(\exp[qV/kT]-1) \approx n_i^2 \exp[qV/kT] \propto \exp[(qV-E_g)/kT], \qquad (3.8)$$

where V is the applied voltage. Under illumination, generation can make the excess np product increase to significantly more than $n_i^2 \exp[qV/kT]$. The result of generation and recombination in the window and buffer layers under illumination then adds a (possibly voltage-dependent) contribution to the photocurrent.

Recombination at grain boundaries was also not explicitly included in the list above. In a one-dimensional model, this recombination path can be treated approximatively by assigning effective values, which take into account the influence of grain boundaries, to the material parameters entering the diode models.

3.1.3 Material aspects

The device performance is largely influenced by material defects, which control doping levels and provide recombination centres.

Defects in the Cu(In,Ga)Se_2 absorber

The subject of defects in Cu(In,Ga)Se_2 is very complex. A large number of defects are native to the crystal structure, and yet more defects can be formed by the presence of additional elements such as Na, Cd and O. The subject has been approached in two ways: (i) by theoretical calculations of defect energies using density functional theory, and (ii) by experimental observation of defects using capacitance methods such as DLTS, R-DLTS, and admittance spectroscopy.

Most of the theoretical work has been done by Zunger and co-workers. Defects in $CuInSe_2$ were treated in [92], the effect of adding Ga in [93] and the effect of adding Na in [94]. One important conclusion from this work is that the CIGS absorbers are heavily compensated, and that they are difficult to dope with extrinsic materials, since the formation of compensating defects becomes more favourable as the Fermi level shifts. In device quality material the net p-doping is a result of shallow V_{Cu}^{-} acceptor states, compensated by In_{Cu} donors.

The experimental characterisation of defects is complicated by metastabilities [95] and by the contribution of tunnelling [96, 97] to their electrical response. As a basis for the discussion in this chapter, I will use the interpretation of defect spectra proposed by the group of M. Igalson in Warsaw. According to this interpretation, the admittance features denoted "N1" and "N2" in the literature are both due to $In_{Cu}^{0/+}$ and $In_{Cu}^{+/++}$ transitions [97–99]. As shown in Table 3.1, reproduced from their review article Ref. [98], the transitions energies obtained correspond very well with theoretical data.

Table 3.1: *Electronic defects derived from capacitance spectra and suggested level assignments by the group of Dr M. Igalson. The table is reproduced from [98]. For the transition* $V_{Se}^{0/2+}$ *Ref. [94] states* E_V*+0.1 eV in the un-relaxed lattice and* E_C*-0.1 eV after lattice relaxion. More recent calculations in Ref. [100] state that the level before relaxation is within the valence band and at* E_V*+0.1 eV after relaxation.*

Type	$E_C - E_T$ [eV]	σ_p [cm^2]	σ_n [cm^2]	Assignment	Theory [92]
donor	0.19		$6 \cdot 10^{-17}$	$(In_{Cu}^{0/+} + V_{Cu})^{+}$	E_C-0.20 eV
donor	0.26		$4 \cdot 10^{-16}$	$In_{Cu}^{0/+}$	E_C-0.26 eV
donor	0.34		$4 \cdot 10^{-15}$	$In_{Cu}^{+/++}$	E_C-0.34 eV
donor	0.47	$< 1 \cdot 10^{-18}$	$5 \cdot 10^{-16}$	O_{Se} ?	
donor	> 0.6	$5 \cdot 10^{-14}$	$> 5 \cdot 10^{-14}$	$V_{Se}^{0/2+}$	

Grain boundaries

Since defects tend to accumulate at grain boundaries, one would expect that they enhance recombination and decrease performance. This is also the reason why solar cells made from polycrystalline silicon have lower efficiency than their mono-crystalline counterparts. In CIGS, however, grain boundaries do not seem to degrade performance significantly. On the contrary, better solar cell performance is obtained with polycrystalline than with single-crystalline material. Improved performance relative to single crystals can be understood if defects segregate to the grain boundary, making the defect density in the grain interior lower than in the single crystals, and the defects at the grain boundaries are left electrically inactive. The passivation of the grain boundaries could be either thanks to repulsive barriers for one or both carriers types,

or thanks to passivation by additional elements such as Na.

The role of grain boundaries in CIGS absorbers has recently gained more attention, both experimentally, see e.g. Refs. [101–103], and theoretically. Calculations by Persson and Zunger [104] suggest that a *charge-neutral* hole barrier, without detrimental band bending in the conduction band, can arise from the Cu deficiency of the grain surface that is required to form a stable polar surface. Such a grain boundary can be constructed by the neutral defects $(2V_{Cu}^{-}+ In_{Cu}^{++})^0$ or $2Na_{Cu}^0$. On the other hand, two-dimensional simulations of grain boundary recombination by Taretto *et al.* [105] did not indicate that a hole barrier would have a big effect in maintaining high efficiency when the density of grain boundary defects is increased.

Interface defects and pinning of the Fermi level

Defects at the back contact and above all at the CdS buffer/CIGS absorber interface are also important for recombination. Part of the interface defects arise from dangling bonds caused by the lattice mismatch between the materials on either side of the heterointerface. The density of interface states is therefore in general lower at heterointerfaces than between materials with similar lattice constants.

An increased density of interface states is not necessarily bad for the solar cell performance. Positively charged interface defect states at the buffer/absorber interface can decrease the distance between the Fermi level and the conduction band at the interface, and thereby decrease interface recombination. If the density of interface states is high enough (some 10^{-13} cm^{-2}), these will fixate ("pin") the Fermi level at the interface. The pinning can be favourable or detrimental for device performance, depending on the energetic position of the defects in the gap [106].

3.1.4 Diode models for recombination in dark conditions

I will use the term *diode model* to refer to expressions for the voltage-dependence of the diode current resulting from a recombination path. The principle way to derive a diode model for a recombination path is to integrate the voltage-dependent recombination of all contributing defect states over the energy within the bandgap over the region defining the path. The standard diode models are given here for easy reference in the following sections. Specifically, the ideality factor and the activation energy of the saturation current will be referred to. As pointed out by Rau and Schock [6, 107], the dominant diode currents about to be developed can all be written on the form

$$J_{diode}(V) = J_0(T)(e^{qV/AkT} - 1) = J_{00}e^{(-E_a/AkT)}(e^{qV/AkT} - 1), \qquad (3.9)$$

where A is the ideality factor, J_0 is the diode saturation current, E_a defines an activation energy, and J_{00} is a pre-factor which should be only weakly dependent on voltage and temperature. Defining the activation energy in this way, with the ideality factor in the denominator, is useful because it yields an activation energy relevant for the open circuit voltage. At open circuit voltage, we have $J_{diode} = J_L$, which can be used with Eq. 3.9 to obtain

$$qV_{oc} = E_a - A(T)kT \ln\left[\frac{J_{00}}{J_L}\right]. \tag{3.10}$$

This shows that the activation energy E_a defined by Eq. 3.9 sets the upper limit of the open circuit voltage, which is approached as the temperature decreases towards 0 K.

More in-depth information about these models can be found in various solar cell textbooks, such as Refs. [89, 108], on which I have based this section. Note that I will give the expressions under the assumption that the separation of the quasi-Fermi levels in dark conditions is constant and equal to qV throughout the space charge layer. As will be illustrated in section 3.2.3 this is not strictly true, but it is a reasonable approximation for high performance solar cells.

Recombination in the quasi-neutral region and at the back contact

In the quasi-neutral part of the CIGS layer and under low injection, we have $n << p \approx N_A$. The SRH-recombination of Eq. 3.7 reduces to $R = f_n\Delta n = \Delta n/\tau_n$, where τ_n is the minority carrier lifetime. This means that the total recombination is controlled by the excess concentration of minority electrons. For constant τ_n, the excess concentration can be obtained from an analytical solution of the continuity equation for electrons. The excess concentration at the edge of the depletion region, $n_0(e^{qV/kT} - 1)$, and the back contact recombination define the boundary conditions, giving the well-known result

$$\begin{aligned} J^{QNR} &= q\frac{D_e n_0}{L_e}\Theta_B(e^{qV/kT} - 1) = q\frac{D_e n_i^2}{L_e N_A}\Theta_B(e^{qV/kT} - 1) \\ &= q\frac{D_e\sqrt{N_C N_V}}{L_e N_A}\Theta_B e^{-E_g/kT}(e^{qV/kT} - 1) \end{aligned} \tag{3.11}$$

where the influence of the back contact recombination is contained in the parameter Θ_B, which depends on the normalized back contact recombination velocity, $s_b = S_b L_e/D_e$, and the ratio of the diffusion length to the width d_0 of the neutral region, $l = L_e/d_0$, according to

$$\Theta_B = \frac{s_b \cosh(l^{-1}) + \sinh(l^{-1})}{\cosh(l^{-1}) + s_b \sinh(l^{-1})}. \tag{3.12}$$

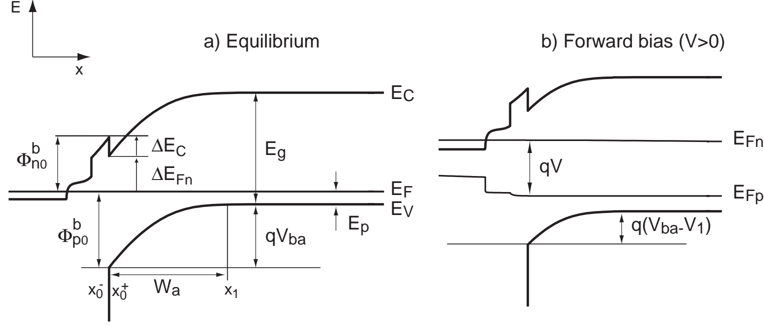

Figure 3.2: Definition of quantities introduced for describing space charge recombination and interface recombination.

Θ_B tends to 1 for small l, i.e. when the diffusion length is small compared to d_0. It can be noted that the diode current J^{QNR} has an ideality factor $A = 1$, and that the saturation current has an activation energy equal to E_g and is inversely proportional to the minority carrier diffusion length L_e.

Recombination in the space charge region

In the case of recombination in the space charge region, the concentration and recombination of both electrons and holes must be kept track of, which makes it much more complicated to derive an analytical expression for the diode current – numerically, it is similar to the case of QNR. The diode current can be approximately described by

$$\begin{aligned} J^{QNR} &= \frac{\pi}{2}\frac{kTD_e}{L_e^2}\frac{W_a}{(V_{ba}-V_1)}n_i(e^{qV/2kT}-1) \\ &= \frac{\pi}{2}\frac{kTD_e}{L_e^2}\frac{W_a(V)}{(V_{ba}-V_1)}\sqrt{N_C N_V}e^{-E_g/2kT}(e^{qV/2kT}-1) \end{aligned} \tag{3.13}$$

where W_a is the width of the space charge region in the absorber, V_{ba} is the band bending in the absorber at equilibrium and V_1 is the part of the total applied voltage V that is developed in the absorber, see Fig. 3.2.

In the above expression it has been assumed that $\tau_n = \tau_p$ and that the dominant contribution to the recombination is from defect states close to midgap. As can be seen seen, the ideality factor in this case becomes $A = 2$, and the activation energy of the saturation current as defined in Eq. 3.9 is again equal to E_g. The diode current is here inversely proportional to the square of the diffusion length. As the energetic position of the dominant recombination centres moves away from midgap, the ideality factor tends to one. The ideality factor is further modified by tunnelling enhancement. For CIGS, the following expression for the ideality factor has been proposed for tunnelling-enhanced

space charge recombination:

$$\frac{1}{A} = \frac{1}{2}\left(1 + \frac{kT^*}{kT} - \frac{E_{00}^2}{3(kT)^2}\right). \tag{3.14}$$

The second term in the brackets originates from a model due to Walter *et al.* [109] of recombination via a distribution of trap states that decreases exponentially from the band edge(s) with a characteristic energy kT^*. The third term, derived by Rau in Ref. [110], accounts for the influence of tunnelling, which becomes increasingly important with decreasing temperature. The characteristic energy for tunnelling, E_{00}, is a material parameter proportional to $\sqrt{N_A/m^*}$, where m^* is the effective mass of the tunnelling charge carrier. The expression Eq. 3.14 has been found to agree well with experimentally obtained ideality factors for different CIGS cells with varying properties. However, basing on the Warsaw interpretation of defect spectra referred to above, one would expect that the dominant recombination occurs through discrete states rather the through a continuous distribution of states decreasing from the band edges.

Interface recombination

For the interface recombination path, the current caused by the recombination of holes with concentration p_a at the absorber side of the buffer/absorber interface is given by the sum of the recombination with electrons on the absorber side having concentration n_a,

$$J^{IFR1} = q\frac{S_n S_p(n_a p_a - n_{a0} p_{a0})}{S_n(n_a + n_t) + s_p(p_a + p_t)}, \tag{3.15}$$

and the recombination with electrons at the buffer side having concentration n_b,

$$J^{IFR2} = q\frac{S_n S_p(n_b p_a - n_{b0} p_{a0})}{S_n(n_b + n_t) + S_p(p_a + p_t)}. \tag{3.16}$$

In these equations, the S parameters are recombination velocities (given in cm/s) corresponding to the recombination frequencies f (measured in 1/s) of Eq. 3.7.

Which of the two terms will dominate depends on the conduction-band offset ΔE_C defined in Fig. 3.2. The effective bandgap for the second process is given by $G = E_g + \Delta E_C$. Thus, for a negative ΔE_C (conduction band minimum of the buffer is at lower energy than the conduction band minimum of the absorber) the latter term will tend to dominate. In the following I will not differentiate between these two contributions, since they can be discussed on the same basis by replacing E_g for G.

It is instructive to consider some special cases. First, if the Fermi level at the interface is close to the conduction band, then the recombination is limited by the concentration p_a of holes available at the absorber side of the interface. This case is commonly referred to by the phrase *type inversion*, since the surface of the absorber is n-type, i.e., type inverted relative to the p-type bulk. Neglecting tunnelling contribution, the current then takes the form

$$\begin{aligned} J^{IFR}(V) &= qS_p(p_a - p_{a0}) = qS_p p_0 e^{-qV_{ba}/kT}(e^{qV_1/kT} - 1) \\ &= qS_p N_V e^{-\Phi^b_{p0}/kT}(e^{qV_1/kT} - 1) \\ &= qS_p N_V e^{-\Phi^b_{p0}/kT}(e^{qV/AkT} - 1) \end{aligned} \quad (3.17)$$

where S_p is the interface recombination velocity, Φ^b_{p0} is the distance between the absorber valence band and the Fermi level at the interface in equilibrium, and $V_1 = V/A$ is the part of the total junction voltage V that is developed in the absorber, and A is identical with the ideality factor. The activation energy defined according to Eq. 3.9 becomes $E_a = A\Phi^b_{p0}$. Note from Fig. 3.2 that the hole barrier for interface recombination is given by

$$\Phi^b_{p0} = E_g - \Delta E_{F_n} = qV_{ba} + E_p, \quad (3.18)$$

where ΔE_{F_n} is the energy difference between conduction band of the absorber and the Fermi level at the buffer/absorber interface in equilibrium, and E_p is the separation between the Fermi level and valence band in the quasi-neutral part of the absorber. Clearly we have $\Phi^b_{p0} \leq E_g$. The relation also shows clearly that the barrier for interface recombination decreases with increasing ΔE_{F_n} and decreasing absorber band bending V_{ba}.

If the charge balance between the positive and negative side of the junction does not change with the applied voltage or illumination, then the ideality factor A is constant for this case. With contribution from tunnelling of holes to the interface, the ideality factor is modified to [111]

$$A = \frac{E_{00}}{kT} \coth\left(\frac{E_{00}}{kT}\right). \quad (3.19)$$

A second case of relevance for the discussion is when the Fermi level at the interface is close to midgap, i.e., when $\Delta E_{F_n} \approx \Phi^b_{p0} \approx E_g/2$. In this case, the concentration of electrons and holes are comparable and Eq. 3.15 can be written (assuming $S_n = S_p$) [89]

$$J^{IFR}(V) = qSn_i\left(\frac{e^{V/kT}}{e^{V_1/kT} + e^{V_2/kT}} - 1\right), \quad (3.20)$$

where $V_2 = V - V_1$ is the part of the voltage developed on the n-side. If the

voltage is developed entirely in the absorber (or entirely on the n-side), then this current will be constant for $V > kT$, which corresponds to an infinite ideality factor. In the more common situation when $V_1 \approx V_2 \approx V/2$, we get

$$\begin{aligned} J^{IFR}(V) &= qSn_i \left(e^{V/2kT} - 1\right) \\ &= qS\sqrt{N_C N_V} e^{-E_g/2kT} \left(e^{V/2kT} - 1\right), \end{aligned} \tag{3.21}$$

such that the ideality factor becomes $A = 2$ and the activation energy equals E_g (or G). Comparison of the current given in Eq. 3.17 for type inversion and the current of Eq. 3.20 for second case of $\Delta E_{F_n} \approx E_g/2$, shows that, neglecting tunnelling

1. The saturation current J_0 is larger in the second case, since the intrinsic carrier concentration n_i is larger than the hole concentration at the interface p_a in the first case.
2. The ideality factor in the second case ($A \in [2, \infty)$) tends to be larger than in the first case of type inversion, where $A \approx 1 < 2$ is valid in the (normal) situation when most of the applied voltage is developed in the absorber.

I will refer to these qualitative features when relating increased interface recombination to an increase of ΔE_{F_n}.

3.2 Modelling of the photocurrent loss

The contributions of different recombination paths to the total diode current can be calculated from the diode models. Their relative magnitude is different from the relative importance of the recombination paths for the photocurrent loss, the other component of the recombination current. For example, the diode current in a CIGS solar cell is normally dominated by the interface path and the space charge layer path, but recombination in the quasi-neutral region can, for the same cell, give the largest contribution to the photocurrent loss. However, there is a profound link between the collection function used to calculate the photocurrent loss and the diode currents, which is given by the so-called reciprocity theorem.

3.2.1 The reciprocity theorem for carrier collection

The reciprocity theorem for carrier collection states that the collection function (or collection probability) for minority carriers in the quasi-neutral region of a solar cell under illumination at short circuit is given by

$$f_c(x) = \frac{u_n(x)}{u_{nJ}}, \tag{3.22}$$

where $u_n \equiv \Delta n/n_0$ is the normalized excess minority (here electron) carrier concentration at forward bias, and $u_{nJ} = (e^{qV_J/kT} - 1)$ is the corresponding normalized excess carrier at the edge of the depletion region, controlled by the junction voltage V_J. In this way, the reciprocity theorem relates the collection function, relevant for the photocurrent of the cell *under illumination*, to the excess carrier concentrations resulting from the diode current *in dark operation*. This relation is not only theoretically interesting, but has also practical use as it provides a convenient way to calculate the collection function numerically, an aspect important not least for calculations in two [112] and three dimensions, where the relation holds equally well.

The reciprocity theorem was first derived for *pn*-junction solar cells by Donolato [113], who applied it to EBIC (electron beam induced current) experiments. The proof has then been generalized by Green [114], Markvart [115] and others to cover the situation where the minority carrier lifetime, the diffusion constant and the equilibrium carrier concentration, i.e. the coefficients that enters the continuity equation describing minority carrier diffusion, all are allowed to vary with the spatial coordinate. The proof relies on the linearity and symmetry of the differential operator defining the continuity equation. It is therefore restricted to low injection conditions. The result has been explained physically as a consequence of the principle of detailed balance by Rau and Brendel [116], who also extended it to the case of discrete states. These authors further investigated the applicability to particles described by Fermi-Dirac statistics (instead of Boltzmann statistics), for which Eq. 3.22 can be written

$$f_c(x) = \frac{E_{F_n}(x)}{qV}, \tag{3.23}$$

where E_{F_n} is the quasi-Fermi level measured from the Fermi level in equilibrium. In this latter case, they found that it was applicable only for small deviations from equilibrium.

3.2.2 A generalization of the reciprocity theorem to include both electrons and holes in the space charge region

The are two limitations of the reciprocity theorem that restrict its applicability to CIGS solar cells: Firstly, it does not hold within the depletion region, where substantial collection losses can occur, for example due to interface recombination. Secondly, the boundary condition for the collection in the quasi-neutral region is not well-defined, i.e. the collection probability at the edge of the depletion region is not necessarily equal to 1.

Now, it turns out that it is possible to generalize the reciprocity theorem in order to take into account both electrons and holes. This is done by consider-

ing the normalized excess np-product,

$$u_{np}(x) = \frac{np(x) - n_0 p_0(x)}{n_0 p_0(x)} = e^{\frac{E_{F_n}(x) - E_{F_p}(x)}{kT}} - 1, \tag{3.24}$$

which is a fundamental driving force for recombination that reduces to the excess minority concentration u_n (or u_p) in the quasi-neutral regions. Since the differential equation controlling u_{np}, corresponding to the continuity equation for minority carriers, is non-linear, the machinery behind the reciprocity theorem cannot be applied directly. However, by linearising the equation for a small deviation from equilibrium, the linearity and symmetry of the linearized differential operator can be used just in the case of minority carriers in neutral regions to obtain a generalized reciprocity theorem valid throughout the solar cell close to equilibrium [117]. The result is

$$f_c(x) = \frac{u_{np}(x)}{e^{qV/kT} - 1} = \frac{E_{F_n}(x) - E_{F_p}(x)}{qV}, \tag{3.25}$$

where the second equality follows from the Eq. 3.24 close to equilibrium, i.e. for small values of the applied voltage V.

It should be emphasized that this result is valid only close to equilibrium, due to the non-linearity of the full equation. There are two slightly different reasons for the non-linearity: (i) changed potential distribution in the junction depending on the illumination- and voltage-dependent occupation of charged defect states, and (ii) recombination paths that are not linear in u_{np}. The latter is the case for all recombination paths with ideality factor different from 1. For example, for recombination in the space charge region with $A = 2$, we have $R \propto u_{np}^{1/A} = u_{np}^{0.5}$. On the other hand, since the recombination can be written $R(x) = R_0(x) u_{np}^{1/A}$, the form of Eq. 3.25 suggests that the total current at an arbitrary working point (V, Φ) can be written (formally including interface recombination in the integrals)

$$\begin{aligned} J(V,\Phi) = J_{rec} - J_{gen} &= q \int_{(p)}^{(n)} [R(x) - G(x)] dx \\ = J_{diode} - J_L &= q \int_{(p)}^{(n)} f_c(x) [R_0(x)(e^{qV/A(x)kT} - 1) - G(x)] dx, \end{aligned} \tag{3.26}$$

where the collection function $f_c(x)$, the pre-factor $R_0(x)$ and the local ideality factor $A(x)$ all are functions of voltage bias and illumination, and where $A(x)$

can be found from (c.f. Ref. [118])

$$\frac{1}{A(x)} = \frac{u_{np}(x)}{R(x)} \frac{dR(x)}{du_{np}(x)}. \tag{3.27}$$

However, this idea has not yet been investigated in detail.

3.2.3 Applications of the reciprocity theorem to collection in CIGS solar cells

In spite of the restriction to situations close to equilibrium, the generalized reciprocity theorem of Eq. 3.25 has an application for CIGS solar cells, since it can be used to calculate a collection function pertinent for interpretation of QE spectra measured at zero voltage bias and at low light intensity. In practice, this can be done by calculating first $n_0p_0(x)$ and then $np(x)$ at small forward bias using a device simulator such as SCAPS[12, 13], and then plug these into Eq. 3.24 and Eq. 3.25. The validity of this approach has been tested numerically by comparing QE spectra calculated in SCAPS with QE spectra calculated from Eq. 2.12 with the collection function of Eq. 3.25 for the same generation profile $g(x,\lambda)$.

Here, this method has been used to illustrate the effect of varying material parameters on the collection function and the quantum efficiency. The QE spectra were calculated with $g(x,\lambda)$ obtained from the optical model of chapter 2. The thickness of the layers was set to 350 nm, 70 nm, 50 nm and 1.5 μm for ZnO:Al, ZnO, CdS and CIGS, respectively.

Collection function for varying diffusion lengths

In Fig. 3.3 the effect of varying diffusion lengths for electrons and holes in the CIGS absorber is illustrated. The diffusion lengths were varied by varying the concentration of midgap recombination centres in the SCAPS simulation. Equal capture cross sections were assumed for electrons and holes, resulting in equal life times, but since the electron mobility μ_e was assumed four times higher (100 cm^2/Vs) than the hole mobility (μ_h= 25 cm^2/Vs), the resulting diffusion length L_e for electrons was double the diffusion length L_h for holes. The calculation was done for the case of an inverted surface, which makes the collection of photogenerated electrons less sensitive to interface recombination.

When the diffusion length is long, or, more precisely, when the drift length L_{drift} in the space charge region is much longer than the width of space charge region for both electrons and holes, collection in the space charge region is close to unity. The drift length depends on the square of the diffusion length, $L_{drift} = v_{drift}\tau = \frac{q}{kT}\xi L_{diff}^2$, where ξ is the electric field. Note that the reciprocity theorem for collection of minority carriers, Eq. 3.22, always applies

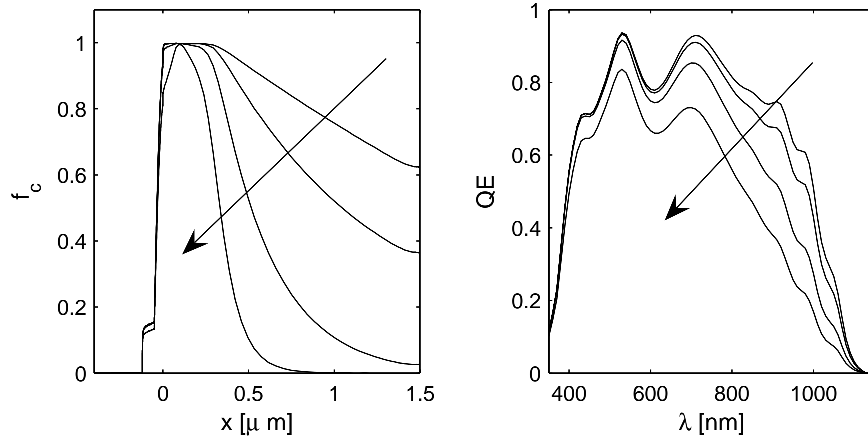

Figure 3.3: Collection function and quantum efficiency calculated for different values of the diffusion lengths of electrons (L_e) and holes (L_h) in the CIGS absorber. L_h was set to $L_e/2$, and L_e decreases in the direction of the arrow according to 3.3 μm, 1.0 μm, 0.33 μm, and 0.1 μm. Back contact recombination velocity was set to $S_b = 10^3$ cm/s, and doping levels were chosen such that the absorber was type inverted at the interface to the CdS buffer. Recombination velocities at the CdS/CIGS and ZnO/CdS interfaces were set to $S_{if1} = 10^5$ cm/s and $S_{if2} = 10^6$ cm/s, respectively.

in the quasi-neutral region, provided that the collection probability $f_c(x_1)$ at the edge of the depletion region (at $x = x_1$, c.f. Fig. 3.2), is used as a boundary condition. For constant material parameters it can be obtained analytically from the solution of the continuity equation for minority electrons,

$$f_c(x') = f_c(x_1)\left[\cosh(x'/L_e) - \Theta_B \sinh(x'/L_e)\right], \qquad (3.28)$$

where x' measures the distance from the edge of the depletion region, and Θ_B again is given by Eq. 3.12. When the diffusion length is long with respect to the width of the quasi-neutral region, the recombination velocity at the back contact becomes important; in Fig. 3.3 a $S_b = 10^3$ cm/s has been used. As the diffusion lengths are decreased, carrier collection decreases in the quasi-neutral region, but also in the space charge region. In the case of L_e = 0.1 μm, unity collection, i.e. a separation of the quasi-Fermi levels equal to qV, is maintained only in the middle of the space charge region where $n \approx p$. The decline from this point towards the CdS interface is caused by incomplete collection of (minority) holes, and the decline towards the back contact is caused by incomplete collection of (minority) electrons. When the diffusion lengths are further decreased, collection falls below unity also in the middle of the space charge region.

Collection function for varying interface recombination velocity

The next two figures, Fig. 3.4 and Fig. 3.5, illustrate the effect of varying interface recombination velocity. The result is quite different depending on the type inversion of the absorber. The case of Fig. 3.4 corresponds to an inverted absorber, i.e., the Fermi level at the interface is close to the conduction band of the absorber, which resulted from doping levels for the CIGS, CdS and ZnO layers of 10^{16} cm^{-3}, $5 \cdot 10^{16}$ cm^{-3}, and 10^{17} cm^{-3}, respectively, and $\Delta E_C = 0$ at the CdS/CIGS interface. Increasing interface recombination then has a significant impact only on carrier collection in the buffer layers. Since these layers are thin, drift and diffusion lengths should be comparable to or exceed the layers' thicknesses (in the simulations, L_h was set to 0.1 μm and 0.5 μm in the CdS and ZnO layers, respectively), and collection is therefore controlled by the interface recombination. For the upper curve of Fig. 3.4, the CdS/CIGS interface, S_{if1}, is set to a reasonably high value of 10^5 cm/s, and the interface recombination at the ZnO/CdS interface, S_{if2}, is set to zero. With these parameters, the calculated collection probability is high in both buffer layers, which results in a quantum efficiency for short wavelengths higher than what is experimentally observed. According to the optical model, the generation of electron-hole pairs in the ZnO layer is larger than in the CdS layer for $\lambda < 390$ nm. The experimentally observed low QE in this wavelength re-

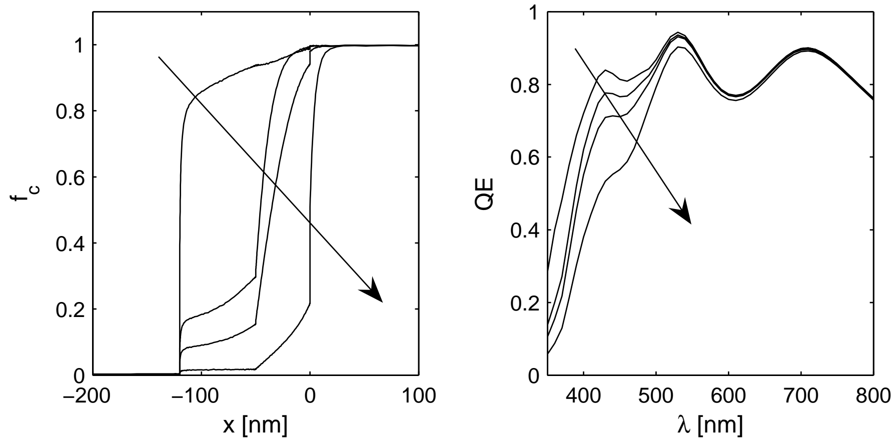

Figure 3.4: Collection function and quantum efficiency calculated for different interface recombination velocities at the CdS/CIGS interface (S_{if1}) and at ZnO/CdS interface (S_{if2}) for the case when the Fermi level at the interface is close to the conduction band (type inversion). For the curve with highest collection, $S_{if2} = 0$ cm/s and $S_{if1} = 10^5$ cm/s. For the other curves, $S_{if2} = 10^6$ cm/s and $S_{if1} = 10^3$ cm/s, 10^5 cm/s, and 10^6 cm/s, respectively, with increasing values in the direction of the arrow. $L_e = 2L_h$ in the absorber was set to 1.0 μm.

gion can be approached by assuming a high interface recombination velocity

at the ZnO/CdS interface. This was done for the three lower curves of Fig. 3.4, where S_{if2} was set to 10^6 cm/s. Note that the largest impact on the QE caused by this change for $\lambda > 400$ nm is due decreased collection in the CdS layer. This highlights the influence of the second interface on the current collection, an aspect that should be considered also in the analysis of short wavelength QE of cells with alternative buffer layers. Varying S_{if1} for a fix high value of S_{if2} affects the collection in the CdS buffer most. For the highest recombination velocity, collection in the top of the CIGS layer is also affected.

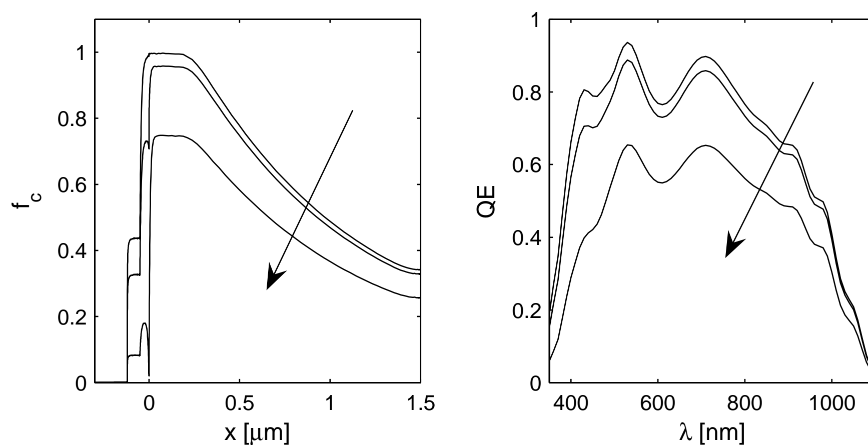

Figure 3.5: Collection function and quantum efficiency calculated for different interface recombination velocities at the CdS/CIGS interface (S_{if1}) for the case when the Fermi level at the interface is close to mid-gap. In the direction of the arrow, S_{if1} increases according to 10^3 cm/s, 10^5 cm/s, and 10^7 cm/s, respectively. S_{if2} was set to 10^6 cm/s, and $L_e = 2L_h$ in the absorber to 1.0 μm.

In the case of Fig. 3.5, the Fermi level at the interface is close to midgap, which resulted from doping levels for the CIGS CdS and ZnO layers all equal to 10^{16} cm^{-3}, and a positive conduction-band offset $\Delta E_C = +0.2$ eV between the CdS buffer and the absorber. Since in this case $n \approx p$ at the interface, increased interface recombination is important not only for the collection of holes but also for the collection of electrons. Thus, the level of the collection function is decreased throughout the CIGS absorber, since every photogenerated electron has to pass the interface before getting collected at the n-side contact.

Recombination analysis using QE **spectra**

It is clear from the simulations above that the analysis of QE spectra combined with a model for the generation profile can provide information on the collection function and, thereby, the reason for incomplete carrier collection. QE measurements as a function of illumination and voltage bias can provide

additional information on how the collection function depends on the working point (V,Φ). In the appended papers and in the remaining of this chapter, the QE analysis is done only qualitatively, for example to distinguish between collection losses due to poor diffusion length affecting long wavelength QE (c.f. Fig. 3.3), and collection losses due to interface recombination for a non-inverted absorber affecting all wavelengths (c.f. Fig. 3.5).

Accurate knowledge of the generation profile also allows for a more quantitative analysis, in which Eq. 2.12 is inverted to yield $f_c(x)$ given $g(x,\lambda)$ and $\mathrm{QE}(\lambda)$. It is then preferable to work with the internal quantum efficiency, defined by

$$\mathrm{IQE}(\lambda) = \frac{\mathrm{QE}(\lambda)}{1 - R_{tot}(\lambda)} \tag{3.29}$$

to reduce errors introduced by errors in the optical model for the total reflectance R_{tot}. Because of the interference in CIGS solar cells, it is important to measure QE and R_{tot} at the same spot (to get same layer thicknesses) and with the same angle of incidence.

3.2.4 Combining diode currents and the photocurrent under illumination

The expressions given in section 3.1.4 for the diode currents resulting from the recombination paths as a function of applied voltage are valid on the condition that the quasi-Fermi levels, E_{F_n} and E_{F_p}, are separated by qV throughout the depletion region. If that holds, the total current is obtained by simply adding the individual contributions:

$$\begin{aligned} J(V,\Phi) = {} & J_0^{QNR}(e^{qV/kT} - 1) + J_0^{SCR}(e^{qV/A_{SCR}kT} - 1) \\ & + J_0^{IFR}(e^{qV/A_{IFR}kT} - 1) - J_L. \end{aligned} \tag{3.30}$$

But it follows from the results in section 3.2.3 that this condition is not necessarily true even under dark conditions. A more general situation is analysed, for instance, in chapter 5 of Ref. [89]. The result obtained in this reference, where interface recombination was considered but remaining recombination (and generation) was neglected in the space charge region, is kept on the form of Eq. 3.30 by the introduction of transport factors $0 < F < 1$

$$\begin{aligned} J(V,\Phi) &= F_{an}F_{in}F_{bn}\left[J_0^{QNR}(e^{qV/kT} - 1) - J_{L'}^{QNR}\right] \\ &= F_{in}F_{bn}\left[J_0^{IFR1}(e^{qV/A_{IFR1}kT} - 1)\right] \\ &= F_{bn}\left[J_0^{IFR2}(e^{qV/A_{IFR2}kT} - 1)\right]. \end{aligned} \tag{3.31}$$

Here, $J_{L'}^{QNR}$ is the photocurrent diffusing out of the neutral region, i.e. the contribution to the total photocurrent that would have been obtained with unity collection $f_c(x_1) = 1$ at the edge of the depletion region at $x = x_1$ (c.f. Fig. 3.2). The transport factor F_{an}, where the index a stands for "absorber" and the index n signifies n-type carrier, is a measure of how likely it is that an electron at $x = x_1$ will be swept across the depletion region to the interface instead of diffusing away from the junction, given by

$$F_{an} = \frac{v_{drift}}{v_{drift} + v_{diff}}, \tag{3.32}$$

where v_{drift} is an average drift velocity and $v_{diff} = D_e/L_e\theta_B$ is the diffusion velocity (including the effect of the back contact); the transport factor F_{bn} is correspondingly defined for electrons in the conduction band of the buffer. Similarly, the transport factor F_{in} is a measure of how likely an it is that an electron at the interface ($x = x_0^+$, see Fig. 3.2) will be emitted to the other side of the interface ($x = x_0^-$), relative to its tendency to recombine at the interface or to diffuse back. We wish these transport factors to be as close as possible to unity, since that maximizes the photocurrent and the power output. The transport factors are useful for interpreting collection losses, to which they are clearly related; the collection probability for electrons at $x = x_1$ can be identified with the product $f_c(x_1) = F_{an}F_{in}F_{bn}$. Examples will be given below, where a combination of a positive conduction band off-set and small band bending in the absorber decreases the rate of thermionic emission so that $F_{in} < 1$. This decreases collection of all electrons generated on the absorber side of the junction, as also shown by the simulations illustrated in Fig. 3.5.

To sum up, the photo-current in CIGS solar cells can be split into contributions from the quasi-neutral region in the absorber (J_L^{QNR}), from the space charge region (J_L^{SCR}) and from the buffer layers (J_L^{buffer}) according to

$$\begin{aligned} J_L(V,\Phi) &= J_L^{QNR} + J_L^{SCR} + J_L^{buffer} \\ &= f_c(x_1)J_{L'}^{QNR} + \overline{f}_c^{SCR} J_{L'}^{SCR} + f_c(x_0^-)J_{L'}^{buffer} \end{aligned} \tag{3.33}$$

where $J_{L'}^{QNR}$ ($J_{L'}^{buffer}$) is the photo-current that would have been obtained from the quasi-neutral region (the buffer layers) if the collection probability at the edge of the the depletion region (at the buffer side of the interface) now equal to $f_c(x_1)$ ($f_c(x_1^-)$) were equal to unity, and $J_{L'}^{SCR} = J_{gen}^{SCR}$ is the photo-current that would have been obtained from the space charge region if the collection probability in this region, now having an average value of $\overline{f}_c^{SCR}$, were equal to unity. The comparison of Eq. 3.31 and Eq. 3.26 proposed earlier further

suggests that the total current under illumination can be written on the form

$$
\begin{aligned}
J(V,\Phi) = f(x_1)\left[J_0^{QNR}(e^{qV/kT}-1) - J_{L'}^{QNR}\right] \\
+ f_c(x_{max})\cdot J_0^{SCR}(e^{qV/A_{SCR}kT}-1) - \overline{f}_c^{SCR}\cdot J_{gen}^{SCR} \\
+ f_c(x_0^+)\left[J_0^{IFR1}(e^{qV/A_{IFR1}kT}-1)\right] \\
+ f_c(x_0^-)\left[J_0^{IFR2}(e^{qV/A_{IFR2}kT}-1) - J_{L'}^{buffer}\right]
\end{aligned}
\tag{3.34}
$$

where $f_c(x_{max})$ is the average collection probability in the region of maximum recombination in the space charge region. In the recombination analysis of the diode currents discussed in the next section, Eq. 3.30 rather than Eq. 3.34 will be used. This approach is acceptable when the voltage-dependence of the collection function is weak. The values of the collection function at $V = 0$ then enter as constant factors multiplying the saturation currents J_0.

3.3 Recombination analysis of the diode currents

Measurement of current-voltage characteristics at different temperatures, $J(V)_{\mathrm{T}}$, is the most widely used method for characterising diode currents in CIGS solar cells. The analysis aims at identifying the dominant recombination path from the temperature dependence of the corresponding diode saturation current and ideality factor.

3.3.1 Fitting of one-diode model parameters

To find the saturation current J_0 and the ideality factor A, these parameters have been fitted to measured $J(V)$ characteristics in dark and under illumination, as have the photo-current J_L, the series resistance R_s and the shunt conductance G of the one-diode model. In Paper VI and Paper VII a semi-manual method similar to the procedure described in Ref. [119] was used. In Paper VIII, a more elaborate least-square fitting taking into account the strongly varying slope of the $J(V)$ curve [120, 121] was used.

A drawback with the methods we have used is that there is strong co-variation between the series resistance and ideality factor, which increases the uncertainty in the fit result for these parameters. An alternative method commonly used is to determine J_0 and A from plots of J_{sc} vs. V_{oc} measured at different light intensities, which avoids fit errors induced by the series resistance. On the other hand, when the diode properties depend on the light intensity, this J_{sc}–V_{oc} method yields result that are average values for the intensities used.

3.3.2 Discussion of the standard method for $J(V)_{\mathrm{T}}$ analysis

As discussed in section 3.1.4, the diode saturation current of the dominant recombination paths can be written

$$J_0(T) = J_{00} \exp\left[\frac{-E_a}{A(T)kT}\right]. \tag{3.35}$$

For recombination in the bulk of the absorber, be it in the quasi-neutral part or in the space charge region, $E_a = E_g$ is expected. For interface recombination, $E_a < E_g$ is normally found, but as will be discussed below, E_a, as defined in Eq. 3.9 and here in Eq. 3.35, can also exceed E_g for interface recombination. The different recombination paths can be further discriminated by the value and the temperature dependence of the ideality factor $A(T)$. In particular, tunnelling contribution to the recombination in the space charge region and to the recombination at the interface modify the ideality factors [110, 111].

Eq. 3.35 is the starting point for an analysis of $J(V)_{\mathrm{T}}$ data [122] which has become standard in the CIGS community. By taking the logarithm and multiplying by $A(T)$ one obtains

$$A(T)\ln[J_0(T)] = A(T)\ln[J_{00}] - E_a\frac{1}{kT}. \tag{3.36}$$

Thus, by plotting $A(T)\ln[J_0(T)]$ vs $\frac{1}{kT}$, a straight line should be obtained with a negative slope given by the activation energy of the dominant recombination path. The method yields a well-defined activation energy in many cases, even when a temperature dependence in the ideality factor prevents the extraction of an activation energy from the standard Arrhenius plot of $\ln[J_0(T)]$ vs $\frac{1}{kT}$. The method has been used in numerous publications, including Paper VI, Paper VII, and, in a modified version, in Paper VIII. However, as brought up in Paper VII and Paper VIII and further discussed here below, there are some limitations that should be kept in mind when discussing the activation energies obtained.

Apparent activation energy $E_a > E_g$ for interface recombination

>From Eq. 3.17, given for interface recombination in the case of type inversion of the absorber surface, we can identify the pre-factor J_{00} for the saturation current with qS_pN_V, and the activation energy E_a with $\Phi^b_{p0}A$. Since $A \geq 1$, we clearly have $E_a \geq \Phi^b_{p0}$. But can E_a also exceed E_g?

Consider the case of the Anderson heterojunction model without interface charges [108]. Then the ideality factor A, given by the ratio V/V_1 of the total applied voltage to the voltage developed in the absorber, is independent of voltage and equals V_b/V_{ba}, where V_b the total built-in potential and V_{ba} is the

band bending in the absorber, see Fig. 3.2. Therefore, using Fig. 3.2, we have

$$E_a = \Phi^b_{p0} A = \Phi^b_{p0} \frac{V_b}{V_{ba}} = \Phi^b_{p0} \frac{qV_b}{\Phi^b_{p0} - E_p} \geq qV_b, \tag{3.37}$$

where the total built-in potential V_b is given by

$$qV_b = E_g + \Delta E_C - E_n - E_p. \tag{3.38}$$

If the space charge region on the n-side extends beyond the first buffer layer, then ΔE_C should here be taken as the conduction-band offset between the absorber layer and layer where the space charge region ends; similarly, E_n is the distance $E_C - E_F$ in the neutral part of this layer. Thus, for $\Delta E_C > E_n + E_p$ it is possible that the activation energy deduced from the plot of Eq. 3.36 exceeds the bandgap energy. This would require a spike in the conduction band ($\Delta E_C > 0$); in a more general situation with interface charges and tunnelling present, that might not be a necessary condition. In any case, this result shows that $E_a \geq E_g$ cannot be used as an argument against interface recombination – especially considering the additional error sources discussed here below. However, a properly determined $E_a < E_g$ should still be a safe signature of interface recombination.

Further corrections for the temperature dependence of A, E_a, and J_{00}

In general, we expect some temperature dependence also in J_{00} and E_a. For the latter, a linear temperature dependence $E_a(T) = E_a^{0K} - CkT$ can be expected from the temperature dependence based of the bandgap; for $CuInSe_2$ a linear coefficient $C \cdot k \approx 0.1$ meV/K accurately describes the temperature dependence in the range 150 K–350 K [123]. The temperature dependence of the prefactor can be approximated by $J_{00} = J_{00}^{T_{ref}} (\frac{T}{T_{ref}})^{\gamma}$, with γ in the range 0.5–3.5, depending on the recombination path [124]. Equation (3.36) can then be written

$$\begin{aligned} A(T)\ln[J_0(T)] &= A(T)(\ln[J_{00}]) + C - E_a^{0K}\frac{1}{kT}. \\ &= A(T)\left(\ln\left[J_{00}^{T_{ref}}\right] + \gamma \ln\left[\frac{kT}{kT_{ref}}\right]\right) + C - E_a^{0K}\frac{1}{kT}. \end{aligned} \tag{3.39}$$

Taking the derivative of $y = A\ln[J_0]$ with respect to $x = 1/kT$ yields the following expression for the activation energy $\tilde{E}_a$ deduced from the $A\ln[J_0]$ plot:

$$\tilde{E}_a = -\frac{d}{dx}(A(T)\ln[J_0(T)]) = +E_a^{0K} + A(T)\gamma kT - \frac{d}{dx}(A(T))\ln[J_{00}]. \tag{3.40}$$

First we can notice that the activation energy extrapolated to 0 K, E_a^{0K}, enters in the first term. But the difference with respect to the room temperature value is small – only ~0.03 eV when $C \cdot k \approx 0.1$ meV/K. The second term is generally also small, but can be significant. For example, $\gamma = 2$, and $A = 2$ at 300 K and $A = 4$ at 150 K gives a contribution of +0.1 eV to $\tilde{E}_a$. The third term is the most problematic one; if A is independent of T it is identical zero, but also a modest temperature dependence can give large contribution when multiplied by a large value of $\ln[J_{00}]$. The latter is typically in the order of 10 when J_{00} is expressed in mA/cm^2. With the values of $A(T)$ the derivative $\frac{dA}{dx}$ is about 0.05 eV, which then results in a contribution to $\tilde{E}_a$ of -0.5 eV, which is certainly significant with respect to activation energies that should be bound by the bandgap. Furthermore, the magnitude and sign of this contribution becomes dependent on the choice of measurement unit for the current, as illustrated in Fig. 4 of Paper VIII.

A modified method for extracting the activation energy of Eq. 3.35 was proposed in the master thesis of Malm [121] and in Paper VIII: neglecting the temperature dependence of J_{00}, Eq. 3.39 involves three unknown parameters, E_a, J_{00} and C, which can be found from a least square fit to experimental values of A, J_0 and kT. Once J_{00} is known, one can check the degree of linearity obtained with the fit parameters by plotting

$$A(T)\ln\left[\frac{J_0(T)}{J_{00}}\right] = +C - E_a^{0K}\frac{1}{kT}, \tag{3.41}$$

which clearly is independent of the measurement unit. This method has proven more robust than the standard one for finding a well-defined activation energy in the case of "problematic" cells with large temperature dependence in the ideality factor, as exemplified in Paper VIII. Unfortunately, it is not without complications either. When A is constant, independent of T, already Eq. 3.39 should yield a straight line. It can be seen that in this case both $\ln[J_{00}]$ and C have the same effect of shifting the model values up and down in the y-direction of the $A\ln[J_0]$ plot, and they can thus not be independently determined. E_a alone determines the slope and is well-defined. Now, if there is a temperature dependence $A(T)$, the fitting procedure tends to give unrealistically high values of C, and correspondingly unrealistically low values of $\ln[J_{00}]$. Fit results for C are typically in the range 23–26, which corresponds to a difference in activation energy of 0.6–0.7 eV between 0 K and 300 K. A probable cause for this is that a low $\ln[J_{00}]$ quenches any variations in $\frac{dA}{dx}$ causing deviations from the linear behaviour, regardless of whether the variations are caused by measurement noise or by discrepancies between measurement data and the model. (This explanation for unrealistic C values was found by Ulf Malm.) To avoid that problem, C can be limited to, e.g., 0.1 (meV/(Kk) $\approx$ 1.2. However, for the few cells investigated the quality of

this fit was not acceptable . The situation is yet modified if the temperature dependence of $\ln[J_{00}]$ is included, and more work is needed to clarify if these inconsistencies are due to the fitting procedure or to lack of applicability the model of equation Eq. 3.35 for the saturation current of the cells analysed.

An alternative approach

The complications with the standard method addressed above call for alternative approaches to analyse $J(V)_{\mathrm{T}}$ data. A fundamental problem with the approach we have used so far, is that we *first* fit a diode model to the measured $J(V)$ data at each temperature, and *then* analyse the temperature dependence of the parameters. This results in a large total number of fit parameters (six per temperature for light characteristics), with weak coupling to the actual recombination mechanism. It is difficult to uniquely determine the parameters of more than one recombination path of comparable magnitude at a given temperature, simply because there is already enough flexibility (free parameters) in the one-diode model. This suggests that more reliable fits of parameters with a clearer physical significance could be obtained by simultaneous fitting of $J(V)$ data at all temperatures. Such a fit can incorporate more than one of the diode models described in section 3.1.1, without involving a large number of parameters. The standard fit at each temperature provides a convenient way of finding good starting values. Yet another option would be to fit the data to a full numerical model using a device simulator such as SCAPS.

3.4 Influence of the Ga content

In Paper VI we made an $J(V)_{\mathrm{T}}$ analysis of CIGS cells with varying Ga content in the absorber layer. For the six samples labelled A-F, the Ga content, x in $\mathrm{CuIn}_{1-x}\mathrm{Ga}_x\mathrm{Se}_2$ was 0, 0.3, 0.4, 0.5, 0.6 and 1.0, respectively. Bandgaps, Ga content, and room temperature $J(V)$ parameters are given in Table 3.2. The analysis was made with the standard method described above. We concluded that the dominant recombination mechanism was tunnelling enhanced recombination in the space charge region for $x \leq 0.5$ (samples A-D), based on $E_a \approx E_g$ and the temperature dependence of the ideality factors. For $x = 1$ (sample F) we found $E_a < E_g$ and a large temperature dependence of the ideality factor, which indicated tunnelling-enhanced interface recombination. The sample with $x = 0.6$ (sample E) was characterized as an intermediate case, with interface recombination being more important in light than in dark conditions.

Given the error sources of the standard method, are these conclusions valid? I dare answer yes. The trend of increasing interface recombination with increasing bandgap should be correct: $E_a < E_g$ is a valid signature of interface

Table 3.2: *Bandgap E_g from* QE *measurement, Ga content x from energy-dispersive X-ray spectroscopy, and room temperature $J(V)$ parameters V_{oc}, J_{sc}, FF, and η for representative cells of samples A-F.*

	E_g	x	V_{oc}	J_{sc}	FF	η
	[eV]	[-]	[mV]	[mA/cm^2]	[%]	[%]
A	0.98	0.00	431	38.3	67.5	11.1
B	1.11	0.27	590	33.0	76.0	14.8
C	1.22	0.43	675	28.2	74.9	14.3
D	1.26	0.49	715	26.8	76.2	14.6
E	1.39	0.63	795	20.2	75.9	12.2
F	1.67	1.00	846	13.1	67.3	7.5

recombination for sample F. Since the bandgap increase with increasing Ga content occurs mainly by raising of the conduction band edge, rather than by lowering of the valence band edge, the hole barrier Φ^b_{p0} does not increase in proportion to the bandgap. This should result in a relative increase of interface recombination, see, e.g., [6] p. 327.

A few modifications should be added to the discussion, though. As shown above, $E_a \approx E_g$ is not a sufficient condition for claiming dominant bulk recombination. Numerical SCAPS simulations indicate that interface recombination is significant at V_{oc} also for samples with intermediate bandgap (1.1-1.3 eV), which can explain the high fill factors and low ideality factors observed. Again referring to SCAPS simulations, voltage-dependent current collection appears important for $E_g \geq 1.3$ eV, just as claimed by Shafarman, Klenk and McCandless [119]. In Paper VI we used as an argument against this the low value of the shunt conductance G, as determined from the slope of $J(V)$ close to 0 V. We found $G < 1$ mS/cm^2 for all samples. However, as current collection losses can increase with forward bias, in particular approaching V_{oc} they can cause significant reduction of FF and V_{oc}.

3.5 Effect of damp-heat treatment depending on Ga content

In Paper VII we examined degradation of the samples with varying Ga content used Paper VI, when these were subject to accelerated ageing in dry-heat conditions (+85°C, low pressure) and in damp-heat conditions (+85°C, 85% relative humidity, atmospheric pressure). After 800 hours, degradation had almost saturated. The observations can be summarized as follows:

- In dry heat, samples A–E are stable, while sample F degrades in all solar cell parameters.

- In damp heat all samples degrade. Degradation is smallest for intermediate bandgaps (efficiency η of sample C decreases by 27%), and severe for the endpoints (η decreases by 64% for sample F, and by 92% for sample A).
- The "blocking behaviour" of the forward current, seen for several of the cells in the initial state at low temperatures, increases with damp heat. For sample A, blocking becomes significant also for the reverse (photo)current at room temperature.
- The temperature dependence of the ideality factors increases in damp heat, in particular for wide bandgap cells.
- The effective activation energy determined from dark characteristics is almost stable at $\tilde{E}_a^{dark} \approx E_g$ for samples A–C, but decreases for sample D. For samples E-F, the lack of linear regions in the plot of $A\ln[J_0]$ vs $\frac{1}{kT}$ made extraction of $\tilde{E}$ impossible until they appeared dominated by tunnelling after 800 hours of damp heat.
- A current transport mechanism with high ideality factor, which we denote as the "2nd diode", increases by damp-heat treatment. This transport mechanism is more important in light than in dark, and more important for high than for low Ga content.
- A decrease in quantum efficiency by damp heat is observed, and is found more pronounced for longer than shorter wavelengths. The average loss in QE is smallest for intermediate bandgaps and largest for sample F, which also shows the largest wavelength-dependence in the loss. For sample A, the QE loss is large, but less wavelength-dependent (see Fig. 4 of Paper VII).
- An increase in series resistance is observed for all samples.

We concluded that the blocking behaviour was the primary cause for the severe degradation of sample A, while the increased magnitude of the "2nd diode" was the cause of the severe degradation of samples E-F with high Ga content, and important for the degradation of samples B-D.[2]

I will now try to interpret the observations in terms of:

i a damp-heat induced decrease in the absorber band bending, and

ii a damp-heat induced activation of the grain boundaries.

The band bending in the absorber and the distance ΔE_{F_n} between the conduction band and the Fermi level at the CIGS/CdS interface are given by the charge neutrality condition for the junction [106]. An increase in ΔE_{F_n} is the result of a decreased net positive charge on the *n*-side or at the interface, or an increased net negative charge on the *p*-side. There are several mechanisms that can cause such changes of the charge balance between the two sides of

[2] It can be debated whether the term "2nd diode" is appropriate for light measurements, since the current in that case can be interpreted as voltage-dependent collection losses. However, since a similar transport mechanism is present in dark measurements, it seems reasonable to assume that they are manifestations of the same recombination path.

the junction. Wennerberg *et al.* have reported decreased carrier concentration in the window/buffer structure [125] as a result of damp heat. Nguyen *et al.* have argued for the existence of detrimental acceptor states at the ZnO/buffer interface in the case of $In(OH_x,S_y)$ buffers [126], decreasing the net doping of the *n*-side. It is possible that damp-heat treatment creates acceptor states at the ZnO/CdS interface, or in the CdS buffer. Regardless of the cause, an increase of ΔE_{F_n} decreases the band bending in the CIGS layer and therefore decreases the hole barrier for interface recombination, Φ^b_{p0}. The barrier for electrons to leave the absorber, Φ^b_{n0}, increases by the same amount. (In the case of creation of acceptor state at the ZnO/CdS interface, Φ^b_{n0} can increase more than ΔE_{F_n}.)

Changes in the charge distribution can also originate from the absorber itself. According to the "defect layer model" [95, 127, 128] there exists a thin ($\sim$10 nm) layer of "ordered defect compound", ODC, with a large number of acceptor states adjacent to the interface. In the more recent Igalson model for this "p+ layer" [129], the accumulating negative charge is captured by relaxing compensating donors, present everywhere in the absorber. Thus, her model suggests a continuous variation of charged defect states rather than a distinct defect layer. In any case, with increased negative charge at or in the vicinity of the the interface, an increasing fraction of the absorber band bending will develop over this region, which decreases the band bending in the remaining CIGS. In effect, a lowering of the hole barrier Φ^b_{p0} and an increase in the electron barrier Φ^b_{n0} is obtained similar to the case of shifted position of the Fermi level at the CdS interface, considering that holes can recombine at the "ODC/CIGS interface" (directly or by tunnelling to the CdS interface), and that photo-generated electrons have to overcome the potential barrier resulting from the accumulated negative charge in the defect layer.

The effect on the cell performance caused by a change of the Fermi level at the interface (or by an increased density of negative charge in the top of the absorber) differs radically depending on the Ga content, as can be motivated with reference to Fig. 3.6.

For cells with low Ga content we expect a positive band offset ΔE_C. If the barrier for thermionic emission of electrons into the buffer is further increased by decreasing band bending in the absorber, then the interface transport factor F_{in} (introduced in section 3.2.4) can decrease drastically and reduce current collection. This can explain the severely reduced photocurrent collection and, thereby, the reduction of FF, J_{sc}, and V_{oc}. Note that $F_{in} < 1$ affects QE for all wavelengths, which fits to observations for sample A.

For cells with high Ga content, which have a negative ΔE_C, decreased band bending is less critical for the transport factor F_{in}. However, since these cells are limited by interface recombination, an increase in ΔE_{F_n}, which decreases the hole barrier Φ^b_{p0}, directly affects V_{oc}. FF is not only affected indirectly by the decrease in V_{oc}, but also by a shift to a higher ideality factor for the

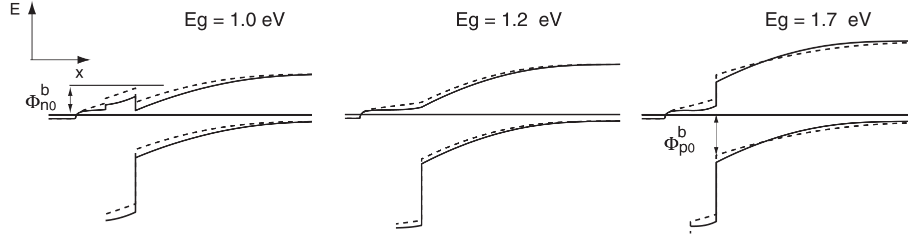

Figure 3.6: Illustration of damp-heat induced shift towards midgap of the Fermi level at the CdS/CIGS interface for absorbers with different Ga content. Left: $CuInSe_2$, $E_g \approx 1.0$ eV; Middle: $CuIn_{0.6}Ga_{0.4}Se_2$, $E_g \approx 1.2$ eV; Right: $CuGaSe_2$ $E_g \approx 1.7$ eV. For the low bandgap cell, increased barrier Φ^b_{n0} for electrons to leave the absorber is critical for carrier collection. For the high bandgap cell, decreased hole barrier Φ^b_{p0} for interface recombination is critical for the open circuit voltage. The shift was simulated in SCAPS by decreasing the doping of the buffer layers. A similar effect on the effective electron and hole barriers is obtained by increasing the negative charge in absorber in the vicinity of the CdS interface.

interface recombination as the equilibrium Fermi level at the interface moves closer to midgap.

For cells with intermediate Ga content we have the beneficial situation that an increase in ΔE_{F_n} neither affects the current collection ($F_{in} \approx 1$ still holds), nor V_{oc} (interface recombination is still small compared to bulk recombination). The observation that $\tilde{E}_a^{dark} \approx E_g$ is stable for samples B–C fits well into this picture.

Thus, different sensitivities to decreased absorber band bending can explain most of the trends observed by degradation of cells with different Ga content. Note that in Fig. 3.6 and the argument in Ref. [130], where Morkel *et al.* report $\Delta E_C = (0.0 \pm 0.2)$ eV for $CdS/CuInSe_2$, as measured from direct characterisation of the conduction band using inverse photoemission spectroscopy. As emphasized by these authors, the offset is influenced by the difference between surface and bulk bandgaps of the interfacing materials, and by interdiffusion of elements across the interface. It is not obvious whether the offset calculated right at the interface, or rather an offset between the conduction band at some distance from the interface at either side, is decisive for the current transport. However, if $\Delta E_C = 0.0$ eV is pertinent to current transport of the $CdS/CuInSe_2$ junction, then the decreased carrier collection observed for sample A is more likely the result of a barrier induced by a "p^+ layer" in the absorber [129], than by a shift of the Fermi level at the interface.

What remains to be explained is the increasing temperature dependence of the ideality factors, in particular at high Ga contents, the wavelength dependence of the QE degradation and the nature of the "2nd diode": activation of grain boundaries is one possibility. Needless to say, there can be other expla-

nations as well.

To explain the QE degradation we should look for a mechanism that can decrease the electron diffusion length *in the bulk* of the absorber. This can then also explain the voltage-dependent current collection, or, put differently, the larger influence of the “2nd diode” in light rather than in dark.

What are the motivations for involving grain boundaries? The basic argument is that since diffusion of impurities is much faster in the grain boundaries than within the grains, the grain boundaries can be expected to be more sensitive to environmental conditions than the grain interior. Turning to the diffusion lengths, SCAPS simulations indicate that extremely short minority diffusion lengths, $L_n \leq 0.1$ μm ($\tau_n \approx 0.02$ ns with μ_n = 100 cm^2/Vs), are needed to model the poor and voltage dependent current collection of the $CuGaSe_2$ sample at room temperature already in the initial state. As shown by the wavelength dependent QE degradation, this diffusion length is then further reduced by damp heat (τ_n decreased by a factor 2 or more). Such short effective diffusion lengths can be explained in terms of grain boundary recombination

$$L_n^{poly} = \left[(L_n)^{-2} + 2S_g/(D_n g)\right]^{-1/2} \tag{3.42}$$

where S_g is the grain boundary recombination velocity and g is a characteristic dimension of the grain [107]. In order to reduce the *minority* carrier diffusion length, an accumulation of positive charge, leading to downward bend bending, should be expected. Absorbers with high Ga content generally have smaller grains, which increases the influence of the grain boundaries according to Eq. 3.42. In addition, band bending caused by positively charged states at the grain boundaries could help explaining the tunnelling character of the “2nd diode”.

Are there reasons why grain boundaries should be activated by damp heat, when they appear to remain passive in dry heat? One argument is the chemical reactivity of Na, an element that appears to be important for passivating grain boundaries. Experimentally, the main electrical effect of Na is to increase the *p*-type conductivity, by increased hole concentration, increased hole mobility or both. According to calculations, the main effect of low concentrations of Na in $CuInSe_2$ is to form Na_{Cu}, which is electrically inactive, thereby decreasing or even eliminating the concentration of compensating In_{Cu} donors and thus increasing the carrier concentration [94]. Now, since Na is preferentially found at the grain boundaries [131] and since Na is known to be chemically reactive, it seems quite reasonable that the damp-heat treatment can change the chemical state of Na and give rise to increased concentration of In_{Cu} and Ga_{Cu}, or other positively charged donors at the grain boundaries. In the investigation by Malm *et al.* of damp-heat stability for cells with different absorber thickness [132], it was found that cells with absorbers deposited with additional

Na supply from a NaF pre-cursor layer, presumably having an increased Na concentration at the grain boundaries, degrade significantly more than cells without NaF pre-cursor, in consistence with an activation of the grain boundaries mediated by Na.

Damp-heat induced changes in the defect spectra have been reported and discussed several times in the literature, see e.g. Refs. [133–136]. To summarize, damp heat seems to shift the position of the Fermi level at the interface, to decrease the effective doping of the CIGS layer, and to increase the density of bulk defects. These bulk defects are all donors according to the Warsaw interpretation referred to in section 3.1.3. It is quite conceivable if part of the donor defects could be found at the grain boundaries, acting as recombination centres. Since the Ga_{Cu} transition energies are predicted about 0.3 eV deeper than the corresponding In_{Cu} transitions [93], the band bending at the grain boundaries will be deeper in CGS than in CIS if these defects are the active ones and their concentration is high enough to pin the Fermi level. If we assume that the concentration of grain boundary donors is high enough to pin the Fermi level at the grain boundary in equilibrium, but low enough for the pinning to be lifted by increased electron injection at forward bias, then it follows that this recombination path will have a high ideality factor. This is because the barrier for injecting electrons into the grain boundary valley will increase with voltage.

In conclusion, the activation of grain boundaries provides a possible explanation for the decreased diffusion length and the enhancement of a transport mechanism with high ideality factor observed by damp-heat ageing, in particular for absorbers with high Ga content. Together with the difference in sensitivity for a change in the absorber band bending, induced by degradation of the window properties or by an increase of negative charge in the the absorber close to the interface, the trends in damp-heat degradation of cells with varying Ga content can be accounted for.

3.6 Influence of the buffer layer

The influence of the buffer layer on the recombination in the cell is brought up in Paper II (ALD-In_2S_3) and Paper VIII (ALD-ZnO). In both cases, we make a connection between a negative conduction-band offset ΔE_C (i.e., conduction band of the buffer below the conduction band of the absorber, c.f. Fig. 3.2 and Fig. 3.6), and increased interface recombination caused by a decreased hole barrier Φ_{p0}^{b}. An additional reason for decreased Φ_{p0}^{b} with alternative buffers, relative to CdS, can be a lack of favourable pinning of the Fermi level close to the conduction band of the buffer.

In the case of the ALD-In_2S_3/CIGS junction, the conduction-band offset

was estimated to $\Delta E_C = (-0.25 \pm 0.2)$ eV from photoelectron spectroscopy measurements of the valence-band offset of a buffer deposited at 160°C substrate temperature, combined with optical bandgaps determined for samples deposited on glass substrates, see section 2.3.5. High interface combination fits with the low values of V_{oc} obtained for this buffer deposition temperature ($V_{oc} \approx 0.48$ V, 0.15 V below CdS reference) and reduced QE for photons absorbed close to the CIGS surface (λ = 500–600 nm). We attributed the additional QE loss for photons absorbed deeper in the absorber (longer wavelengths) to a decreased width of the space charge region, consistent with reduced absorber band bending at equal doping density.

For the ALD-ZnO/CIGS and ALD-ZnO/CIS junctions investigated in Paper VIII, Platzer-Björkman *et al.* had previously determined a negative offset $\Delta E_C = (-0.2 \pm 0.2)$ eV for CIGS absorbers and a small positive offset $\Delta E_C = (+0.1 \pm 0.2)$ eV on CIS absorbers [137]. One would thus suspect that interface recombination is more important for ALD-ZnO/CIGS junctions than for ALD-ZnO/CIS junctions. This agrees with the activation energies extracted from $J(V)_{\mathrm{T}}$ measurements in Paper VIII with the modified analysis discussed above: $E_a \approx E_g$ for both ALD-ZnO and CdS buffers on CIS absorbers, while in the case of CIGS absorbers $E_a \approx E_g$ for the CdS reference but $E_a < E_g$ for the ALD-ZnO/CIGS junction.

Also for the ALD-ZnO/CIS junction with $E_a \approx E_g$, worse V_{oc} and FF were obtained relative to the CdS/CIS reference. According to section 3.3.2, $E_a \approx E_g$ does not exclude that an increase in interface recombination is the cause of this performance loss. Since the conduction-band offset of (0.1 ± 0.2) eV determined for ALD-ZnO/CIS is comparable to the conduction-band offset (0.0 ± 0.2) eV given in Ref. [130] for CdS/CIS, an increased interface recombination is more likely to be the result of un-pinning of the Fermi level at the interface than of a difference in conduction-band offset.

3.7 Influence of the absorber thickness and of Ga grading

The dependence of recombination on the absorber thickness is brought up in Paper III. Naturally, recombination at the back contact becomes more critical as the absorber thickness is decreased. This aspect is central for the discussion of cells with thin absorbers and ZrN back contacts in Paper V, which will be covered in the following section 3.8. In Paper III we concluded that either worse material quality or increased back contact recombination explains increased recombination losses for intermediate absorber thickness. Here, I will present arguments against the idea of increased back contact recombination. In addition, an explanation for increased interface recombination observed for

cells with very thin absorbers is suggested.

In Paper III as well as in Paper V, the beneficial effect of “normal” Ga grading, i.e. an increase of the Ga content towards the back contact, is shown and discussed. Since the increasing Ga content raises the conduction band edge, the Ga gradient creates an effective field $\frac{1}{q}\frac{d\chi}{dx}$, where χ is the electron affinity, acting on the electrons in the direction towards the junction [89]. A comprehensive discussion on the beneficial effect of Ga grading as well as on the influence of the absorber thickness can be found in the thesis by Olle Lundberg [9]. The general statements made below about the effect of Ga grading are based on the conclusions in that thesis. Before turning to the thickness dependence, we can note that the main beneficial effect of Ga grading for standard cells is an improved short-circuit current J_{sc}. This is explained by improved carrier collection in the quasi-neutral region thanks to the effective field acting on the electrons in the conduction band. Somewhat surprisingly, the improvement in J_{sc} is most pronounced for absorbers with the longest minority diffusion lengths (obtained with optimal [Cu]/([In] + [Ga]) ratios of about 0.9). This is because the effective diffusion length of the electrons scales as L_e^2 as a result of the effective field in the conduction band that is caused by the Ga grading. Since device properties are not changed at the positions of dominant recombination (in the space charge region or at the interface), V_{oc} and FF are not improved by Ga grading. In terms of the notation introduced in section 3.2.4, J_L^{QNR} increases while J_0^{IFR} and J_0^{SCR} are left un-affected.

In the Lundberg thesis, the analysis of Paper III is refined by considering small differences in bandgap between cells with different thickness and Ga profile. Thus, the trends in V_{oc} relative to the bandgap ($\Delta V_{oc} = V_{oc} - (E_g/q-$ 0.6 V)), rather than the trends in V_{oc} itself, are considered. Likewise, the J_{sc} values are normalized to J_{sc}^{max}, defined as integrated current density available in the standard spectrum between $\lambda = 360$ nm and the cut-off given by the the bandgap [9]. The trends of these relative $J(V)$ parameters are shown in Fig. 3.7. Turning first to the samples without grading, it can be seen that the efficiency drops from about 16% at d_a = 1.8 μm to about 8% at d_a = 0.36 μm. Most of this decrease is due to decrease of the short circuit current J_{sc}^{rel}, which decreases from almost 80% to just above 50% of the available current J_{sc}^{max}. This is only partly caused by the decreased generation (absorptance) in the CIGS layer, which was discussed in chapter 2; as shown by Fig. 8 in Paper III, a large fraction of the current loss is caused by increased collection losses with decreasing absorber thickness. For intermediate thickness, e.g., d_a = 0.80 μm in this figure, the collection losses are seen in the QE for long wavelengths only, which indicates decreased collection in the quasi-neutral region of the absorber. This could result from an increased influence of the back contact, or from decreased material quality (possibly induced by smaller grains), or a combination thereof. For the thinnest samples, collection is decreased also

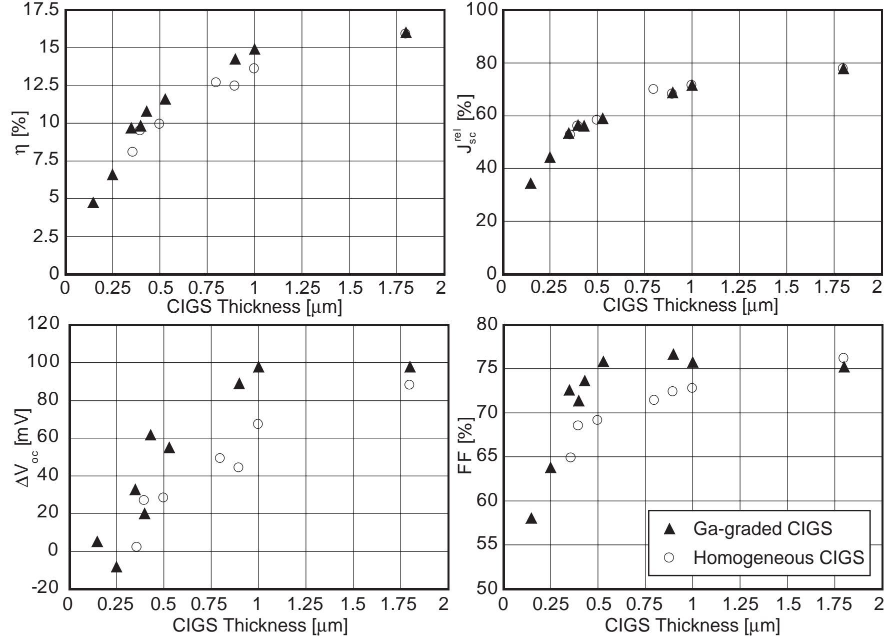

Figure 3.7: Efficiency η, normalized short circuit current J_{sc}^{rel} (see text), $\Delta V_{oc} = V_{oc} - (E_g/q - 0.6V))$, and fill factor FF as a function of absorber thickness d_a for samples mad with (filled triangles) and without (open circles) Ga grading. The figure is reproduced from the thesis by O. Lundberg [9].

for short wavelengths, which indicates recombination at the buffer/absorber interface, c.f. section 3.2.3.

The decrease in V_{oc} is larger than what would result from from the decrease in J_{sc} if the saturation current and the ideality factor were kept constant. The decrease in ΔV_{oc} caused by a decrease in J_{sc} can be estimated from the relation

$$V_{oc} \approx \frac{AkT}{q} \ln \left[\frac{J_{sc}}{J_0} \right] \tag{3.43}$$

. Table 3.3 details parameters for the three cells with different absorber thickness appearing in Fig. 8 and Fig. 11 of Paper III. If J_0 and A were constant at the values obtained for the thicker cell with $d_a = 1.80$ μm ($J_0 = 7 \cdot 10^{-7}$, $A = 1.4$), the decrease in ΔV_{oc} caused by a decreased J_{sc} would be $\sim$5 mV for the cell with $d_a = 0.80$ μm and $\sim$15 mV for the cell with $d_a = 0.35$ μm, which is clearly less than the observed decrease of $\sim$40 mV and $\sim$85 mV, respectively.

Since the ideality factor from dark $J(V)$ increases with decreasing absorber thickness, see Table 3.3, we can exclude that increased back contact recombination is the primary cause of the increase of J_0 and decrease of V_{oc} – if that

Table 3.3: *Absorber thickness d_a, normalized short circuit current J_{sc}^{rel} (see text), $\Delta V_{oc} = V_{oc} - (E_g/q - 0.6V)$, and diode saturation current J_0 and ideality factor A obtained from dark characteristics for the three cells without Ga grading of the absorber appearing in Fig. 8 and Fig. 11 of Paper III.*

d_a	J_{sc}^{rel}	ΔV_{oc}	J_0	A
[μm]	[%]	[mV]	[mA/cm^2]	[-]
1.8	77	88	$7 \cdot 10^{-7}$	1.4
0.80	70	50	$6 \cdot 10^{-6}$	1.6
0.35	52	2	$8 \cdot 10^{-5}$	1.9

were the case, the effective ideality factor should decrease towards 1. It is important here that ideality factors from dark $J(V)$ are compared; in light $J(V)$, back contact recombination can result in voltage-dependent current collection which increases the ideality factor obtained from the one-diode model.

Cells with intermediate thickness maintain high QE for short wavelengths, which speaks against increased interface recombination. Thus, for these cells, the most likely explanation for decreased V_{oc} is a decreased minority carrier diffusion length, which could then also explain increased collection losses. The fact that the elemental composition of the different absorbers is comparable, while the grain size decreases with decreasing thickness (see Fig. 2 in Paper III), suggests that the decreased effective diffusion length is a result of the influence of the grain boundaries. Also note from the dark and light $J(V)$ of Fig. 11 in Paper III, that the shunt conductance increases with decreasing thickness, and is more important in light than in dark. This shunt can be identified with the influence of the "2nd diode", which was introduced in section 3.5 and suggested to be related to grain boundary recombination. It should be emphasized here, that the electrical activity of the grain boundaries depends on the detailed properties (crystal orientation, composition, etc.) of the CIGS absorber [138]. Thus, the suggested increase in the influence of the grain boundaries by damp-heat treatment and for decreasing absorber thickness should be expected to depend on the absorber deposition process.

As for the cells with the thinnest absorbers, we see signs of additional degradation due to interface recombination. This might be surprising, since the formation of the junction was made with identical processes for deposition of buffer and window layers for all absorbers. However, it is clear that for sufficiently thin absorbers, the depletion region will extend all the way to the back contact; this has also been verified by $C(V)$-measurements [132]. Thus, for absorber thickness below a critical value $d_a^{crit} = W_{a0}$, where W_{a0} is the width of the depletion region that would have been obtained with a thick absorber having the same doping density N_A, the band bending in the CIGS layer is

limited to

$$V_{ba}^{thin} = \frac{N_A d_a^2}{2\varepsilon_{sa}} < V_{ba}^{thick} = \frac{N_A W_{a0}^2}{2\varepsilon_{sa}}, \tag{3.44}$$

where ε_{sa} is the permittivity of the absorber. This limitation on V_{ba} will shift the Fermi level at the buffer interface towards mid-gap, and thus increase interface recombination and decrease current collection for all wavelengths by decreasing the transport factor F_{in}.

Now, let us consider the effect of Ga grading for different absorber thicknesses d_a. With Ga grading, the J_{sc}^{rel} decrease follows the trend obtained for the samples without grading, while ΔV_{oc} and FF are almost constant down to $d_a \approx 0.9\ \mu$m and $d_a \approx 0.5\ \mu$m, respectively, where they start to decrease. This can be explained as follows:

- For thin absorbers, the Ga gradient, creating an additional field for the electrons, and the space charge region at zero bias will overlap.
- Improvement of carrier collection with grading is not significant in thin absorbers at short circuit, since the space charge region extends through most of the absorber. Thus J_{sc} is not improved.
- At forward bias, the space charge region narrows and the electric field decreases, which degrades carrier collection in cells without grading. With grading, the additional field acting on the electrons maintains carrier collection and thus suppresses fill factor losses and V_{oc} losses caused by voltage-dependent carrier collection.
- Below the critical thickness where the absorber becomes fully depleted, V_{oc} and FF start to degrade because of increased interface recombination, independent of the Ga grading. This effect is seen earlier in V_{oc} than in FF. This is because the decrease of the hole barrier Φ_{p0}^{b} that follows from a decreased V_{ba} is more critical than the increase in ideality factor of the interface recombination obtained for the same reason.

To summarize, similar to the case of damp-heat treated cells, changes in absorber band bending and a degradation of minority carrier diffusion length, suggestively related to grain boundaries, can be invoked to explain the increase in recombination observed for cells with decreasing absorber thickness. The main effect of the Ga grading in this case appears to be to decrease the voltage-dependent current collection losses caused by decreased effective diffusion electron length.

Finally, the finding by Malm *et al.* that cells with very thin absorbers ($d_a = 0.36\mu$m) are stable in damp heat, can be appreciated from the concept of critical thickness for the absorber band bending: since V_{ba}^{thin} is limited by the thickness, it will not necessarily decrease further due to degradation of the window or un-pinning of the Fermi level at the interface. This implies that the hole barrier limiting V_{oc} in these devices can remain constant by damp-heat ageing.

3.8 Electronic losses with ZrN back contact and the beneficial effect of $MoSe_2$

In chapter 2 the optical gain obtained by using ZrN or TiN as back contact instead of Mo was discussed. In this section I will discuss the electronic losses that unfortunately are induced by the CIGS/ZrN contact, as well as the benign effect of introducing an interfacial contact layer of $MoSe_2$. These effects were shown in Paper V and are also discussed in the master thesis by Sebastian Schleussner [23]; the case of TiN has not been electrically analysed beyond the room temperature $J(V)$ shown in Paper IV, and will not be covered here.

In the recombination analysis of this chapter so far, I have emphasized how different recombination paths are operative in parallel, and to show how a controlled variation (Ga-content, buffer layer) can shift the balance between these paths. In this section, the controlled variation is the change of the back contact for samples having thin absorber layers, see Fig. 3.8, which makes the device performance sensitive to the properties of the back contact. One would therefore expect that if an increase in recombination is observed, then it is surely due to increased back contact recombination. This is also what I will argue for here, based on the overall clear picture from Paper V: with ZrN and without grading (structure A in Fig. 3.8) performance is worse than for Mo references; with Ga grading (structure B) performance is closer to the Mo reference, and with $MoSe_2$ (structure C) the ZrN sample even outperforms the Mo reference.

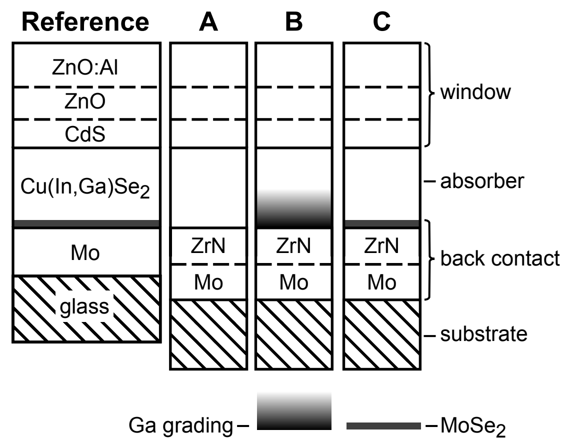

Figure 3.8: Standard structure of the reference sample with Mo contact and modified structure of the ZrN back reflector samples investigated: direct ZrN (A), with Ga grading (B), and with $MoSe_2$ contact layer (C).

However, before proceeding to the more detailed motivation for the importance of the back contact, let me just stress that that replacing Mo by ZrN can affect the device properties in several ways, apart from changing the electric properties of the back contact. The most important of these additional effects is the different supply of Na. Since ZrN acts as a barrier for Na, it prevents the diffusion of Na from the soda-lime substrate glass that takes place with Mo back contact. We have therefore added Na by means of a NaF pre-cursor layer, but the Na supply to the CIGS absorber can be different with respect to the reference also in this case; with a sufficiently thick NaF layer the Na content in the absorber with ZrN substrate will be higher than in the reference absorber, since the Mo substrate of the latter will act as a Na sink.[3] The change of back contact can also be expected to influence the nucleation of the CIGS growth, and, through difference in emissivity, affect the substrate temperature. The above can, and does, influence important properties of the absorber, such as composition, doping level, crystal orientation and surface roughness. The situation gets even more complex when the additional $MoSe_2$ layer is added. So far we have not gained full control of the experimental parameters; work is still in progress.

3.8.1 Suggested band diagrams at the back contact and effect on device performance

To explain the observations found in Paper V, we propose that the band diagrams resulting from the structures in Fig. 3.8 can be described according to the schematic illustration in Fig. 3.9. In the case of the reference with Mo back contact, we believe that an interfacial $MoSe_2$ layer increases performance by lowering the contact resistance and by creating a barrier for electrons at the back contact, thereby reducing back contact recombination. The existence and benign effects of a $MoSe_2$ layer will be discussed in the next subsection.

For structure A, we suggest that a barrier for majority holes is formed at the CIGS/ZrN interface. Such a barrier will give rise to a contact resistance (R_c), which adds to the total series resistance (R_s) of the device and thereby reduces the fill factor. Furthermore, with the proposed band bending, the back contact will act as a sink for electrons, which increases back contact recombination and can explain the lowering of both V_{oc} and FF relative to the reference. Such a sink is also critical for the collection of electrons photogenerated deep in the absorber, and therefore counteracts the gain in the quantum efficiency for long wavelengths expected from the increased absorber absorptance $A_a(\lambda)$ obtained with ZrN back contacts.

[3] For TiN, no NaF precursor was necessary to achieve high performance, which implies that (thin) TiN is less a efficient diffusion barrier for Na than (thicker) ZrN.

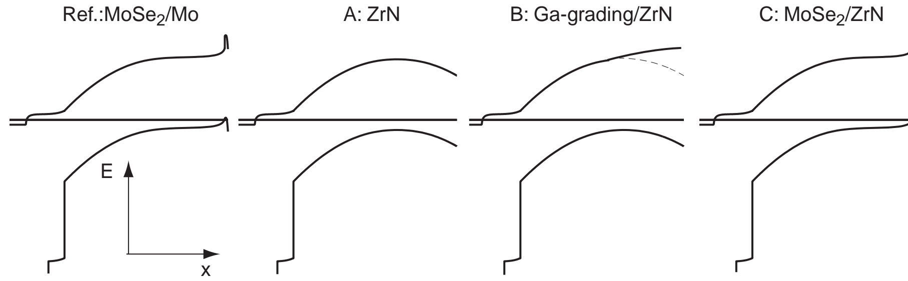

Figure 3.9: Proposed band diagrams for the samples of Fig. 3.8 with different back contacts. For the reference sample with Mo contact and for sample C with ZrN contact a 10 nm thick $MoSe_2$ layer p^+-doped layer with $E_g = 1.4$ eV is assumed. For sample A, a 0.45 eV Schottky barrier is proposed for the CIGS/ZrN contact. In the case of sample B, an increased Ga content towards the back contact increases the conduction band relative to sample B, but the hole barrier in the conduction band is left un-changed.

In the case of structure B, the Ga grading causes a potential barrier that decreases the number of minority electrons that reach the back contact interface, see Fig. 3.9. Thereby current collection is improved at short circuit conditions, and a larger fraction of the optical gain with a ZrN back reflector is utilized, resulting in an increased QE level and a J_{sc} significantly higher than in the reference sample. However, this barrier does not completely suppress back contact recombination, so V_{oc} and FF are still lower than for the reference. FF is further lowered by a value of the series resistance R_s significantly higher than in the reference, which can be explained by a high contact resistance R_c; since Ga grading leaves the valence band practically unchanged, it should be expected that a hole barrier present in structure A remains in structure B, as indicated in Fig. 3.9.

With the $MoSe_2$ contact layer in structure C, the series resistance of the reflector sample is similar to that of the reference, indicating a low contact resistance R_c. Furthermore, recombination in this case is *lower* for the reflector sample than for the reference, as manifested in lower J_0, and higher V_{oc} and FF. On the other hand, in spite of better optical performance, J_{sc} is only at about the same level, indicating collection losses. As argued in Paper V, these results can be explained by an efficient passivation of the recombination at the back contact with a $MoSe_2$ layer, in combination with a higher doping level in the reflector sample. A higher doping level, which was deduced from capacitance-voltage measurements, can increase V_{oc} through an increased built-in potential, but also decrease current collection by a narrowing of the space charge region.

3.8.2 On the contact barrier of the CIGS/ZrN junction

The difference in doping level just mentioned in the case of structure C is an example of a second-order effect resulting from the change of back contact. Could such effects account for the main part of the performance loss? What are really the reasons for claiming increased back contact recombination with ZrN?

I argued against back contact recombination for the samples with thin absorbers in Paper III, based on an increase in the ideality factors relative to samples with thick absorbers. Looking at the ideality factors shown in Table II of Paper V, the ZrN samples of structure A and B also show increased ideality factor with respect to the Mo reference. But, firstly, these values are for light measurements, where a voltage-dependent current collection caused by back contact recombination can show up as a high ideality factor in the one-diode model. Secondly, if there is a large hole barrier at the back contact, as suggested in Fig. 3.9, then the electron and hole concentrations will be comparable, which implies that the back contact recombination is no longer characterized by an ideality factor $A = 1$. Thus, the ideality factors shown in Paper V can neither be used as an argument for nor against increased back contact recombination.

However, the barrier for holes at the CIGS/ZrN interface implied by the increase in series resistance is so large that it will certainly result in increased back contact recombination. The series resistance R_s in standard cells is about 0.5 Ωcm^2 and is dominated by resistance for the lateral current transport in the window layer; the contribution from the back contact resistance R_c is negligible. But for cells fabricated with CIGS/ZrN contact, we have consistently observed an increase in the series resistance by some 0.3–3.5 Ωcm^2 compared to reference cells with CIGS/Mo contact. The higher values in the range are obtained from fits to dark measurements, and should be more reliable. This indicates the existence of a barrier for the majority holes at the back contact. The current over this barrier should be approximately described by the expression for thermionic emission over a Schottky barrier [139]. Differentiating with respect to the (small) contact voltage yields a contact conductance

$$G_c = \frac{1}{R_c} = \frac{q}{kT} A^* T^2 \exp\left[-\frac{\Phi_b}{kT}\right], \tag{3.45}$$

where Φ_b is the barrier height and A^* is the effective Richardson constant [140]

$$A^* = \frac{4\pi q m^* k^2}{h^3}. \tag{3.46}$$

A^* can be estimated to 22 A/(cm^{2}K^2) by using a value $m^* = 0.18 \cdot m_0$ for the effective mass of the holes in the valance band, estimated from $N_V = 2 \cdot 10^{18}$

cm^{-3}. Solving Eq. 3.45 for the barrier height and setting $T = 300$ K, results in

$$\begin{aligned} \Phi_b &= kT \ln\left(A^* R_c q T / k\right) \\ &= 0.39 + 0.026 \ln\left(A^* R_c\right) \text{ eV}, \end{aligned} \tag{3.47}$$

with the product A^*R_c expressed in units V/K^2. With $A^*R_c = 22 \cdot 1$, a barrier height of 470 meV is obtained. The barrier estimate is insensitive to the exact values of A^* and R_c; decreasing (increasing) the product A^*R_c by a factor 10 lowers (increases) the estimate by 60 meV. This means that the measured increase in series resistance implies a contact barrier comparable to the absorber band bending! Such a large barrier has been anticipated in Fig. 3.9, and its detrimental effect on device performance has been verified by numerical SCAPS simulations.

Is a barrier of about 0.5 eV to be expected from the material properties of CIGS and ZrN? Without an interfacial $MoSe_2$ layer and in the ideal case without any interface charge, the barrier at the CIGS/ZrN interface is given by [139]

$$\Phi_b = E_g + \chi_a - \Phi_m = \Phi_a + E_p - \Phi_m \tag{3.48}$$

where Φ_m is the work function of the (ZrN) back contact, and χ_a and Φ_a denote the electron affinity and work function of the (CIGS) absorber, respectively. $E_p = kT \ln \frac{N_V}{N_A}$ denotes the distance between the Fermi level and the valence band in the quasi-neutral part of the absorber, and is found to lie in the range 0.1–0.2 eV for typical doping concentrations (N_A in the range $1 \cdot 10^{15}$–$5 \cdot 10^{16}$ cm^{-3}). The absorber work function Φ_a has been measured by photoemission to 5.2 eV for cleaved (011) surfaced of single crystalline $CuInSe_2$ [141], and to (4.9 ± 0.1) eV for Cu(In,Ga)Se_2 prepared by RTP (which results in low Ga content at the surface) [142]. Measurement results by Kelvin force microscopy are reported at ~ 4.9 eV for $CuGaSe_2$ [143] and at 5.3-5.5 eV for co-evaporated $CuIn_{0.7}Ga_{0.3}Se_2$ [138]. These results indicate that the edge of the valence band in CIGS should be located at $\Phi_a + E_p = (5.3 \pm 0.3)$ eV below the vacuum level. Subtracting the barrier of 0.5 eV, we get from the simple model of Eq. 3.48 an estimate of the ZrN work function of $\Phi_m \approx (4.8 \pm 0.3)$ eV. Since inclusion of tunnelling and other refinements of the thermal emission model will tend to lower the effective barrier, this can be considered an upper bound on the ZrN work function.

The value of Φ_m for ZrN obtained in the estimation above fits well with experimental data. The work function of ZrN_x with varying nitrogen content x has been measured by Kelvin probe in air, and was reported to vary between 4.4 eV and 4.7 eV, see Ref. [144] and references therein. In Paper IX, we report on work function measurements for ZrN films sputtered in the same deposition

system as used for making the solar cell back contacts, with the nitrogen gas flow used in the reactive sputtering varied from 12 sccm to 20 sccm. The work function was determined from electrical characterisation of ZrN_x/SiO_2/p-Si MOS capacitor structures, and measured after sequential annealing steps. After initial form gas anneal at 400°C for 30 min, the values obtained increased with increasing nitrogen flow from 4.0 eV at 12 sccm to 4.6 eV at 20 sccm . After rapid thermal processing at 600°C for 30 s in N_2 atmosphere, the work function increased to 4.2 eV at 12 sccm nitrogen flow to 4.9 eV at 20 sccm nitrogen flow, see Fig. 4 of Paper IX. The mechanism behind the variations found has not yet been settled; one possibility is that incorporation of oxygen at the ZrN_x/SiO_2 interface affects the work function; another possibility is the influence of interface states. In any case, the values obtained for the work function of ZrN are compatible with the barrier deduced for the CIGS/ZrN contact.

3.8.3 $MoSe_2$ as a contact layer

The introduction of an interfacial $MoSe_2$ layer in sample C could reduce the high contact resistance observed for structures A and B. Since the decreased contact resistance implies decreased band bending, it follows that back contact recombination also decreases, which improves the open circuit voltage and the carrier collection. That an interfacial $MoSe_2$ layer can be beneficial for device performance in CIGS solar cells is well established. The formation of an interfacial layer of $MoSe_2$ between a Mo back contact and a CIGS absorber prepared by the three-stage process was investigated by Wada, Nishiwaki, Kohara and co-workers [145, 146]. They found that the properties of the $MoSe_2$ layer depend on the atomic composition of the evaporation flux. When only Se was evaporated, they found a thin ($\sim$10 nm) layer of $MoSe_2$, with the c-axis perpendicular to the Mo substrate. When In, Ga and Se were evaporated with the substrate at 350°C, followed by the evaporation of Se at 550°C, they obtained a thicker layer ($\sim$100 nm) with the c-axis parallel to the Mo substrate.[4] Evaporation of Cu-rich material was found to inhibit the formation of $MoSe_2$.

Later, the same group of authors also found, using SiO_2 as a Na barrier below the Mo layer, that the absence of Na inhibited the formation of a $MoSe_2$ layer. For devices with Na barrier and without $MoSe_2$ layer they observed an increasing series resistance with decreasing temperature, and deduced that the back contact in this case acted as a Schottky barrier. For devices without

[4] Since $MoSe_2$ is a layered semi-conductor with a relatively large spacing ($c = 1.3$ nm) and weak cohesion between the (crystal) layers, the crystal orientation of the $MoSe_2$ film is important for the adhesion of a CIGS/$MoSe_2$/back contact structure. The c-axis perpendicular to the Mo substrate corresponds to the case expected to give weak adhesion.

Na barrier and with a $MoSe_2$ layer, the series resistance was low also at low temperature. From these observations, it was concluded that the $MoSe_2$ interface layer is essential for establishing a beneficial ohmic behaviour of the CIGS/Mo back contact [147, 148]. The formation of an interfacial layer of $MoSe_2$ and its ability to establish an ohmic contact has also been reported for $CuGaSe_2$ grown on Mo substrates by chemical vapour deposition [149].

Since the interfacial $MoSe_2$ layer can enable an ohmic contact for the p-type CIGS, it can probably be characterized as a p^+-type semi-conductor with high carrier concentration, as assumed in Fig. 3.9. A bandgap of the $MoSe_2$ layer larger than the bandgap of the absorber then is beneficial, since it creates a barrier preventing electrons in the conduction band from recombining at the back contact. In Refs. [147, 148], a bandgap of 1.4 eV was deduced from an analysis of QE spectra, which can be compared with 1.1-1.2 eV reported for sputtered $MoSe_2$ films as well as single crystals [150].

Our findings in Paper V are in agreement with the results cited above. Since the beneficial effect of $MoSe_2$ was already known, the significance of Paper V with respect to $MoSe_2$ is rather that this beneficial effect can be obtained without having a Mo back contact. This approach has recently been employed to form an ohmic contact between CIGS and ZnO:Al [151], which opens a perspective for efficient bi-facial solar cells.

Concerning any alternative back contact/layer material which, like ZrN, does not react with Se, another interesting aspect is that the maximum thickness of the $MoSe_2$ contact layer can be controlled, and optimized, by the thickness of the Mo pre-cursor. It can be noted from Paper V that a Mo precursor layer of thickness of only about 2 nm was sufficient for obtaining a beneficial effect. We are currently investigating how the formation of $MoSe_2$ and the device performance depend on the thickness of the Mo precursor and on the supply of Na.

4. Conclusions

I would like to summarize the results and discussions presented in the two previous chapters on generation and recombination in the following way:

Regarding generation

- The optical properties of the layers in the standard CIGS solar cell structure as well as of ALD-In_2S_3 have been experimentally determined.
- With a specular optical model based on these optical properties, the main features of the optical response of the CIGS solar cell could be reproduced.
- An extension to ideally Lambertian scattering was employed to investigate the potential for maintaining high current generation in CIGS cells with thin absorber layer by means of light trapping.
- Two structures with optically improved back contacts, TiN and ZrN, have been realized. In both cases the current gain was small ($\sim$1 mA/cm^2), but significant and in agreement with model predictions.

Regarding recombination

- A generalized version of the reciprocity theorem for carrier collection has been applied to simulate the collection function in CIGS solar cells.
- Complications involved in the standard procedure for analysing $J(V)_{\mathrm{T}}$ data have been discussed. In particular, it has been found that an apparent activation energy equal to or larger than the bandgap energy, cannot be taken as evidence against dominant interface recombination.
- It was found from a study of damp-heat ageing of cells with different Ga content in the absorbers, that cells with intermediate Ga content were the most stable ones. An explanation involving different sensitivity, depending on the Ga content, to decreased absorber band bending and activation of grain boundaries is suggested.
- The optical gain obtained with a ZrN back contact was found to be counteracted by increased back contact recombination and contact resistance. Strategies to avoid these electronic problems were developed. It was experimentally demonstrated that the inclusion of an interfacial layer of $MoSe_2$ could suppress the electronic losses, and allow for an overall improved efficiency of devices with ZrN back contact compared to reference devices with Mo back contact.

5. Summary in Swedish

Om genererering och rekombination av elektron-hål-par i $Cu(In,Ga)Se_2$-tunnfilmssolceller

Inledning

En bidragande orsak till den stora och snabba och förbättring av hälsa, medellivslängd och materiell välfärd som, globalt sett, skett de senaste hundra åren är ökad användning av energi, och då inte minst elektricitet. Korrelationen mellan levnadsstandard, så som den mäts av FN:s utvecklingsorgan UNDP, och energianvändning är tydlig [2]. Man kan förvänta, och hoppas, att fortsatt förbättring av människors materiella levnadsvillkor kommer att ske, vilket ger en förväntan på ytterligare ökad energianvändning. Samtidigt sätter risker förknippade med global uppvärmning [3] begränsningar på hur mycket ytterligare energi som anses acceptabelt att tillföras genom förbränning av fossila bränslen.

Det vore önskvärt om ökad efterfrågan på energi kunde mötas med ökad tillförsel av *förnyelsebar* energi. Med dagens teknik för förnyelsebar energi kan dock inte tillräckligt mycket energi tillföras till attraktiva priser. Detta gäller speciellt förnyelsebar elektricitet från solceller, som är ämnet för denna avhandling.

Solceller

Solceller kan direkt omvandla en del av energin i det infallande solljuset till elektricitet. Elproduktion med solceller har många attraktiva egenskaper: den sker utan vare sig utsläpp eller buller, den har en mycket stor global potential, tekniken är modulär och skalbar, och den grundläggande enheten i solcellssystem, solcellsmodulen, är robust och håller länge – idag lämnar tillverkarna normalt en garanti på 20 år.

Men solcellstekniken innebär också en del utmaningar, t.ex. relativt stort ytbehov, och krav på samordning med annan elproduktion eller på lagring av el för att möta efterfrågan också när solen inte lyser. Den viktigaste utmaningen är dock att få ned priset. Det höga priset på solcellsel är den viktigaste anledningen till att solceller idag bara står för en dryg tiotusendel av den totala eltillförseln i världen.

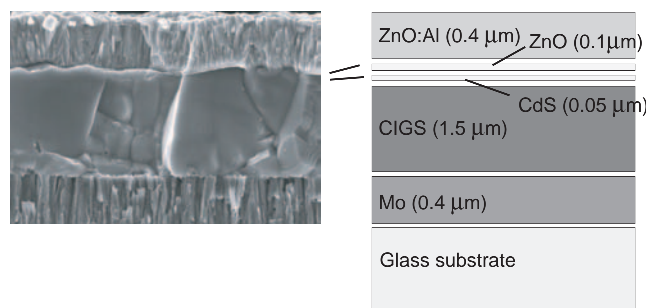

Figure 5.1: Svepelektronmikroskopbild (till vänster) och schematisk illustration av standardstrukturen för Cu(In,Ga)Se_2-solceller i genomskärning.

Den stora potentialen har ändå motiverat marknadsstödjande åtgärder, framför allt i Tyskland och Japan, som starkt bidragit till att priset sjunkit med cirka 30% de senaste åren. För kiselsolceller, den klart dominerande solcellstekniken, visar erfarenheten hittills att skalfördelarna med ökad volym på tillverkningen är sådana, att varje gång den ackumulerade produktionen av solceller fördubblas, så sjunker priset med cirka 20%.

Jämfört med kiselsolceller bedöms solceller byggda på tunnfilmsteknik ha potential att nå lägre kostnader, bland annat pga av mindre materialåtgång och möjlighet till långt gången automatisering i tillverkningen. Hittills har dock inte någon tunnfilmsteknik nått någon större kommersiell framgång. För att nå ett genombrott är de viktigaste kraven (i) en låg tillverkningskostnad, (ii) en verkningsgrad jämförbar med den för kiselsolceller (13-20%), (iii) bevisad lång teknisk livslängd och (iv) liten miljöpåverkan i produktionen.

CIGS-solceller

Tunnfilmssolceller baserade på Cu(In,Ga)Se_2, eller CIGS, utgör ett lovande alternativ att få möta kraven för kommersiell elproduktion från solceller. De ingående skikten är mycket tunna, totalt mindre än 3 μm, och bärs upp av vanligt fönsterglas. Därmed är mängden aktivt material som åtgår till en solcellsmodul liten.

En CIGS-tunnfilmssolcell består av fem separata skikt som kan delas upp i bakkontaktskikt (molybden, Mo), absorberande skikt (CIGS), buffertskikt (kadmiumsulfid, CdS och odopad zinkoxid ZnO), och genomskinlig framkontakt, “fönster” (aluminiumdopad zinkoxid, ZnO:Al) , se figur 5.1

CIGS-skiktet tillverkas genom samförångning av de ingående grundämnena koppar, inidum, gallium och selen på en molybdentäckt glasskiva som håller en temperatur på cirka 500°C. Resultatet blir en polykristallin film med en tjocklek av cirka 1,5 μm. Molybden- och zinkoxidskikten tillverkas genom sputtring och det tunna buffertskiktet av kadmiumsulfid tillverkas med en våtkemisk metod.

Arbetsprincip, generering och rekombination

Den grundläggande arbetsprincipen för solceller är ljusabsorption följd av laddningsseparation. Genom absorption kan energin i en ljuspartikel, en foton, tas emot av en elektron, som exciteras till ett högre energitillstånd och lämnar efter sig "ett hål" som är positivt laddat – ett elektron-hål-par genereras. Genom en lämplig elektronisk struktur på materialen i solcellen så förs den exciterade elektronen och hålet åt olika håll, laddningarna separeras. Om de når fram till kontakten på respektive sida så erhålls en ström i en yttre krets ansluten till solcellen. Men det kan också hända att en exciterad elektron faller tillbaka till sitt lägre tillstånd. Därvid försvinner även ett hål; man säger att ett elektron-hål-par har rekombinerat.

En solcells verkningsgrad begränsas därför av hur mycket ström som alstras genom absorption av fotoner som genererar elektron-hål-par (generering) och hur många av de genererade laddningsbärarna som går förlorade innan laddningarna har separerats hela vägen till kontakterna (rekombination). Genereringen är gränssättande för den maximala strömmen. Eftersom rekombinationen ökar med den spänning som utvecklas över solcellen, så begränsar rekombinationen den maximala spänningen för en given generationsström.

De flesta solceller är uppbyggda på samma sätt som en halvledardiod, med en n-dopad och en p-dopad sida, en så kallad pn-övergång. Det är då skillnaden i dopning som är den struktur som ger upphov till laddningsseparation. I den CIGS-baserade solcellen består n-sidan av de tre översta skikten, medan CIGS-skiktet är p-dopade delen av dioden. Det är i CIGS-skiktet huvuddelen av absorptionen av solljuset sker och därmed också där som huvuddelen av den fotogenererade strömmen alstras.

Syfte

Det övergripande syftet med avhandlingen var att bidra till förbättrad modellering av CIGS-solceller, dels genom att *förbättra den optiska modellen* av CIGS-solceller – som kan användas till att svara på frågan *hur många elektron-hål-par genereras och var någonstans i solcellen sker detta?* dels genom att *förbättra den elektroniska modellen* som kan användas för att svara på frågan *hur många var elektron-hål-par rekombinerar och var någonstans i solcellen sker detta?* Med en bättre modell så förbättras möjligheterna att optimera CIGS-strukturen för ökad verkningsgrad.

Den optiska analysen användes också som ett verktyg för att nå ett mer direkt tekniskt mål, nämligen att finna sätt att ytterligare minska tjockleken på det absorberande CIGS-skiktet från 1,5 μm till 0,5-1,0 μm utan att tappa alltför mycket i verkningsgrad. Med tunnar skikt minskar materialåtgång och deponeringstid, och därmed tillverkningskostnaden.

Resultat

Optisk karaktärisering och modellering

För att kunna beräkna genereringen av elektron-hål-par krävs en optisk modell som kan beskriva hur de olika materialen i strukturen absorberar och reflekterar solljuset. De optiska egenskaperna, d.v.s. komplext brytningsindex som funktion av våglängd, har bestämts för alla skikt i CIGS-solcellen genom analys av reflektans- och transmittansmätningar. Genom att använda de erhållna optiska egenskaperna som indata, kunde huvuddragen den kompletta solcellsstrukturens absorption och reflektion av ljus som funktion av våglängd reproduceras med en spekulär optisk modell, d.v.s. en modell som försummar ljusspriding orsakade av ytojämnheter.

Genom att utvidga modellen till att inkludera fallet med ideal Lambertiansk ljusspridning vid CIGS-skiktets båda gränsytor så kunde potentialen för att bibehålla hög fotoström för tunna CIGS-skikt bedömas. Den genererade strömmen simulerades som funktion av CIGS-skiktets tjocklek för bakkontakter med olika optiska egenskaper.

Optiskt förbättrade bakkontakter

Den optiska analysen visade att reflektionen i gränsytan mellan CIGS och bakkontakten av Mo är låg. När CIGS-skiktet görs tunnare ökar den andel ljuset som når bakkontakten utan att absorberas, och det blir därför viktigare att ha hög reflektion i detta gränsskiktet.

Två alternativa bakkontakter, titannitrid (TiN) och zirkoniumnitrid (ZrN) har undersökts experimentellt. Båda gav en liten men signifikant optisk förbättring av solcellsströmmen, i god överensstämmelse med förutsägelserna från den optiska modellen, se figur 5.2.

Rekombinationsanalys genom elektrisk karaktärisering

Den dominerande metoden för att analysera rekombination i solceller är att mäta ström-spänningskurvor vid olika temperaturer. Det sätt att analysera mätdata som är mest använt för CIGS-solceller diskuteras i avhandlingen, och flera komplikationer påpekas.

Vidare föreslås en ny metod för att beräkna den så kalled uppsamlingsfunktionen, som anger, som funktion av positionen i solcellen, hur stor sannolikheten är att ett elektron-hål-par som genereras verkligen bidrar till fotoströmmen i den yttre kretsen. Metoden bygger på en generalisering av ett tidigare känt teoretiskt samband.

Huvuddelen av rekombinationsanalysen ägnas åt att diskutera den elektroniska orsaken till den variation i prestanda som erhålls för solceller som tillverkats på olika sätt (olika buffertskikt, absorbatortjocklek, Ga-halt, och bakkontakt) och när de utsätts för hög temperatur och hög luftfuktighet.

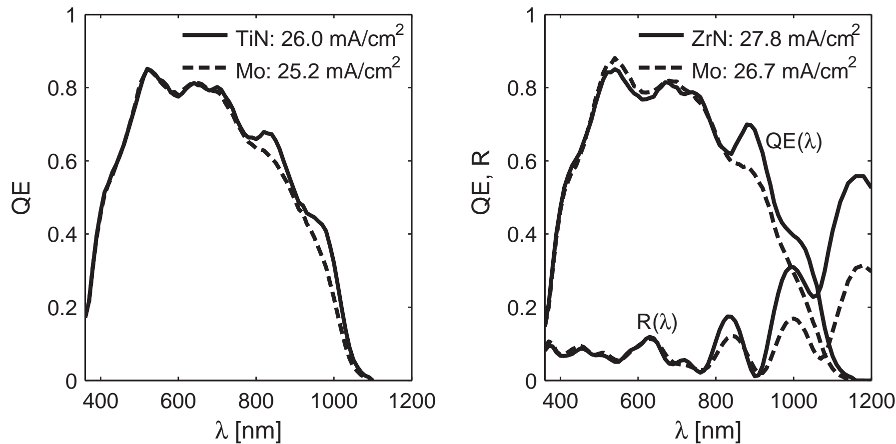

Figure 5.2: Experimentellt bevis för förbättrad kvantverkningsgad (QE) med optiskt förbättrade bakkontakter för tunna (ca 0,5 μm) CIGS-skikt. Effekten märks för längre våglängder λ, där absorptionen i CIGS-skiktet är svagare. Till vänster visas fallet med TiN och till höger med ZrN. Den observerade ökning överensstämmer väl med förutsägelserna från den optiska modellen. Notera för ZrN-provet till höger att solcellens reflektans, $R(\lambda)$, ökar, vilket bekräftar ökad bakkontkatsreflektans R_b för CIGS/ZrN jämfört med CIGS/Mo.

Vad gäller bakkontakten fungerar standardkontakten av Mo *elektriskt* mycket bra, medan den optiska vinst som erhölls med en bakkontakt av ZrN mer än kompenserades av elektriska förluster orsakade av ökad kontaktresistans och ökad rekombination för övergången mellan CIGS och ZrN. Efter att problemets orsak analyserats, kunde det emellertid lösas genom att ett tunt skikt av molybdenselenid, $MoSe_2$, introducerades som ett kontaktskikt mellan ZrN- och CIGS-skikten.

Solcellsmoduler ska tåla att under lång tid utsättas för varierande klimatförhållanden, från mycket kallt till varmt och fuktigt. Det ställer höga krav på de ingående materialens stabilitet, vilket testas genom att utsätta solceller för accelerad klimattestning vid hög temperatur och luftfuktighet. Sammansättningen för CIGS kan varieras, vilket innebär att materialet kan fås med bandgap ända från 1,0 eV för ren $CuInSe_2$ till 1,7 eV för ren $CuGaSe_2$. De solceller som uppvisat högst stabilitet har tillverkats med CIGS med bandgap på 1,1-1,3 eV, det vill säga mellan dessa ändvärden. En förklaringsmodell för denna observation har lagts fram i avhandlingen.

6. Acknowledgements

A large number of people have contributed to make the accomplishment of this thesis possible and the five years spent at the Ångström Laboratory enjoyable. I would like to thank ...

Lars Stolt, my supervisor, for accepting me as a student and for giving me continuous support also on a personal level, for showing confidence in me and for being tolerant with my less good sides.

All current and earlier members of the solar cell group that I have been privileged to work with; a group of people that I find extraordinarily nice – is there a solar biased selection? Special thanks to ...

Olle Lundberg, with whom I have been lucky to share office, and who has learnt me so much about CIGS in particular and about life in general whenever we have spent time together in the lab, at the gym, on the ice, on the dance floor, and in the skiing track – I look forward to join you for Vasaloppet 2006; I promise that I will not be writing on a thesis on the first Sunday of March next year!

Johan Wennerberg, a deeply appreciated friend who helped me into the project leading to Paper VI and Paper VII, and with whom I have shared many formative experiences also outside the Ångström Lab. The same goes for *Jan Sterner*, whom I also thank for inviting me to the project of Paper II.

Sebastian Schleussner for the fruitful co-operation we had during his master thesis on ZrN reflector cells; I am glad to see you back in Uppsala!

Marika Edoff for her attentive leadership of the group the last years.

John Kessler for all inspiring discussions about science and about everything, and for bringing me new perspectives and good old sayings – I know much too well with what that road to hell is paved!

The whole group for the encouragement, time, resources and continuous support that has been offered me these last few weeks of intense writing. In particular the discussions with *Ulf Malm*, and careful manuscript reading and correction by the amazing *Uwe Zimmermann*, Ulf and Sebastian, and the last few days extra support from Lars and Marika, have been valuable.

Jörgen Westlinder for inspiring co-operation in the project of Paper IX and for all the good time spent together outside work. To be continued!

Sören Berg and *Marianne Asplund* for their contribution to the good atmosphere prevailing at the department of Solid State Electronics.

Part of my Ångström heart will always belong to the Solid State Physics department, where I was first accepted as a project worker, and where I have felt welcome since and often found help and support. In particular, I thank *Arne Roos* and *Jacob Jonsson* for sharing their expertise on optical characterization. I also thank ...

Kay Orgassa for valuable discussions about CIGS optics and for good company at conferences, along with another nice colleague of his, *George Hanna*.

Taher Mazloomian at Geotryckeriet for showing flexibility in the printing of this thesis.

Min närmaste familj, mamma och pappa; Susanna, Bertrand, Emil, och Linnea; Petter, Sara, Arvid och Ylva för omtanke och kärlek.

Finally, *all tax payers in Sweden and throughout the European Union* who have financed my salary for the last five years – I sincerely hope that this massive investment in my research education some day will prove to have paid back in one way or another.

References

[1] B. Lomborg, *The Skeptical Environmentalist*, 2001.

[2] C. Murphy and B. Ross-Larson, Eds., *Human Development Report 2004*. UNDP, 2004.

[3] "Intergovernmental panel on climate change." [Online]. Available: http://www.ipcc.ch/

[4] M. A. Green, *Solar Cells. Operating Principles, Technology and System Applications*. Kensington: The University of New South Wales, 1992.

[5] "IEA photovoltaic power systems programme." [Online]. Available: http://www.iea-pvps.org/

[6] U. Rau and H. W. Schock, "Cu(In,Ga)Se_2 solar cells," in *Clean Electricity from Photovoltaics*, ser. Series on Photovoltaic Conversion of Solar Energy, M. D. Archer and R. Hill, Eds. London: Imperial College Press, 2001, vol. 1, pp. 277–345.

[7] W. N. Shafarman and L. Stolt, "Cu(InGa)Se_2 solar cells," in *Handbook of photovoltaic science and engineering*, A. Luque and S. Hegedus, Eds. Chichester: Wiley, 2003.

[8] J. Kessler, M. Bodegård, J. Hedström, and L. Stolt, "Baseline Cu(In,Ga)Se_2 device production: Control and statistical significance," *Solar Energy Materials and Solar Cells*, vol. 67, pp. 67–76, 2001.

[9] O. Lundberg, "Band gap profiling and high speed deposition of Cu(In,Ga)Se_2 for thin film solar cells," PhD Thesis, Uppsala University, 2003. [Online]. Available: http://publications.uu.se/theses/abstract.xsql?dbid=3757

[10] J. Sterner, "ALD buffer layer growth and interface formation on Cu(In,Ga)Se_2 solar cell absorbers," PhD thesis, Uppsala University, 2004. [Online]. Available: http://publications.uu.se/theses/abstract.xsql?dbid=4009

[11] J. Wennerberg, "Design and stability of Cu(In,Ga)Se_2-based solar cell modules," PhD thesis, Uppsala University, 2002. [Online]. Available: http://publications.uu.se/theses/abstract.xsql?dbid=1630

[12] M. Burgelman, P. Nollet, and S. Degrave, "Modelling polycrystalline semiconductor solar cells," *Thin Solid Films*, vol. 361, pp. 527–532, 2000.

[13] S. Degrave, M. Burgelman, and P. Nollet, "Modelling of polycrystalline thin film solar cells: New features in SCAPS version 2.3," in *Proceedings 3rd World Conference on Photovoltaic Energy Conversion*, K. Kurokawa, L. L. Kazmerski, B. McNelis, M. Yamaguchi, C. Wronski, and W. C. Sinke, Eds., vol. A. Osaka, Japan: WCPEC-3 Organizing Committee, 2003, pp. 487–490.

[14] Z. Knittl, *Optics of Thin Films*, ser. Wiley series in pure and applied optics. Prague: John Wiley and Sons, Ltd, 1976.

[15] P. Nostell, A. Roos, and D. Ronnow, "Single-beam integrating sphere spectrophotometer for reflectance and transmittance measurements versus angle of incidence in the solar wavelength range on diffuse and specular samples," *Review of Scientific Instruments*, vol. 70, no. 5, pp. 2481–94, 1999.

[16] A. Djurisic, T. Fritz, and K. Leo, "Determination of optical constants of thin absorbing films from normal incidence reflectance and transmittance measurements," *Optics Communications*, vol. 166, no. 1-6, pp. 35–42, 1999.

[17] A. Djurisic, T. Fritz, K. Leo, and E. Li, "Improved method for determination of optical constants of organic thin films from reflection and transmission measurements," *Applied Optics*, vol. 39, no. 7, pp. 1174–82, 2000.

[18] A. Djurisic, Y. Chan, and E. Li, "Progress in the room-temperature optical functions of semiconductors," *Materials Science & Engineering R: Reports*, vol. R38, no. 6, pp. 237–93, 2002.

[19] D. Lynch and W. Hunter, "Molybdenum (Mo)," in *Handbook of optical constants of solids*, E. D. Palik, Ed. Orlando: Academic Press, 1985, pp. 303–313.

[20] J. Weaver, D. Lynch, and C. Olson, "Optical properties of V, Ta, and Mo from 0.1 to 35 eV," *Physical Review B (Solid State)*, vol. 10, no. 2, pp. 501–16, 1974.

[21] J. Nestell, J.E., R. Christy, M. Cohen, and G. Ruben, "Structure and optical properties of evaporated films of the Cr- and V-group metals," *Journal of Applied Physics*, vol. 51, no. 1, pp. 655–60, 1980.

[22] S. Berg and T. Nyberg, "Fundamental understanding and modeling of reactive sputtering processes," *Thin Solid Films*, vol. 476, no. 2, pp. 215–230, 2005.

[23] S. Schleussner, "Cu(In,Ga)Se_2 thin film solar cells with ZrN as a back contact," Master thesis, Uppsala University/University of Stuttgart, 2003.

[24] M. Veszelei, K. Andersson, C.-G. Ribbing, K. Järrendahl, and H. Arwin, "Optical constants and Drude analysis of sputtered zirconium nitride films," *Applied Optics*, vol. 33, no. 10, pp. 1993–2001, 1994.

[25] C. F. Klingshirn, *Semiconductor Optics*. Berlin: Springer, 1997.

[26] K. Orgassa, "Coherent optical analysis of the ZnO/CdS/Cu(In,Ga)Se_2 thin film solar cell," PhD thesis, Universität Stuttgart, 2004.

[27] M. Alonso, K. Wakita, J. Pascual, M. Garriga, and N. Yamamoto, "Optical functions and electronic structure of $CuInSe_2$, $CuGaSe_2$, $CuInS_2$, and $CuGaS_2$," *Physical Review B (Condensed Matter)*, vol. 63, no. 7, pp. 075 203/1–13, 2001.

[28] M. Alonso, M. Garriga, C. Rincon, E. Hernandez, and M. Leon, "Optical functions of chalcopyrite $CuGa_xIn_{1-x}Se_2$ alloys," *Applied Physics A (Materials Science Processing)*, vol. A74, no. 5, pp. 659–64, 2002.

[29] P. Paulson, R. Birkmire, and W. Shafarman, "Optical characterization of $CuIn_{1-x}Ga_xSe_2$ alloy thin films by spectroscopic ellipsometry," *Journal of Applied Physics*, vol. 94, no. 2, pp. 879–88, 2003.

[30] K. Orgassa, U. Rau, H.-W. Schock, and J. Werner, "Optical constants of $Cu(In,Ga)Se_2$ thin films from normal incidence transmittance and reflectance," in *Proceedings 3rd World Conference on Photovoltaic Energy Conversion*, K. Kurokawa, L. L. Kazmerski, B. McNelis, M. Yamaguchi, C. Wronski, and W. C. Sinke, Eds. Osaka, Japan: WCPEC-3 Organizing Committee, 2003, pp. 2P–A8–04.

[31] A. Forouhi and I. Bloomer, "Optical properties of crystalline semiconductors and dielectrics," *Physical Review B (Condensed Matter)*, vol. 38, no. 3, pp. 1865–74, 1988.

[32] J. Börjesson, "Ellipsometric characterization of the wavelength dependent optical properties of co-evaporated $CuIn_{1-x}Ga_xSe_2$ thin films with varied gallium content x," Master thesis, Linköping University, 2003.

[33] A. Djurisic and E. Li, "Modeling the optical constants of $CuGaSe_2$ and $CuInSe_2$," *Applied Physics A (Materials Science Processing)*, vol. A73, no. 2, pp. 189–92, 2001.

[34] G. Hodes, *Chemical Solution Deposition of Semiconductor Films*, 1st ed. New York: Marcel Dekker, 2003.

[35] C. Yeh, Z. W. Lu, S. Froyen, and A. Zunger, "Zinc-blende—wurtzite polytypism in semiconductors," *Phys. Rev. B*, vol. 46, no. 16-15, p. 10086–10097, 1992.

[36] M. J. Furlong, M. Froment, M. C. Bernard, R. Cortes, A. N. Tiwari, M. Krejci, H. Zogg, and D. Lincot, "Aqueous solution epitaxy of CdS layers on $CuInSe_2$," *Journal of Crystal Growth*, vol. 193, no. 1-2, pp. 114–122, 1998.

[37] A. Kylner and E. Niemi, "Chemical bath deposited CdS films with different impurity concentrations – film characterisation and $Cu(In,Ga)Se_2$ solar cell results," in *Proceedings Fourteenth European Photovoltaic Solar Energy Conference*, H. Ossenbrink, P. Helm, and H. Ehmann, Eds. Felmersham: H.S. Stehphens & Associates, 1997, vol. 2, pp. 1326–9.

[38] S. Ninomiya and S. Adachi, "Optical properties of wurtzite CdS," *Journal of Applied Physics*, vol. 78, no. 2, pp. 1183–1190, 1995.

[39] L. Ward, “Cadmium sulphide (CdS),” in *Handbook of optical constants of solids II*, E. D. Palik, Ed. Orlando: Academic Press, 1991, pp. 579–595.

[40] M. Cardona and G. Harbeke, “Optical properties and band structure of wurtzite-type crystals and rutile,” *Physical Review*, vol. 137, no. 5A, p. 1467, 1965.

[41] T. M. Bienewski and S. J. Czyzek, “Refractive indexes of single hexagonal ZnS and CdS crystals,” *J. Opt. Soc. Am.*, vol. 53, p. 496, 1963.

[42] E. Khawaja and S. Tomlin, “The optical constants of thin evaporated films of cadmium and zinc sulphides,” *Journal of Physics D (Applied Physics)*, vol. 8, no. 5, pp. 581–93, 1975.

[43] E. Palik, “Corrections, additions, and comments,” in *Handbook of optical constants of solids III*, E. D. Palik, Ed. Orlando: Academic Press, 1998, pp. 6–7.

[44] S. Mathew, P. S. Mukerjee, and K. P. Vijayakumar, “Optical and surface properties of spray-pyrolysed CdS thin films,” *Thin Solid Films*, vol. 254, no. 1-2, pp. 278–284, 1995.

[45] B. M. Basol, V. K. Kapur, and A. Halani, “Advances in high efficiency $CuInSe_2$ solar cells prepared by the selenization technique,” in *Conference Record 22nd IEEE Photovoltaic Specialist Conference*. New York: IEEE, 1991, pp. 893–897.

[46] S. Mahanty, D. Basak, F. Rueda, and M. Leon, “Optical properties of chemical bath deposited CdS thin films,” *Journal of Electronic Materials*, vol. 28, no. 5, pp. 559–62, 1999.

[47] D. Brüggeman, “Berechnung verschiedener physikalischer konstanten von heterogenen systemen,” *Annalen der Physik*, vol. 24, p. 636, 1935.

[48] A. Djurisič, Y. Chan, and E. Li, “The optical dielectric function of ZnO,” *Applied Physics A (Materials Science Processing)*, vol. A76, no. 1, pp. 37–43, 2003.

[49] J. Jellison, G.E. and F. Modine, “Parameterization of the optical functions of amorphous materials in the interband region,” *Applied Physics Letters*, vol. 69, no. 3, pp. 371–3, 1996.

[50] G. E. Jellison, Jr., “Data analysis for spectroscopic ellipsometry,” *Thin Solid Films*, vol. 234, no. 1-2, pp. 416–422, 1993.

[51] B. Canava, J. F. Guillemoles, J. Vigneron, D. Lincot, and A. Etcheberry, “Chemical elaboration of well defined $Cu(In,Ga)Se_2$ surfaces after aqueous oxidation etching,” *Journal of Physics and Chemistry of Solids*, vol. 64, no. 9-10, pp. 1791–1796, 2003.

[52] S. Adachi, “Effects of the indirect transitions on optical dispersion relations,” *Physical Review B (Condensed Matter)*, vol. 41, no. 6, pp. 3504–3508, 1990.

[53] T. Asikainen, M. Ritala, and M. Leskelä, “Growth of In_2S_3 thin films by atomic layer epitaxy,” *Applied Surface Science*, vol. 82/83, pp. 122–125, 1994.

[54] S. Spiering, D. Hariskos, M. Powalla, N. Naghavi, and D. Lincot, “Cd-free Cu(In,Ga)Se_2 thin-film solar modules with In_2S_3 buffer layer by alcvd,” *Thin Solid Films*, vol. 431-432, pp. 359–363, 2003.

[55] N. Naghavi, S. Spiering, M. Powalla, B. Cavana, and D. Lincot, “High-efficiency copper indium gallium diselenide (CIGS) solar cells with indium sulfide buffer layers deposited by atomic layer chemical vapor deposition (alcvd),” *Progress in Photovoltaics*, vol. 11, no. 7, pp. 437–443, 2003.

[56] N. Naghavi, R. Henriquez, V. Laptev, and D. Lincot, “Growth studies and characterisation of In_2S_3 thin films deposited by atomic layer deposition (ald),” *Applied Surface Science*, vol. 222, no. 1-4, pp. 65–73, 2004.

[57] I. Lefebvre, M. Lannoo, J. Olivier-Fourcade, and J. C. Jumas, “Tin oxidation number and the electronic structure of SnS-In_2S_3-SnS_2 systems,” *Physical Review B (Condensed Matter)*, vol. 44, no. 3, pp. 1004–1012, 1991.

[58] A. Lavrent’ev, N. Safontseva, V. Dubeiko, B. Gabrel’yan, and I. Nikiforov, “Electronic band structure of In_2S_3 and $CdIn_2S_4$ semiconductor spinels from the data of X-ray spectroscopy and theoretical calculations,” *Fizika Tverdogo Tela*, vol. 42, no. 11, pp. 1992–7, 2000.

[59] M. Womes, J. Jumas, and J. Olivier-Fourcade, “X-ray absorption spectra and conduction band structure of In_2S_3,” *Solid State Communications*, vol. 131, no. 3-4, pp. 257–60, 2004.

[60] S.-i. Katsuki, “The band structure of $CdIn_2S_4$ calculated by the pseudopotential method,” *Journal of the Physical Society of Japan*, vol. 33, no. 6, pp. 1561–1565, 1972.

[61] M. Inoue and M. Okazaki, “Band structure of $CdIn_2S_4$ by Heine-Abarenkov model potential method,” *Journal of the Physical Society of Japan*, vol. 36, no. 3, pp. 780–785, 1974.

[62] H. Nakanishi, “Fundamental absorption edge in $CdIn_2S_4$,” *Jpn. J. Appl. Phys.*, vol. 19, no. 1, pp. 103–108, 1980.

[63] T. Takizawa, H. Ohwada, H. Kobayashi, K. Kanbara, T. Irie, S. Endo, H. Nakanishi, H. Kato, and H. Fukutani, “VUV reflection spectra and fundamental optical constants of $CdIn_2S_4$, $CdInGaS_4$, Cd_3InGaS_6 single crystals,” *Solid State Communications*, vol. 67, no. 7, pp. 739–743, 1988.

[64] W. Rehwald and G. Harbeke, “On the conduction mechanism in single crystal β-indium sulfide In_2S_3,” *Journal of Physics and Chemistry of Solids*, vol. 26, no. 8, pp. 1309–1318, 1965.

[65] K. Kambas, A. Anagnostopoulos, S. Ves, B. Ploss, and J. Spyridelis, “Optical absorption edge investigation of $CdIn_2S_4$ and β -In_2S_3 compounds,” *Physica Status Solidi (B): Basic Research*, vol. 127, no. 1, pp. 201–208, 1985.

[66] R. Becker, T. Zheng, J. Elton, and M. Saeki, "Synthesis and photoelectrochemistry of In_2S_3," *Solar Energy Materials*, vol. 13, no. 2, pp. 97–107, 1986.

[67] R. H. Bube and W. H. McCarroll, "Photoconductivity in indium sulfide powders and crystals," *Journal of Physics and Chemistry of Solids*, vol. 10, no. 4, pp. 333–335, 1959.

[68] S. Gorai, P. Guha, D. Ganguli, and S. Chaudhuri, "Chemical synthesis of β-In_2S_3 powder and its optical characterization," *Materials Chemistry and Physics*, vol. 82, no. 3, pp. 974–979, 2003.

[69] N. Barreau, J. C. Bernede, S. Marsillac, and A. Mokrani, "Study of low temperature elaborated tailored optical band gap β-$In_2S_{3-3x}O_{3x}$ thin films," *Journal of Crystal Growth*, vol. 235, no. 1-4, pp. 439–449, 2002.

[70] N. Barreau, J. Bernede, and S. Marsillac, "Study of the new β-In_2S_3 containing Na thin films. Part II: Optical and electrical characterization of thin films," *Journal of Crystal Growth*, vol. 241, pp. 51–56, 2002.

[71] R. Nomura, K. Konishi, and H. Matsuda, "Single-source organometallic chemical vapour deposition process for sulphide thin films. Introduction of a new organimetallic precursor $Bu^nIn(Spr^i)_2$ and preparation of In_2S_3 thin films," *Thin Solid Films*, vol. 198, no. 1-2, pp. 339–345, 1991.

[72] W.-T. Kim and C.-D. Kim, "Optical energy gaps of β -In_2S_3 thin films grown by spray pyrolysis," *Journal of Applied Physics*, vol. 60, no. 7, pp. 2631–3, 1986.

[73] R. S. Mane and C. D. Lokhande, "Studies on structural, optical and electrical properties of indium sulfide thin films," *Materials Chemistry and Physics*, vol. 78, pp. 15–17, 2002.

[74] C. D. Lokhande, A. Ennaoui, P. S. Patil, M. Giersig, K. Diesner, M. Muller, and H. Tributsch, "Chemical bath deposition of indium sulphide thin films: preparation and chatacterization," *Thin Solid Films*, vol. 340, pp. 18–23, 1999.

[75] E. B. Yousfi, T. Asikainen, V. Pietu, P. Cowache, M. Powalla, and D. Lincot, "Cadmium-free buffer layers deposited by atomic later epitaxy for copper indium diselenide solar cells," *Thin Solid Films*, vol. 361-362, pp. 183–186, 2000.

[76] Y. Yasaki, N. Sonoyama, and T. Sakata, "Semiconductor sensitization of colloidal In_2S_3 on wide gap semiconductors," *Journal of Electroanalytical Chemistry*, vol. 469, no. 2, pp. 116–122, 1999.

[77] M. G. Sandoval-Paz, M. Sotelo-Lerma, J. J. Valenzuela-Jauregui, M. Flores-Acosta, and R. Ramirez-Bon, "Structural and optical studies on thermal-annealed In_2S_3 films prepared by the chemical bath deposition technique," *Thin Solid Films*, vol. 472, no. 1-2, pp. 5–10, 2005.

[78] M. Ylilammi and T. Ranta-aho, "Optical determination of the film thicknesses in multilayer thin film structures," *Thin Solid Films*, vol. 232, no. 1, pp. 56–62, 1993.

[79] E. B. Yousfi, B. Weinberger, F. Donsanti, P. Cowache, and D. Lincot, "Atomic layer deposition of zinc oxide and indium sulfide layers for Cu(In,Ga)Se_2 thin-film solar cells," *Thin Solid Films*, vol. 387, no. 1-2, pp. 29–32, 2001.

[80] C. Guillén, T. Garcia, J. Herrero, M. T. Gutierrez, and F. Briones, "Tailoring growth conditions for modulated flux deposition of In_2S_3 thin films," *Thin Solid Films*, vol. 451-452, pp. 112–115, 2004.

[81] J. Jellison, G.E. and L. Boatner, "Optical functions of uniaxial ZnO determined by generalized ellipsometry," *Physical Review B (Condensed Matter)*, vol. 58, no. 7, pp. 3586–9, 1998.

[82] H. Yoshikawa and S. Adachi, "Optical constants of zno," *Jpn. J. Appl. Phys.*, vol. 36, no. 10, pp. 6237–6243, 1997.

[83] Z.-C. Jin, I. Hamberg, and C. G. Granqvist, "Optical properties of sputter-deposited ZnO:Al thin films," *Journal of Applied Physics*, vol. 64, no. 10, pp. 5117–5131, 1988.

[84] I. Hamberg and C. G. Granqvist, "Evaporated sn-doped in2o3 films: Basic optical properties and applications to energy-efficient windows," *Journal of Applied Physics*, vol. 60, no. 11, pp. R123–R159, 1986.

[85] M. Green, "Lambertian light trapping in textured solar cells and light-emitting diodes: Analytical solutions," *Progress in Photovoltaics: Research and Applications*, vol. 10, no. 4, pp. 235–41, 2002.

[86] E. D. Palik and G. Ghosh, *Electronic Handbook of Optical Constants of Solids*. San Diego: Academic Press, 1999.

[87] Y. Claesson, M. Georgson, A. Roos, and C.-G. Ribbing, "Optical characterisation of titanium-nitride-based solar control coatings," *Solar Energy Materials*, vol. 20, no. 5-6, pp. 455–65, 1990.

[88] K. Orgassa, H. W. Schock, and J. H. Werner, "Alternative back contact materials for thin film Cu(In,Ga)Se_2 solar cells," *Thin Solid Films*, vol. 431-432, pp. 387–391, 2003.

[89] S. J. Fonash, *Solar Cell Device Physics*, ser. Energy Science and Enginennering: Resources, Technology, Management. New York: Academic Press, 1981.

[90] W. Shockley and W. T. Read, "Statistics of the recombinations of holes and electrons," *Physical Review*, vol. 87, no. 5, pp. 835–842, 1952.

[91] R. N. Hall, "Electron-hole recombination in germanium," *Physical Review*, vol. 87, no. 2, p. 387, 1952.

[92] S. B. Zhang, S.-H. Wei, A. Zunger, and H. Katayama-Yoshida, "Defect physics of the $CuInSe_2$ chalcopyrite semiconductor," *Physical Review B (Condensed Matter and Materials Physics)*, vol. 57, no. 16, pp. 9642–9656, 1998.

[93] S.-H. Wei, S. B. Zhang, and A. Zunger, "Effects of Ga addition to $CuInSe_2$ on its electronic, structural, and defect properties," *Applied Physics Letters*, vol. 72, no. 24, pp. 3199–3201, 1998.

[94] ——, "Effects of Na on the electrical and structural properties of $CuInSe_2$," *Journal of Applied Physics*, vol. 85, no. 10, pp. 7214–7218, 1999.

[95] P. Zabierowski, U. Rau, and M. Igalson, "Classification of metastabilities in the electrical characteristics of ZnO/CdS/Cu(In,Ga)Se_2 solar cells," *Thin Solid Films*, vol. 387, no. 1-2, pp. 147–150, 2001.

[96] P. Zabierowski and M. Igalson, "Thermally assisted tunnelling in Cu(In,Ga)Se_2-based photovoltaic devices," *Thin Solid Films*, vol. 361-362, pp. 268–272, 2000.

[97] P. Zabierowski and M. Edoff, "Laplace-DLTS analysis of the minority carrier traps in the Cu(In,Ga)Se_2-based solar cells," *Thin Solid Films*, vol. In Press, Corrected Proof, 2005.

[98] M. Igalson and P. Zabierowski, "Electron traps in Cu(In,Ga)Se_2 absorbers of thin film solar cells studied by junction capacitance techniques," *Opto-Electronics Review*, vol. 11, no. 4, pp. 261–7, 2003.

[99] M. Igalson and M. Edoff, "Compensating donors in Cu(In,Ga)Se_2 absorbers of solar cells," *Thin Solid Films*, vol. In Press, Corrected Proof, 2005.

[100] S. Lany and A. Zunger, "Metal-dimer atomic reconstruction leading to deep donor states of the anion vacancy in II-VI and chalcopyrite semiconductors," *Physical Review Letters*, vol. 93, no. 15, pp. 156 404–4, 2004.

[101] C.-S. Jiang, R. Noufi, J. A. AbuShama, K. Ramanathan, H. R. Moutinho, J. Pankow, and M. M. Al-Jassim, "Local built-in potential on grain boundary of Cu(In,Ga)Se_2 thin films," *Applied Physics Letters*, vol. 84, no. 18, pp. 3477–3479, 2004.

[102] C.-S. Jiang, R. Noufi, K. Ramanathan, J. A. AbuShama, H. R. Moutinho, and M. M. Al-Jassim, "Does the local built-in potential on grain boundaries of Cu(In,Ga)Se_2 thin films benefit photovoltaic performance of the device?" *Applied Physics Letters*, vol. 85, no. 13, pp. 2625–2627, 2004.

[103] N. Ott, G. Hanna, U. Rau, J. Werner, and H. Strunk, "Texture of Cu(In,Ga)Se_2 thin films and nanoscale cathodoluminescence," *Journal of Physics: Condensed Matter*, vol. 16, no. 2, pp. 85–9, 2004.

[104] C. Persson and A. Zunger, "Anomalous grain boundary physics in polycrystalline $CuInSe_2$: The existence of a hole barrier," *Physical Review Letters*, vol. 91, no. 26, pp. 266 401–4, 2003.

[105] K. Taretto, U. Rau, and J. Werner, "Numerical simulation of grain boundary effects in Cu(In,Ga)Se_2 thin-film solar cells," *Thin Solid Films*, vol. In Press, Corrected Proof, 2005.

[106] U. Rau, D. Braunger, R. Herberholz, H. W. Schock, J.-F. Guillemoles, L. Kronik, and D. Cahen, "Oxygenation and air-annealing effects on the electronic properties of Cu(In,Ga)Se_2 films and devices," *Journal of Applied Physics*, vol. 86, no. 1, pp. 497–505, 1999.

[107] U. Rau and H. Schock, "Electronic properties of Cu(In,Ga)Se_2 heterojunction solar cells-recent achievements, current understanding, and future challenges," *Applied Physics A (Materials Science Processing)*, vol. A69, no. 2, pp. 131–47, 1999.

[108] A. L. Fahrenbuch and R. H. Bube, *Fundamentals of solar cells*. New York: Academic Press, 1983.

[109] T. Walter, R. Menner, C. Köble, and H. Schock, in *Proceedings Twelvth European Photovoltaic Solar Energy Conference*, R. Hill, W. Palz, and P. Helm, Eds. Bedford: H.S. Stehphens & Associates, 1994, p. 1755.

[110] U. Rau, "Tunneling-enhanced recombination in Cu(In,Ga)Se_2 heterojunction solar cells," *Applied Physics Letters*, vol. 74, no. 1, pp. 111–13, 1999.

[111] U. Rau, A. Jasenek, H. Schock, F. Engelhardt, and T. Meyer, "Electronic loss mechanisms in chalcopyrite based heterojunction solar cells," *Thin Solid Films*, vol. 361-362, pp. 298–302, 2000.

[112] A.-A. S. Al-Omar and M. Y. Ghannam, "Direct calculation of two-dimensional collection probability in pn junction solar cells, and study of grain-boundary recombination in polycrystalline silicon cells," *Journal of Applied Physics*, vol. 79, no. 4, pp. 2103–2114, 1996.

[113] C. Donolato, "A reciprocity theorem for charge collection," *Applied Physics Letters*, vol. 46, no. 3, pp. 270–272, 1985.

[114] M. Green, "Generalized relationship between dark carrier distribution and photocarrier collection in solar cells," *Journal of Applied Physics*, vol. 81, no. 1, pp. 268–71, 1997.

[115] T. Markvart, "Photogenerated carrier collection in solar cells in terms of dark carrier distribution: Three dimensions," *IEEE Transactions on Electron Devices*, vol. 44, no. 7, pp. 1182–1183, 1997.

[116] U. Rau and R. Brendel, "The detailed balance principle and the reciprocity theorem between photocarrier collection and dark carrier distribution in solar cells," *Journal of Applied Physics*, vol. 84, no. 11, pp. 6412–6418, 1998.

[117] J. Malmström, 2005, un-published.

[118] M. A. Green, "General temperature dependence of solar cell performance and implications for device modelling," *Progress in Photovoltaics: Research and Applications*, vol. 11, no. 5, pp. 333–340, 2003.

[119] W. N. Shafarman, R. Klenk, and B. E. McCandless, “Device and material characterization of Cu(InGa)Se_2 solar cells with increasing band gap,” *Journal of Applied Physics*, vol. 79, no. 9, pp. 7324–7328, 1996.

[120] A. Burgers, J. Eikelboom, A. Schönecker, and W. Sinke, “Improved treatment of the strongly varying slope in fitting solar cell I-V curves,” in *Conference Record 25th IEEE Photovoltaic Specialist Conference*. IEEE, 1996.

[121] U. Malm, “Determination of dominant recombination mechanisms in Cu(In,Ga)Se_2 thin-film solar cells with ALD-ZnO buffer layer,” Master thesis, Uppsala university, 2003.

[122] U. Rau, A. Schmidt, A. Jasenek, G. Hanna, and H. Schock, “Electrical characterization of Cu(In,Ga)Se_2 thin-film solar cells and the role of defects for the device performance,” *Solar Energy Materials and Solar Cells*, vol. 67, no. 1-4, pp. 137–43, 2001.

[123] C. Rincón and J. Gonzáles, “Temperature dependence of the bandgap in $CuInSe_2$,” *Solar Cells*, vol. 16, pp. 357 – 362, 1986.

[124] R. H. Bube, *Photoelectronic Properties of Semiconductors*. Cambridge University Press, 1992.

[125] J. Wennerberg, J. Kessler, M. Bodegård, and L. Stolt, “Damp heat testing of high performance CIGS thin film solar cells,” in *Proceedings 2nd World Conference on Photovoltaic Solar Energy Conversion*, J. Schmid, H. Ossenbrink, P. Helm, H. Ehmann, and E. D. Dunlop, Eds. Ispra: European Commission, 1998, pp. 1161–1164.

[126] Q. Nguyen, K. Orgassa, I. Koetschau, U. Rau, and H. W. Schock, “Influence of heterointerfaces on the performance of Cu(In,Ga)Se_2 solar cells with CdS and In(OH_x,S_y) buffer layers,” *Thin Solid Films*, vol. 431-432, pp. 330–334, 2003.

[127] A. Niemegeers, M. Burgelman, R. Herberholz, U. Rau, D. Hariskos, and H.-W. Schock, “Model for electronic transport in Cu(In,Ga)Se_2 solar cells,” *Progress in Photovoltaics: Research and Applications*, vol. 6, no. 6, pp. 407–421, 1998.

[128] M. Topič, F. Smole, and J. Furlan, “Examination of blocking current-voltage behaviour through defect chalcopyrite layer in ZnO/CdS/Cu(In,Ga)Se_2/Mo solar cell,” *Solar Energy Materials and Solar Cells*, vol. 49, no. 1-4, pp. 311–317, 1997.

[129] M. Igalson, M. Bodegård, and L. Stolt, “Reversible changes of the fill factor in the ZnO/CdS/Cu(In,Ga)Se_2 solar cells,” *Solar Energy Materials and Solar Cells*, vol. 80, no. 2, pp. 195–207, 2003.

[130] M. Morkel, L. Weinhardt, B. Lohmuller, C. Heske, E. Umbach, W. Riedl, S. Zweigart, and F. Karg, “Flat conduction-band alignment at the CdS/$CuInSe_2$ thin-film solar-cell heterojunction,” *Applied Physics Letters*, vol. 79, no. 27, pp. 4482–4484, 2001.

[131] D. W. Niles, M. Al-Jassim, and K. Ramanathan, "Direct observation of Na and O impurities at grain surfaces of $CuInSe_2$ thin films," *Journal of Vacuum Science & Technology A: Vacuum, Surfaces, and Films*, vol. 17, no. 1, pp. 291–296, 1999.

[132] U. Malm, M. Edoff, and L. Stolt, "The stability in damp heat conditions of thin-film CIGS solar cells with different absorber thickness," in *Proceedings Nineteenth European Photovoltaic Solar Energy Conference*, W. Hoffman, J.-L. Bal, H. Ossenbrink, W. Palz, and P. Helm, Eds. Munich: WIP, 2004, vol. II, pp. 1890–1893.

[133] M. Schmidt, D. Braunger, R. Schaffler, H. Schock, and U. Rau, "Influence of damp heat on the electrical properties of $Cu(In,Ga)Se_2$ solar cells," *Thin Solid Films*, vol. 361-362, pp. 283–7, 2000.

[134] C. Deibel, V. Dyakonov, J. Parisi, J. Palm, S. Zweigart, and F. Karg, "Influence of damp heat testing on the electrical characteristics of $Cu(In,Ga)(S,Se)_2$ solar cells," *Thin Solid Films*, vol. 403-404, pp. 325–330, 2002.

[135] M. Igalson, M. Wimbor, and J. Wennerberg, "The change of the electronic properties of CIGS devices induced by the 'damp heat' treatment," *Thin Solid Films*, vol. 403-404, pp. 320–324, 2002.

[136] M. Igalson, M. Bodegård, and L. Stolt, "Recombination centers in the $Cu(In,Ga)Se_2$-based photovoltaic devices," *Journal of Physics and Chemistry of Solids*, vol. 64, no. 9-10, pp. 2041–2045, 2003.

[137] C. Platzer-Bjorkman, J. Lu, J. Kessler, and L. Stolt, "Interface study of $CuInSe_2$/ZnO and $Cu(In,Ga)Se_2$/ZnO devices using ALD ZnO buffer layers," *Thin Solid Films*, vol. 431-432, pp. 321–325, 2003.

[138] G. Hanna, T. Glatzel, S. Sadewasser, N. Ott, H. P. Strunk, U. Rau, and J. H. Werner, "Influence of film texture on the electronic activity of grain boundaries in polycrystalline $Cu(In,Ga)Se_2$ thin films," *Unpublished*.

[139] S. M. Sze, *Physics of semiconductor devices*. New York: John Wiley & Sons, 1981.

[140] E. H. Rhoderick and R. H. Williams, *Metal-Semiconductor Contacts*, 2nd ed., ser. Monographs in Electrical and Electronic Engineering, P. Hammond and R. L. Grimsdale, Eds. Oxford: Oxford University Press, 1988, vol. 19.

[141] A. Klein, T. Löher, C. Pettenkofer, and W. Jaegermann, "Chemical interaction of Na with cleaved (011) surfaces of $CuInSe_2$," *Journal of Applied Physics*, vol. 80, no. 9, pp. 5039–43, 1996.

[142] C. Heske, G. Richter, Z. Chen, R. Fink, E. Umbach, W. Riedl, and F. Karg, "Influence of Na and H_2O on the surface properties of $Cu(In,Ga)Se_2$ thin films," *Journal of Applied Physics*, vol. 82, no. 5, pp. 2411–2420, 1997.

[143] D. Marron, S. Sadewasser, A. Meeder, T. Glatzel, and M. Lux-Steiner, "Electrical activity at grain boundaries of Cu(In,Ga)Se_2 thin films," *Physical Review B (Condensed Matter and Materials Physics)*, vol. 71, no. 3, pp. 33 306–1, 2005.

[144] Y. Gotoh, H. Tsuji, and J. Ishikawa, "Measurement of work function of transition metal nitride and carbide thin films," *Journal of Vacuum Science and Technology B: Microelectronics and Nanometer Structures*, vol. 21, no. 4, pp. 1607–1611, 2003.

[145] T. Wada, N. Kohara, T. Negami, and M. Nishitani, "Chemical and structural characterization of Cu(In,Ga)Se_2/Mo interface in Cu(In,Ga)Se_2 solar cells," *Japanese Journal of Applied Physics, Part 2 (Letters)*, vol. 35, no. 10A, pp. L1253–6, 1996.

[146] S. Nishiwaki, N. Kohara, T. Negami, and T. Wada, "$MoSe_2$ layer formation at Cu(In,Ga)Se_2/Mo interfaces in high efficiency Cu($In_{1-x}Ga_x$)Se_2 solar cells," *Japanese Journal of Applied Physics, Part 2 (Letters)*, vol. 37, no. 1A-B, pp. L71–3, 1998.

[147] N. Kohara, S. Nishiwaki, Y. Hashimoto, T. Negami, and T. Wada, "Electrical properties of the Cu(In,Ga)Se_2/$MoSe_2$/Mo structure," *Solar Energy Materials and Solar Cells*, vol. 67, no. 1-4, pp. 209–15, 2001.

[148] T. Wada, N. Kohara, S. Nishiwaki, and T. Negami, "Characterization of the Cu(In,Ga)Se_2/Mo interface in CIGS solar cells," *Thin Solid Films*, vol. 387, no. 1-2, pp. 118–22, 2001.

[149] R. Wurz, D. Fuertes Marron, A. Meeder, A. Rumberg, S. M. Babu, T. Schedel-Niedrig, U. Bloeck, P. Schubert-Bischoff, and M. C. Lux-Steiner, "Formation of an interfacial $MoSe_2$ layer in CVD grown $CuGaSe_2$ based thin film solar cells," *Thin Solid Films*, vol. 431-432, pp. 398–402, 2003.

[150] A. Mallouky and J. Bernede, "Characterization of $MoSe_2$ thin films," *Thin Solid Films*, vol. 158, no. 2, pp. 285–98, 1988.

[151] P. Rostan, J. Mattheis, G. Bilger, U. Rau, and J. Werner, "Formation of transparent and ohmic ZnO:Al/$MoSe_2$ contacts for bifacial Cu(In,Ga)Se_2 solar cells and tandem structures," *Thin Solid Films*, vol. In Press, 2005.

Acta Universitatis Upsaliensis

Digital Comprehensive Summaries of Uppsala Dissertations from the Faculty of Science and Technology 28

Editor: The Dean of the Faculty of Science and Technology

A doctoral dissertation from the Faculty of Science and Technology, Uppsala University, is usually a summary of a number of papers. A few copies of the complete dissertation are kept at major Swedish research libraries, while the summary alone is distributed internationally through the series Digital Comprehensive Summaries of Uppsala Dissertations from the Faculty of Science and Technology. (Prior to January, 2005, the series was published under the title "Comprehensive Summaries of Uppsala Dissertations from the Faculty of Science and Technology".)

ACTA
UNIVERSITATIS
UPSALIENSIS
UPPSALA
2005

Distribution: publications.uu.se
urn:nbn:se:uu:diva-5721